Dipl.-Ing. Stefanie Fladischer

Application of new EDXS quantification schemes in TEM to organic semiconducting devices

DOCTORAL THESIS

For obtaining the academic degree of

Doktorin der technischen Wissenschaften

Doctoral Programme of Technical Sciences
Technical Physics

Graz University of Technology

Supervisor:

Ao.Univ.-Prof. Dipl.-Ing. Dr.techn. Werner Grogger

Institute for Electron Microscopy and Nanoanalysis

Graz, July 2013

STATUTORY DECLARATION

I declare that I have authored this thesis independently, that I have not used other than the declared sources / resources, and that I have explicitly marked all material which has been quoted either literally or by content from the used sources.

EIDESSTATTLICHE ERKLÄRUNG

Ich erkläre an Eides statt, dass ich die vorliegende Arbeit selbstständig verfasst, andere als die angegebenen Quellen/Hilfsmittel nicht benutzt, und die den benutzten Quellen wörtlich und inhaltlich entnommenen Stellen als solche kenntlich gemacht habe.

Graz, 8. July 2013 ___________________________________

(signature / Unterschrift)

Abstract

In this thesis transmission electron microscopy (TEM) and its analytical methods, in particular energy-dispersive X-ray spectrometry (EDXS), were used to characterize organic semiconducting devices.

In the first part the performance of two TEM-EDXS systems was characterized with regard to detection efficiency, detection sensitivity, energy resolution, stray radiation, geometrical aspects like solid angle and take-off angle as well as absorption effects caused by geometrical conditions. It could be shown that the detection efficiency of the Super-X detector on a Titan^3 is substantially higher than that of the Si(Li) detector on a Tecnai F20, which results in a significantly improved detection sensitivity allowing the detection of trace elements in mush shorter times and with better statistics. In addition, all characteristic X-ray peaks caused by stray radiation were identified for both systems and absorption effects caused by the geometry of the specimen in combination with the design of the Super-X detector were elucidated. The knowledge of the performance of each system is essential to perform reliable EDXS investigations.

In the second part nanoanalytical characterization was performed on organic semiconducting devices, in particular on organic photodiodes (OPDs). As the device performance of OPDs depends on several aspects, such as intrinsic material properties, the topography and roughness of the interfaces as well as the thicknesses of the individual layers, these parameters were elucidated by TEM in combination with scanning electron microscopy (SEM), atomic force microscopy (AFM) and X-ray scattering techniques. The interface roughness progression of consecutive materials was clarified by AFM and X-ray reflectivity measurements exhibiting rough interfaces for the first two crystalline organic materials which are flattened by the amorphous blocking layer of the OPD. The different layers of the OPDs could be identified and distinguished in TEM by the combination of analytical methods as EDXS, electron energy-loss spectrometry (EELS) and energy filtered transmission electron microscopy (EFTEM), and thus their thicknesses could be measured. Furthermore, this work shows that the morphology of organic/metal interfaces strongly depends on process parameters and the involved materials. Material diffusion and the influence of different organic blocking layers introduced into device structures in combination with different deposition techniques of metal electrodes were studied systematically. In the case of crystalline Bphen no Ag diffusion was detected, whereas for amorphous Alq_3 Ag diffusion of varying extent was observed, which depends on both the deposition technique and the deposition rate. Additionally, the dependence on the material and the deposition technique was confirmed by electrical performance measurements of the various OPDs.

In the third part quantitative X-ray analysis was performed using the ζ-factor method. With its ability to intrinsically correct for X-ray absorption, the ζ-factor method significantly improved the quality of the quantification as well as the accuracy of the results in particular regarding the quantification of light elements. The sensitivity factors (ζ-factors) were determined experimentally using a single standard specimen and an estimation of ζ-factors for elements not contained in the standard was performed for both TEM-EDXS systems. These ζ-factors were then used for the quantitative analyses of organic semiconducting materials. The results are in good agreement with the nominal compositions, which is attributed to the absorption correction, and confirm the good performance of the ζ-factor method.

Kurzfassung

In dieser Dissertation wurde die Transmissionselektronenmikroskopie (TEM) und ihre analytischen Methoden im Besonderen die Energie-dispersive Röntgenspektrometrie (EDXS) verwendet, um organische Halbleiterbauelemente zu charakterisieren.

Im ersten Teil wurde die Leistungsfähigkeit zweier TEM-EDXS Systeme in Bezug auf Detektionseffizienz, Detektionssensitivität, Energieauflösung, Streustrahlung, geometrische Aspekte wie Raumwinkel und Abnahmewinkel, sowie Absorptionseffekte aufgrund geometrischer Gegebenheiten bestimmt. Es konnte gezeigt werden, dass die Detektionseffizienz des Super-X Detektors des Titan³ wesentlich höher ist als die des Si(Li) Detektors des Tecnai F20, was zu einer deutlich verbesserten Detektionssensitivität führt, die die Detektion von Spurenelementen in kürzerer Zeit und mit besserer Statistik erlaubt. Des Weiteren wurden für beide Systeme alle charakteristischen Röntgensignale, die durch Streustrahlung verursacht werden, identifiziert und Absorptionseffekte, die aufgrund der Geometrie der Probe in Kombination mit dem Design des Super-X Detektors entstehen, aufgeklärt. Die Kenntnis der Leistungsfähigkeit für jedes System ist erforderlich, um zuverlässige EDXS Untersuchungen durchführen zu können.

Im zweiten Teil wurden nanoanalytische Charakterisierungen an organischen Halbleiterbauelementen, im Speziellen an organischen Photodioden (OPDs), durchgeführt. Da die Leistungsfähigkeit von OPDs von verschiedenen Aspekten, wie Material spezifische Eigenschaften, der Topographie und Rauigkeit der Grenzfläche als auch der Dicke der individuellen Schichten abhängt, wurden diese Parameter mittels TEM in Kombination mit Rasterelektronenmikroskopie (SEM), Atomkraftmikroskopie (AFM) und Röntgenstreuungstechniken aufgeklärt. Der Verlauf der Grenzflächenrauigkeiten der aufeinanderfolgenden Materialien wurde mittels AFM und Röntgenreflektivitätsmessungen aufgezeigt. Die ersten zwei kristallinen organischen Materialien weisen raue Grenzflächen auf, die von der amorphen Blockierungsschicht der OPD geglättet werden. Die unterschiedlichen Schichten der OPDs konnten im TEM anhand der Kombination von analytischen Methoden wie EDXS, Elektronenenergieverlustspektrometrie (EELS) und Energiegefilterte Transmissionselektronenmikroskopie (EFTEM) identifiziert und unterschieden werden, wodurch ihre Dicken gemessen werden konnten. Des Weiteren zeigt diese Arbeit, dass die Morphologie der organischen/metallischen Grenzflächen stark von den Prozessparametern und den involvierten Materialien abhängt. Materialdiffusion und der Einfluss von verschiedenen organischen Blockierungsschichten, die in die Bauelementstruktur eingebracht werden, in Kombination mit verschiedenen Aufbringungsmethoden von Metallelektroden wurden systematisch mittels TEM studiert. Im Fall von kristallinem Bphen wurde keine Ag Diffusion detektiert, wohingegen für amorphes Alq_3 Ag Diffusion von unterschiedlichem Ausmaß abhängig von der Aufbringungsmethode und der Aufbringungsrate beobachtet wurde. Zusätzlich wurde diese Material- und

Aufbringungsmethodenabhängigkeit durch elektrische Leistungsfähigkeitsmessungen bestätigt.

Im dritten Teil wurden quantitative Röntgenanalysen mittels der ζ-Faktor Methode durchgeführt. Mit ihrer intrinsischen Fähigkeit, Röntgenabsorption zu korrigieren, verbesserte die ζ-Faktor Methode wesentlich die Qualität der Quantifizierung und die Genauigkeit der Ergebnisse, im Speziellen der Quantifizierung von leichten Elementen. Die Empfindlichkeitsfaktoren (ζ-Faktoren) wurden experimentell anhand einer Standardprobe bestimmt und die ζ-Faktoren für Elemente, die nicht in der Standardprobe enthalten sind, wurden für beide TEM-EDXS Systeme berechnet. Diese ζ-Faktoren wurden dann für die quantitative Analyse von organischen halbleitenden Materialien verwendet. Die Ergebnisse stimmen mit den nominellen Zusammensetzungen gut überein, was auf die Absorptionskorrektur zurückzuführen ist, und bestätigen die gute Leistungsfähigkeit der ζ-Faktor Methode.

Acknowledgement

Upon completion of my thesis I would like to express my gratitude to a couple of people.

First of all, I would like to thank my supervisor Prof. Werner Grogger for his encouragement and competent support. Additionally, I would like to thank him and Prof. Ferdinand Hofer for the possibility to realize this thesis here at the Institute for Electron Microscopy and Nanoanalysis.

As this thesis was realized within the research project cluster ISOTEC, the collaboration of different scientists was essential for the success of this work. Thus I would like to thank Elke Kraker and Bernd Lamprecht from the Institute for Surface Technologies and Photonics of the Joanneum Research Forschungsgesellschaft for the production of the devices and their electrical characterization. Furthermore, I would like to thank Alfred Neuhold and Prof. Roland Resel from the Institute of Solid State Physics of the Graz University of Technology as well as Ingo Salzmann from the Department of Physics of the Humboldt-Universität zu Berlin for the X-ray measurements.

Concerning the ζ-factor method I wish to thank Prof. Masashi Watanabe from Department of Materials Science & Engineering of the Lehigh University for providing the standard and the software and for helpful support.

A great thank you goes to the institute. I would like to thank Harald Plank for the introduction and support concerning AFM, Stefan Mitsche and Angelika Reichmann for SEM investigation as well as Claudia Mayrhofer, Manuel Paller, Meltem Sezen and Thomas Haber for specimen preparation. Moreover, I would like to thank the whole TEM group for their help in all kinds of questions and challenges. I would especially like to thank those colleagues who sweetened my working days and who became real friends.

Last but not least I would like to thank my family, my “better two-thirds” and my friends for their everlasting support and for making this period of my life a great, unforgettable time.

Contents

1 Introduction 1
2 Energy-dispersive X-ray spectrometry 3
  2.1 X-ray generation 3
  2.2 The energy-dispersive X-ray spectrometer 6
    2.2.1 The semiconductor detector 6
    2.2.2 Si(Li) and SDD detectors 7
    2.2.3 Detection efficiency 8
    2.2.4 Detector artifacts 9
  2.3 Used TEM-EDXS systems 10
    2.3.1 Comparison of detection efficiency 13
    2.3.2 Stray radiation 14
    2.3.3 Orientation of specimen in microscope - Absorption effects 16
  2.4 TEM-EDXS system characterization 18
    2.4.1 Energy resolution 18
    2.4.2 Solid angle 20
    2.4.3 Further parameters 23
  2.5 Detection sensitivity 24
  2.6 Coherent bremsstrahlung 27
3 Organic semiconducting devices 31
  3.1 Organic photodiode 32
  3.2 Preparation of OPDs for TEM investigation 34
    3.2.1 Preparation of OPDs with flexible substrates 34
    3.2.2 Preparation of OPDs with rigid substrates 36
  3.3 Challenges of OPDs concerning TEM investigations 39
    3.3.1 Organic materials 39
    3.3.2 Hydrocarbon contamination 40
    3.3.3 Ag alteration 41
  3.4 Nanoanalytical characterization of OPDs 43

3.4.1 Interface topography, roughness and layer thickness 43
3.4.2 Distinction of organic materials in TEM 48
3.5 Diffusion of Ag into organic semiconducting materials 60
3.5.1 The Ag layer 63
3.5.2 Diffusion of Ag into Alq_3 and Bphen 66
4 Quantitative EDXS analysis 72
4.1 The ζ-factor method 74
4.2 Determination of ζ-factors 79
4.2.1 ζ-factors of the Si(Li) detector 80
4.2.2 ζ-factors of the Super-X detector 83
4.3 Application of ζ-factor method 87
4.3.1 Sapphire 87
4.3.2 Organic semiconducting materials 89
5 Conclusion and Outlook 94
6 Bibliography 97
A. Appendix 103
A.1 Abbreviations 103
A.2 ζ-factors 104

1 Introduction

This thesis was realized within the research project cluster “Integrated Organic Sensor and Optoelectronic Technologies” (ISOTEC) in Work Area 4 called “Nanoanalytical Characterization of Organic Sensor Devices”. The aim of ISOTEC was the fabrication of opto-electronic components for light guiding and light coupling and the development of integrated organic sensors for multi-analyte detection. The focus lay on the realization of an integrated organic optical sensor platform suitable for the parallel detection of multiple parameters such as oxygen, carbon dioxide, pH, temperature and ammonia. This cutting-edge sensor technology approach combined optical sensor layers, realized by optical waveguides, with organic light emitting devices (OLEDs) and organic photodiodes (OPDs) as light source and detection unit respectively. Work Area 4 concentrated on nanoanalytical methods such as transmission electron microscopy (TEM), scanning electron microscopy (SEM), atomic force microscopy (AFM) and X-ray scattering techniques, which were applied for device, process and system characterization regarding morphology, nanostructure and chemical composition.

In this work TEM and its analytical methods in particular energy-dispersive X-ray spectrometry (EDXS) were used to characterize organic semiconducting devices. To perform reliable EDXS investigations it is necessary to know the performance of the TEM-EDXS system. Therefore the following issues need to be considered carefully: Are trace elements of the specimen detectable with the specific TEM-EDXS system? Can two characteristic X-ray lines lying close together be distinguished or do they overlap? Which signals arise due to stray radiation in relation to different TEM-EDXS systems and specimen holders? Do all detected signals originate from the specimen or must they be attributed to stray radiation? Under which angle and in which direction are the characteristic X-rays detected as this issue is important concerning X-ray absorption within the specimen? All these important issues can be elucidated by analyzing different standard specimens, which was done in this work for two TEM-EDXS system, a Tecnai F20 with a Si(Li) detector and a Titan^3 with a Super-X detector. Thus parameters like detection efficiency, detection sensitivity, energy resolution, stray radiation, geometrical aspects like solid angle and take-off angle as well as absorption effects caused by geometrical conditions were determined yielding the performance of both systems and the possibility to perform reliable interpretation and analysis of acquired EDX spectra of unknown specimens.

These two well characterized TEM-EDXS systems were then used to characterize different aspects of ring-shaped OPDs used as detection units in the organic opto-chemical sensor. The integration of the special ring-shaped design of the OPDs was developed in the collaboration of ISOTEC and guarantees that the majority of the fluorescent light is collected. The performance and efficiency of organic electronic devices and especially OPDs depend on several aspects, such as intrinsic material properties, the topography and roughness of the interfaces as well as the thicknesses of the individual layers. Furthermore, material diffusion and the influence of different organic blocking layers introduced into device structures in combination with different deposition techniques of metal electrodes are of particular importance. To elucidate all these parameters influencing the device performance different investigation methods were used such as TEM, SEM, AFM and X-ray scattering techniques. The results of the different investigation methods were compared to each other and together with all collected information a complete picture of the OPD concerning its appearance and device performance could be gained.

For quantitative analysis of light elements in TEM, typically electron energy-loss spectrometry (EELS) is the usual method to choose. It does not suffer from fluorescence yields and gives a much better detection efficiency compared to EDXS. In this work we would like to demonstrate that EDXS can be considered a serious alternative to EELS especially for the quantification of samples consisting of both light and heavy elements. Therefore quantitative analyses of EDX spectra were performed using the ζ-factor method which provides two important advantages in comparison to the Cliff-Lorimer ratio technique: (i) the use of pure-element standard samples, rather than multi-element standards and (ii) a “built-in” X-ray absorption correction with simultaneous mass thickness determination. A condition of the ζ-factor method is the knowledge of the beam current used during the investigation. If the beam current can be measured the ζ-factor method is applicable and benefits from its absorption correction yielding more reliable quantification results in particular regarding the quantification of light elements. A condition for the accuracy of the ζ-method is the correct determination of the sensitivity factors (ζ-factors). In this work the ζ-factors were determined experimentally using a standard specimen comprising five elements. Based on these five values a series of ζ-factors covering a significant fraction of the periodic table can be estimated enabling the quantification of a multitude of elements. In this work the ζ-factor method was applied to EDX spectra of different materials, on the one hand to stable materials like sapphire and on the other hand to sensitive organic materials frequently used in organic semiconducting devices and in particular in the ring-shaped OPDs. The results of the quantitative analyses are in good agreement with the nominal compositions for the different materials comprising either light elements exclusively or in combination with metal atoms. This good agreement is attributed to the absorption correction of the ζ-factor method and confirms the powerful performance of this method for quantitative analytical investigations in TEM.

2 Energy-dispersive X-ray spectrometry

Energy-dispersive X-ray spectrometry (EDXS) in transmission electron microscopy (TEM) developed significantly in recent years concerning both the hardware and the analysis methods. Large area detectors (www.bruker.com and www.oxford-instruments.com) and multiple detector systems (Schlossmacher et al., 2010a, Schlossmacher et al., 2010b) were implemented to the TEM column yielding bigger solid angles and thus significantly improving the detection efficiency. Thus the accuracy of EDXS was raised to a new level.

In the following chapters the fundamental issues concerning EDXS, the X-ray emission process, the X-ray detectors, the TEM-EDXS system and experimental aspects will be discussed in both theory and practice.

2.1 X-ray generation

When the electron beam hits the specimen, one possible interaction is the emission of characteristic X-rays. The basic concept of this interaction in the TEM is described as follows. If an electron of the high energetic electron beam ionizes an atom of the specimen by ejecting an inner shell electron, the ionized atom can return to its ground state by filling the generated hole in the inner shell with an electron from one of the outer shells. According to this energy difference either a characteristic X-ray or an Auger electron is emitted.

The processes of emitting characteristic X-rays and Auger electrons are competing processes. In Figure 2.1 the X-ray and Auger electron yields indicating the probability of emitting X-rays and Auger electrons are depicted as function of the atomic number. The X-ray yield (ω) is a strong function of the atomic number (Z) and increases with increasing Z. One approximate expression for ω is (Wentzel, 1927):

$$\omega = \frac{Z^4}{b + Z^4} \tag{2.1}$$

ω … X-ray yield
Z … atomic number
b … constant ($b \approx 10^6$)

Note that the X-ray yield for light elements is very low and increases with rising atomic number. Thus EDXS analysis of light elements is challenging due to the low X-ray generation rate.

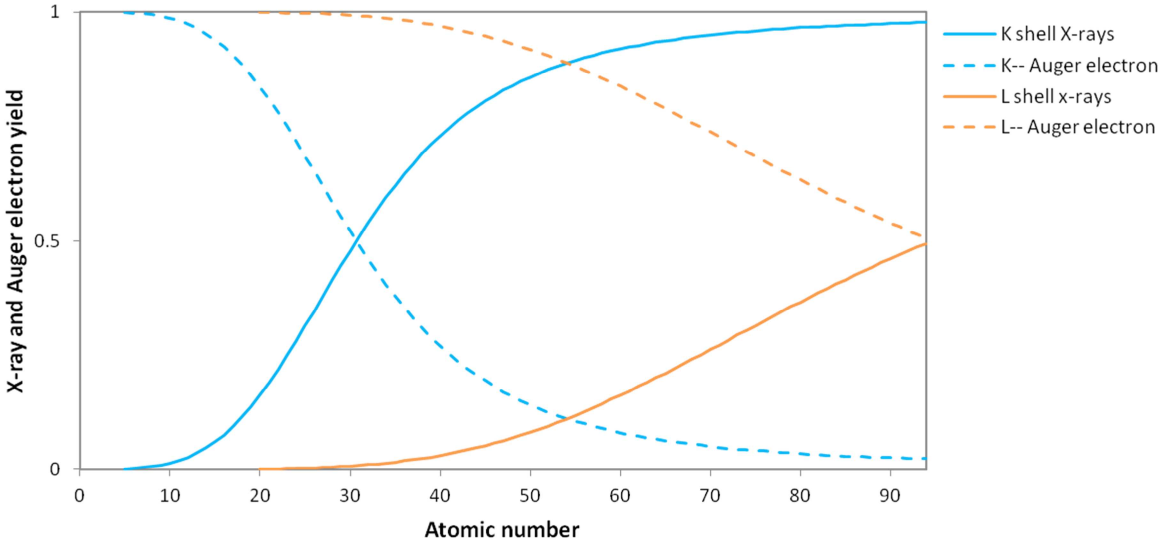

Figure 2.1: X-ray and Auger electron yield as a function of the atomic number. (Values from the Electron Probe Microanalysis Laboratory of the University of California in Berkeley)

According to the selection rules of electron transitions within an atom, X-rays of different energies are emitted. In Figure 2.2 possible electron transitions giving rise to characteristic X-rays are shown. The notation of the X-rays indicates the involved electrons. K, L or M implies that the atom has been ionized by ejecting an electron from the K, L or M shell. The further notation using greek letters (α, β, γ, etc.) and integer numbers describes the involved outer shell, from which the electron fills the hole.

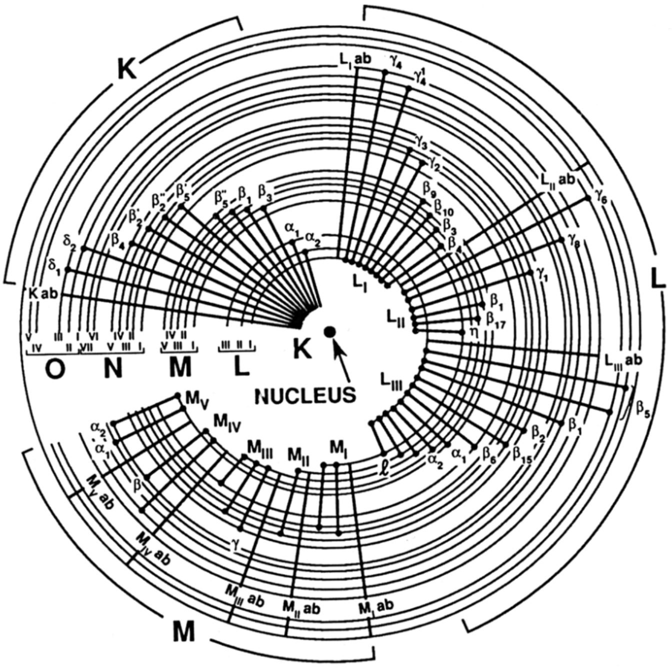

Figure 2.2: The complete range of possible electron transitions that give rise to K, L and M characteristic X-rays. (Williams & Carter, 1996)

The energies of the emitted X-rays are characteristic for the elements. Thus by measuring the characteristic X-ray energies, the corresponding elements can be identified. The energy range of the characteristic X-rays lies between 0.2 and 100 keV. In Figure 2.3 the energies of the characteristic Kα1, Kβ1, Lα1 and Lβ1 X-rays are displayed as a function of the atomic number. For EDXS typically X-ray energies in the range of 0.2 – 40 keV are used due to the detection efficiency of EDXS detectors (see chapter 2.2.3).

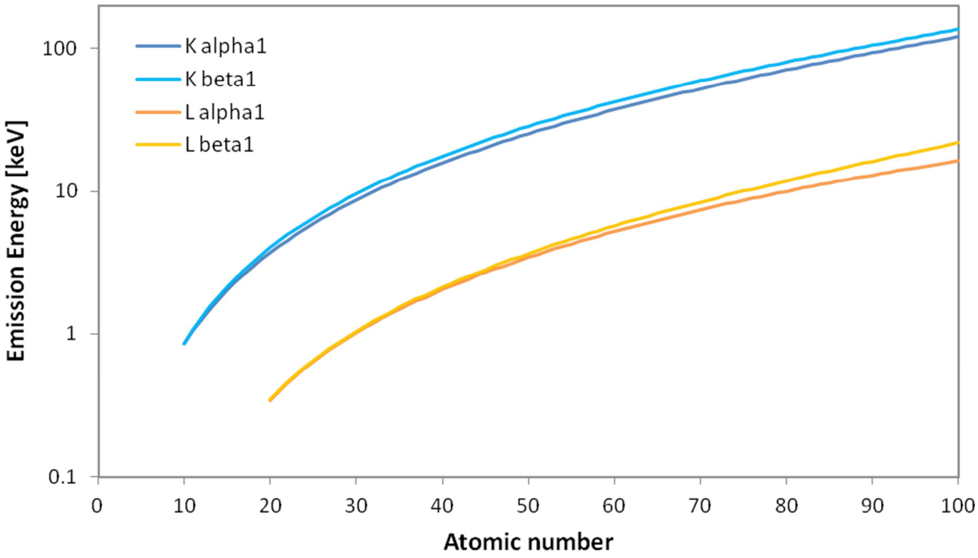

Figure 2.3: Characteristic X-ray energies as a function of the atomic number. (Values from X-ray Transition Energies Database of the National Institute of Standards and Technology (NIST) (Deslattes et al., 2003))

Additionally to characteristic X-rays also bremsstrahlung is generated in TEMs. Bremsstrahlung results from the deceleration of the high energetic beam electrons in the Coulomb field of the atomic nuclei of the specimen. This interaction is detected by EDXS and manifests as a continuous energy spectrum, which is known as background signal of the characteristic X-rays. The bremsstrahlung intensity depends on the atomic number and is a function of the energy (Kramers, 1923):

$$N(E) = \frac{K \cdot Z \cdot (E_0 - E)}{E} \tag{2.2}$$

N(E) … number of bremsstrahlung X-ray quanta
K … Kramers´ constant
Z … atomic number
E … energy of bremsstrahlung X-ray
E_0 … energy of electron

The bremsstrahlung intensity increases with decreasing energy. In EDX spectra the bremsstrahlung drops to zero at very low energies as low energy bremsstrahlung is absorbed in the specimen and the detector. (Williams & Carter, 1996)

2.2 The energy-dispersive X-ray spectrometer

In TEM EDXS is performed by detecting characteristic X-rays and bremsstrahlung using an energy-dispersive X-ray spectrometer. An energy-dispersive X-ray spectrometer consists of three main parts, a semiconductor detector that is interfaced to signal-processing electronics and a computer incorporating the multichannel analyzer (MCA). A schematic diagram of a conventional EDXS detector is depicted in Figure 2.4.

The principal component is a semiconductor detector crystal. An electron trap and a collimator assembly at the entrance of the detector protect the crystal against backscattered electrons and undesired radiation. Depending on the design of the detector either a windowless configuration is chosen or a window is placed in front of the crystal separating the detector vacuum from the TEM column vacuum. When an X-ray hits the semiconductor crystal a charge pulse proportional to the X-ray energy is generated. This pulse is converted to a voltage and preamplified by a field-effect transistor (FET) located behind the crystal. The processing electronics isolates the voltage signal from other pulses, amplifies it further, identifies it as resulting from an X-ray of specific energy and stores the corresponding digitized signal in the proper channel of the MCA. The result is displayed as a histogram of X-ray counts versus energy: an X-ray spectrum.

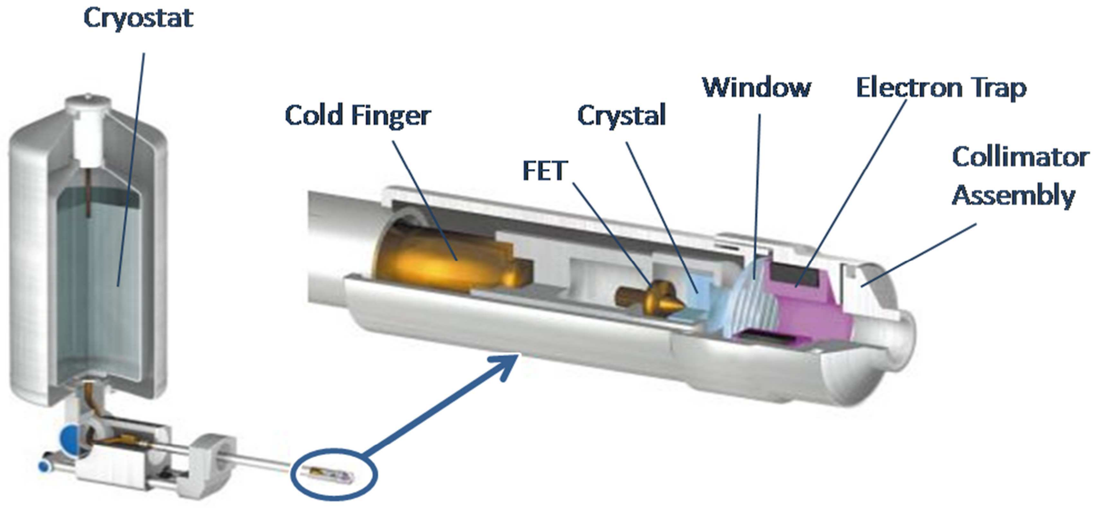

Figure 2.4: Conventional EDXS detector (© Oxford Instruments)

2.2.1 The semiconductor detector

In EDXS different kinds of semiconductor detectors are assembled. Conventional systems use either silicon-lithium Si(Li) or high-purity germanium detectors. In recent years a new technology conquered the market using silicon drift detectors (SDD). The following explanations are made for Si(Li) and SDD detectors as those two types are used in this work.

When X-rays interact with the Si crystal, the predominant method of energy deposition is the transfer of electrons from the valence band to the conduction band, creating electron-hole pairs. Silicon is an indirect semiconductor. The minimum band gap energy is 1.12 eV. To create electron-hole pairs with this minimum energy participating phonons are necessary to provide the required momentum. More likely are direct transitions from the valence to the conduction band. The average energy for the creation of an electron-hole pair with a direct transition is 3.86 eV (Zulliger & Aitken, 1970). Note that characteristic X-rays have energies above 1 keV generating thousands of electron-hole pairs with a single X-ray and that the number of generated electrons/holes is directly proportional to the energy of the X-ray.

2.2.2 Si(Li) and SDD detectors

The Si(Li) detector is a reverse-biased p-i-n diode. In Figure 2.5A a cross section of a Si(Li) detector is shown. In the intrinsic region the electron-hole pairs are generated and thus this region is called the active layer. To compensate for impurities and defects in Si, which would favor recombination of the electron-hole pairs, Li is used filling the recombination sites. Thus the denomination Si(Li) arose. To separate the generated charges Au or Ni contacts are evaporated at the front and the back side of the crystal and a reverse bias of 0.5 – 1 keV is applied (front side: negative, back side: positive). The contact at the front of the crystal is only 2 – 6 nm thick as the X-rays need to traverse it to be detected. As a consequence of the fabrication process a p-type and an n-type layer at the front and the back side of the crystal are created, which are also called dead layers as they don´t contribute to the charge pulse of the incoming X-ray. Si(Li) detectors need to be cooled with liquid N_2 to i) prevent thermally activated electron-hole pairs, giving a noise level that would swamp the characteristic X-ray signal, ii) preserve the intrinsic Li drifted Si region and iii) minimize the noise level in the FET. (Williams & Carter, 1996)

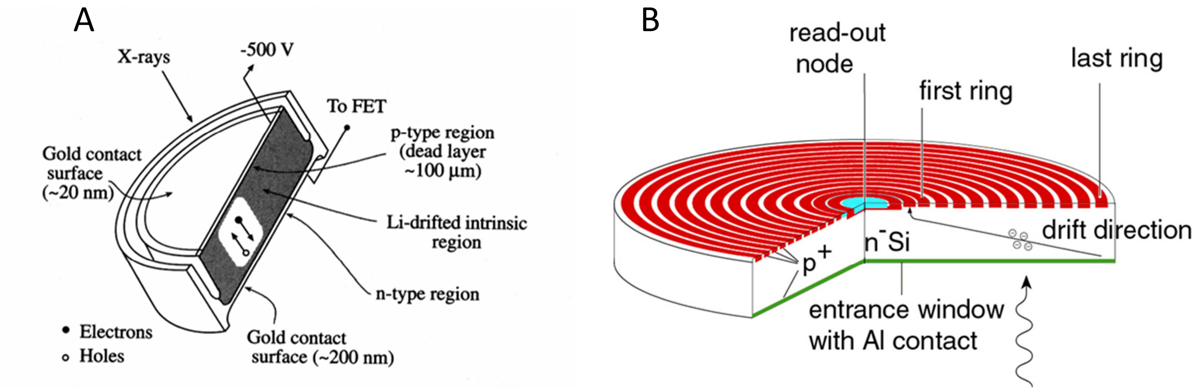

Figure 2.5: Schematic diagrams of A) a Si(Li) detector (Williams & Carter, 1996) and B) an SDD (© PNSensor).

The SDD, as we use it, was presented for the first time in the publication of Lechner et al. (Lechner et al., 1996). A schematic diagram is shown in Figure 2.5B. The major distinguishing feature is a transversal field generated by concentric rings of p-doped Si located at the back side of the single crystal of n-Si. This field together with the field of the Al contact at the front side of the crystal causes the electrons to drift sidewards to the small collection anode in the middle of the drift rings as depicted in Figure 2.5B. As the anode has a much smaller capacitance than the large anode at the back side of a Si(Li) detector, a very high throughput of counts is possible. Another advantage of the SDD is the operating temperature, which is already adjusted by Peltier cooling. This is possible because modern Si-processing technologies reduce thermal-electron generation to extremely low values resulting in very low noise levels even at moderate cooling temperatures. (Williams & Carter, 1996)

2.2.3 Detection efficiency

The detection efficiency is a parameter describing the sensitivity of the EDXS detector to incoming X-rays. It depends on geometrical factors, various detector parameters and the energy of the incoming X-rays. On the one hand low energy X-rays can be absorbed in the different layers that are situated before the active layer, which are i) the window, ii) the contact layer and iii) the dead layer of the crystal. On the other hand high energy X-rays are able to pass through the crystal without being detected. In the latter case the crystal thickness and its mass absorption coefficient are the decisive parameters.

Thus the detection efficiency for an X-ray entering the EDXS detector can be expressed as follows:

$$\varepsilon_A = \exp\left(-\frac{\mu}{\rho}\bigg]_W^A \rho_W t_W\right)\left\{T + (1-T)\exp\left(-\frac{\mu}{\rho}\bigg]_{grid}^A \rho_{grid} t_{grid}\right)\right\}$$

$$\cdot \exp\left(-\frac{\mu}{\rho}\bigg]_{Con}^A \rho_{Con} t_{Con}\right)\exp\left(-\frac{\mu}{\rho}\bigg]_{DL}^A \rho_{DL} t_{DL}\right)\left\{1 - \exp\left(-\frac{\mu}{\rho}\bigg]_{AL}^A \rho_{AL} t_{AL}\right)\right\} \quad (2.3)$$

ε_A … detector efficiency for the energy of the X-rays of element A
$\mu/\rho]^A$ … mass absorption coefficient (MAC) of the X-rays of element A in
    W … window; grid … grid of the window; Con … Contact layer;
    DL … dead layer of the detector; AL … active layer of the detector
ρ … density
t … thickness
T … transmittance of window (typically 77% for ultrathin polymer windows)

The first four terms of equation (2.3) describe the detection efficiency for low energy X-rays expressing the possible absorption by the three above mentioned layers, whereas the last term describes the detection efficiency for high energy X-rays.

To compare the performance of a Si(Li) and an SDD detector their detection efficiencies are displayed in Figure 2.6 as a function of the X-ray energy. The detection efficiency for both EDXS detectors is computed for typical setups. The Si(Li) detector (blue curve) has a crystal thickness of 3 mm and an ultrathin polymer window (AP3.3 window from Moxtek). The SDD (red curve) is a windowless detector with a crystal thickness of 450 µm. In the low energy region the effect of the window is clearly demonstrated. The windowless SDD reaches high detection efficiency already at low energies, whereas the low energy region of the Si(Li) is masked by the absorption of the window. Additionally, the absorption edges for the different elements of the crystal, the contact layer and the elements of the window material are visible. The other big difference between the detectors is the decrease of the detection efficiency at medium energies which results from the crystal thickness. The SDD with a thickness of 450 µm already drops its efficiency at about 10 keV whereas the Si(Li) with a 3 mm thick active layer starts decreasing at about 25 keV. Summing up detectors equipped with windows suffer efficiency losses in the low energy region and depending on the crystal thickness the drop in efficiency starts at different medium energies.

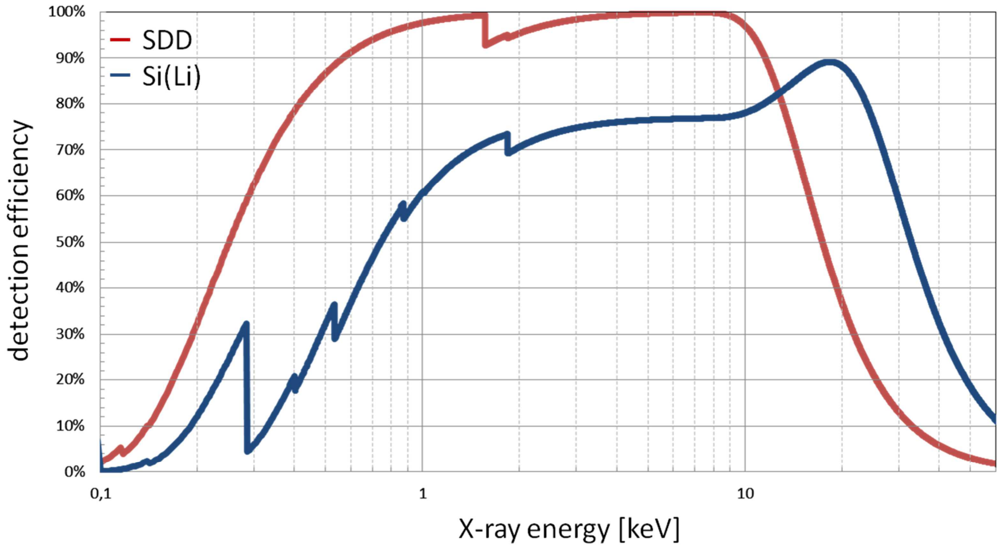

Figure 2.6: Detection efficiency of a Si(Li) and an SDD detector.

2.2.4 Detector artifacts

EDXS detectors produce artifacts deriving from different sources. The main peak may have a tail on its low-energy side due to incomplete charge collection (ICC). The degree to which ICC occurs depends on the quality of the detector crystal. Additional features depending on the photon energy and the count rate are the escape peak, the sum peak and fluorescence peaks caused by the crystal and the contact material. Finally, a shelf caused by hot photoelectrons extends from the main peak down to zero. (Scholze & Procop, 2009)

The manufacturer of our SDD system (Bruker Nano) knows about these artifacts and provides correction files to minimize ICC and shelf. In our case Bruker Nano derived correction files based on several spectra measured on our EDXS system of distinct specimens containing mainly light elements, as low energy X-rays are mainly affected. Thus the following specimens were used Si_3N_4, SiC, BN, MgB_2, $CaMoO_4$, $KAlSi_3O_4$, LaB_6 and Na_3AlF_6 to evaluate the EDXS system and deduce the correction files. In Figure 2.7 the effect of applying correction files can be seen for the example of Al_2O_3; EDX spectra are depicted without correction (blue curve) and applying the correction file (orange curve). The Al K peak only shows minimal alteration whereas the correction of the tailing and a slight energy shift of the O K peak are obvious. Note that the correction of these artifact signals leads to a higher O intensity.

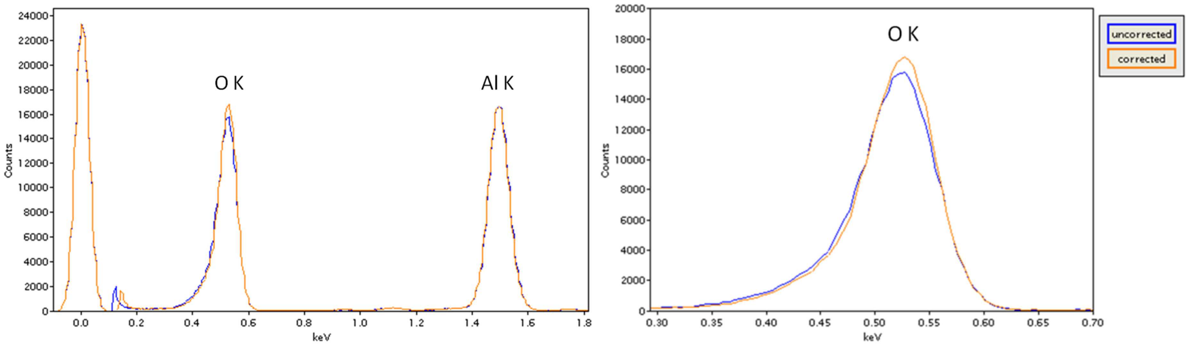

Figure 2.7: Corrected and uncorrected EDX spectra of Al_2O_3 and the O K peak with zoomed energy axis.

2.3 Used TEM-EDXS systems

The basic working principles about TEM, scanning transmission electron microscopy (STEM), energy-loss spectrometry (EELS) or energy filtered transmission electron microscopy (EFTEM) can be found in e.g. books of Williams & Carter and Egerton (Williams & Carter, 1996, Egerton, 1996). The following TEM-EDXS systems were used for this work.

The FEI Tecnai F20 (S)TEM is equipped with a Schottky field-emission gun (FEG) at a high voltage of 200 kV. A schematic diagram and a picture of the instrument are shown in Figure 2.8. It is equipped with a monochromator, a DigiScan II STEM controller, high angle annular dark field (HAADF), annular dark field (ADF) and bright field (BF) detectors and a high resolution Gatan Imaging Filter (GIF) for EELS and EFTEM. The point resolution in TEM mode is 0.24 nm and the HR STEM resolution is 0.2 nm.

Furthermore the Tecnai F20 is equipped with a conventional EDXS detector from EDAX. It consists of a Sapphire Si(Li) detector with an active area of 30 mm², an active layer thickness of 3 mm and an ultrathin polymer window (AP3.3 window from Moxtek).

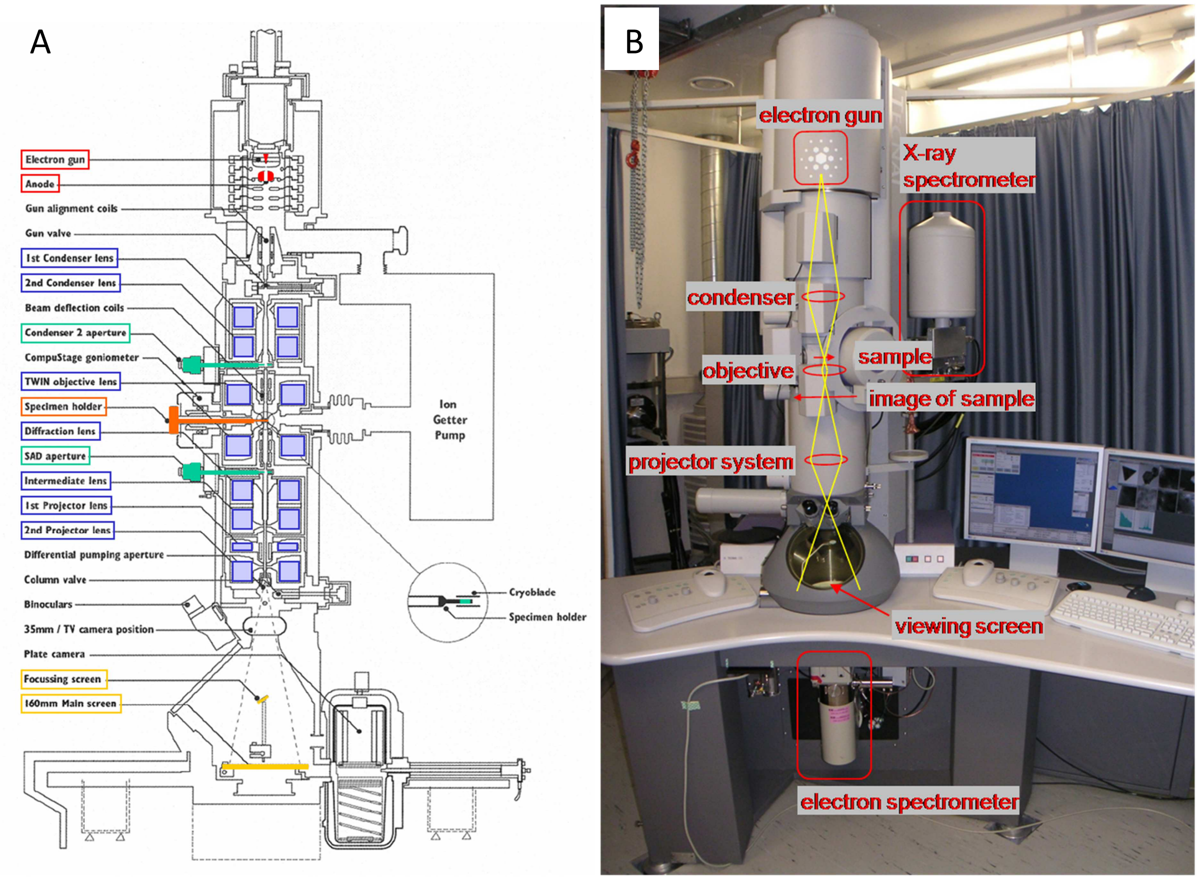

Figure 2.8: A) Schematic diagram of a TEM (© Philips) and B) FEI Tecnai F20

The FEI Titan³ (S)TEM is equipped with an X-FEG high brightness Schottky field emission source and can be operated at high voltages of 80 kV, 200 kV or 300 kV. A schematic diagram and a picture of the Titan³ are shown in Figure 2.9. It is equipped with a monochromator, a Cs-probe corrector for high resolution STEM imaging by correcting spherical aberration, a DigiScan II STEM controller, various HAADF, ADF and BF detectors and a Gatan GIF Quantum energy filter system for high energy-resolution EEL spectroscopy and EFTEM mapping. The TEM point resolution is 0.24 nm and the HR STEM resolution is 0.08 nm due to the Cs-probe correction.

The Titan³ is installed with the ChemiSTEM technology. The ChemiSTEM technology comprises the X-FEG, a special EDXS detector called Super-X detector and fast mapping electronics. The Super-X detector consists of 4 windowless SDD detectors placed symmetrically around the optical axis. In Figure 2.10 schematic diagrams are shown as promoted by FEI (A) and reconstructed together with the Super-X HiVis holder in real dimensions (B). Each quadrant of the Super-X detector has an active area of 30 mm² and a thickness of 450 µm. It is installed at the Titan³ in a windowless design. The ChemiSTEM technology is capable of delivering a 50 – 100 times increase in speed and sensitivity in EDXS mapping applications, thus even allowing for atomically resolved chemical mapping of appropriate specimens.

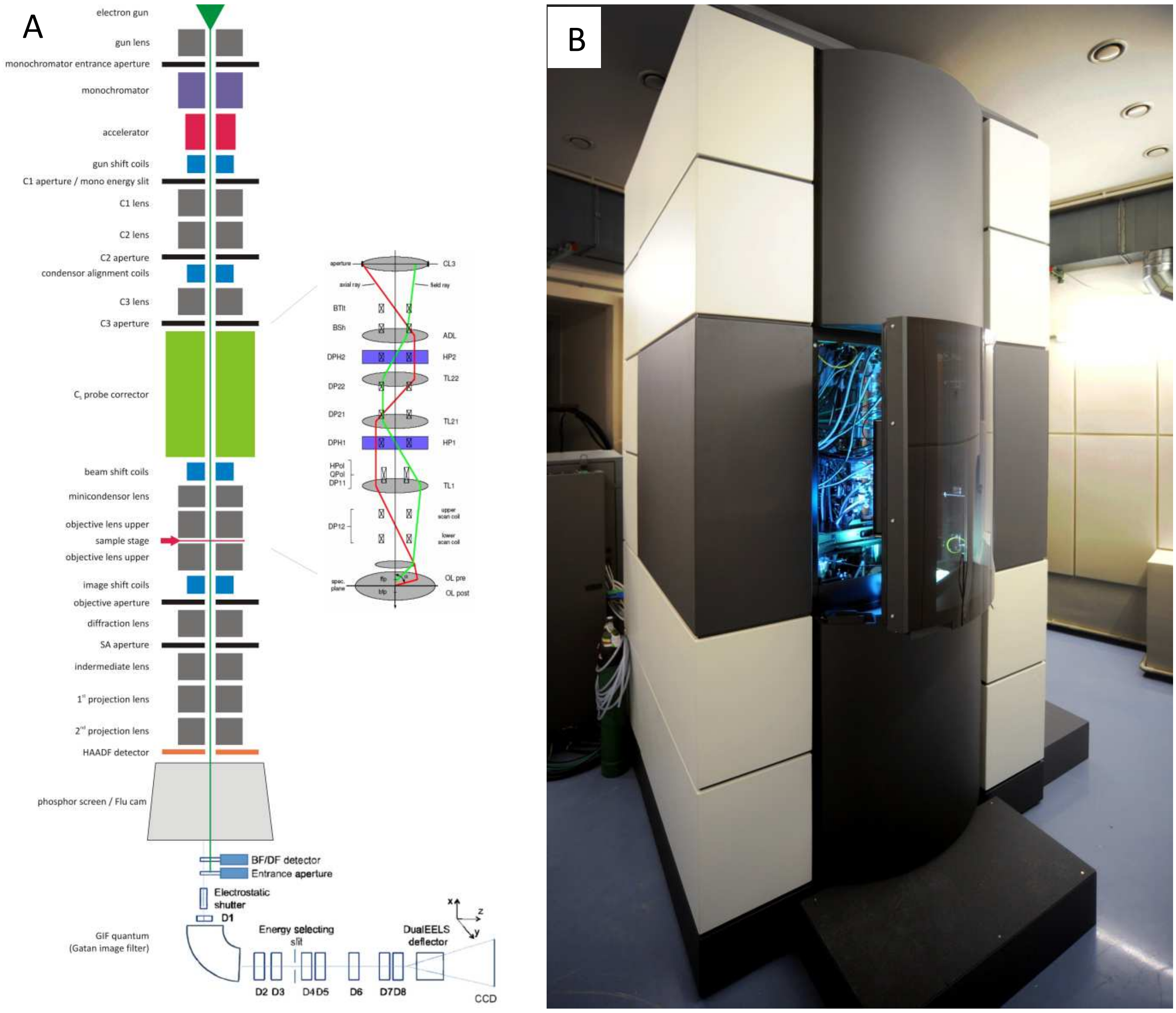

Figure 2.9: A) Schematic diagram of a Cs probe corrected TEM (image by E. Fisslthaler) and B) FEI Titan³

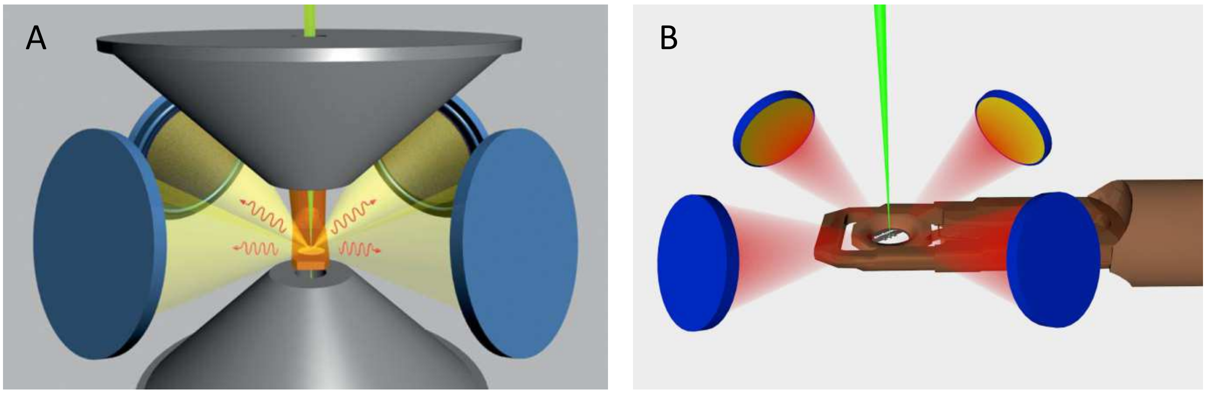

Figure 2.10: Schematic diagram of the Super-X detector A) as promoted by FEI (© FEI) and B) together with the Super-X HiVis holder in real dimensions (image by M. Paller).

To perform reliable EDXS analyses it is important to know the used TEM-EDXS system. Thus our two TEM-EDXS systems were characterized concerning on the one hand detection parameters like detection efficiency, detection sensitivity, stray radiation, energy resolution, etc. and on the other hand geometrical aspects like solid angle, take-off angle as well as absorption effects caused by geometrical conditions. The individual parameters and their characterization are described in both theory and practice in the following chapters. Additionally the results of the characterization of both systems are compared to each other.

2.3.1 Comparison of detection efficiency

The detection efficiency describes the sensitivity of the EDXS detector to incoming X-rays and its theory is explained in chapter 2.2.3. This is one parameter describing the performance of EDXS systems. To compare the performance and the actual detection efficiency of the Si(Li) and the Super-X detector, EDX spectra of a NiOx specimen were acquired using the same acquisition parameters. Therefore a high voltage of 200 kV was chosen for the Titan³ to guarantee the same X-ray generation conditions in both systems. The EDX spectra can be seen in Figure 2.11A with original calibrations and (B) normalized to the Ni Kα peak. These spectra were acquired for an acquisition time of 100 s, a beam current of 0.5 nA was chosen and a specimen area of 0.5 µm² was illuminated.

In Figure 2.11A the huge difference in the detection efficiency of the Si(Li) (red curve) and the Super-X (blue curve) detector is depicted. As the Super-X consists of 4 detectors it possesses a substantially bigger solid angle and a higher detection efficiency in comparison to conventional systems.

Figure 2.11B demonstrates the absorption effect of a window which manifests in the low energy region (Ni L and O K peaks). The Super-X has a higher detection efficiency for medium energies like the Ni Kα peak by a factor of 4.7. For low energies the factor rises to 5.6 for Ni L and even increases to 9.0 for O K. This increase of detection efficiency for low energies is attributed to the windowless design of the Super-X detector. Thus the detection efficiency of a Super-X detector is tremendously increased for the whole energy bandwith detected by EDXS and especially in the low energy region which favors light element detection.

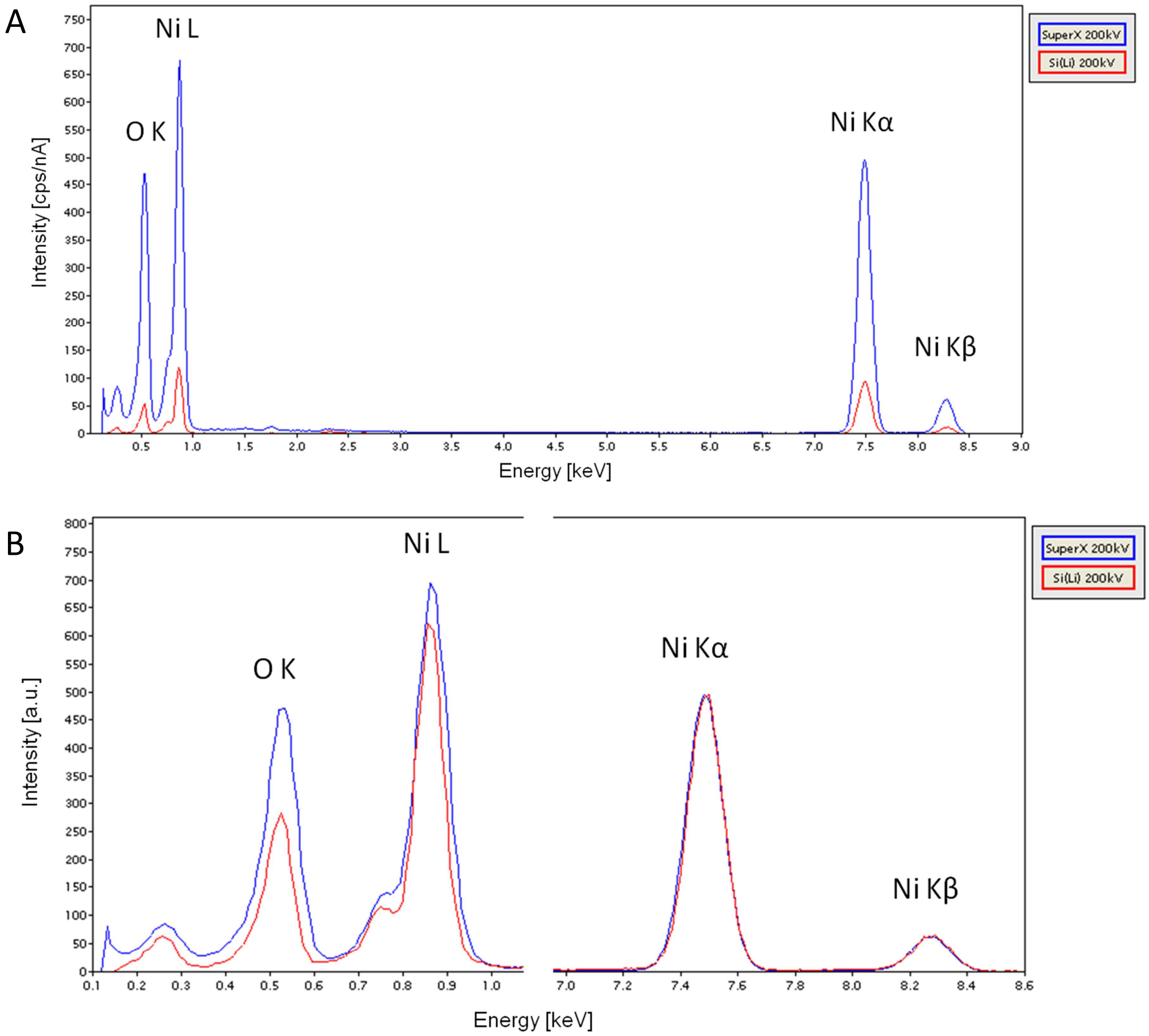

Figure 2.11: EDX spectra of NiOx acquired under same acquisition parameters with the Si(Li) and the Super-X detector A) with original calibrations and B) normalized to the Ni Kα peak.

2.3.2 Stray radiation

An unavoidable artifact in EDXS is stray radiation. It results on the one hand from beam electrons or scattered electrons hitting materials apart from the analysis region of the specimen and consequently generating according characteristic and/or bremsstrahlung X-rays. On the other hand bremsstrahlung X-rays fluoresce characteristic X-rays from any material they stroke. Modern TEMs are designed in such a way that these problems are minimized. Nevertheless, it is important to know about the situation of stray radiation for each TEM-EDXS system, as the detected signals could be interpreted as originating from the specimen. Thus the following paragraphs characterize stray radiation for both TEM-EDXS systems.

When a supporting grid for the specimen is used, characteristic X-rays of the grid material will be detected in the EDX spectra. Typical grid materials are Cu, Mo and Au.

In both TEMs small peaks of Fe and Co appear in the spectra resulting from the interaction of the electrons and the bremsstrahlung X-rays with the objective polepiece.

An analytical double-tilt holder is used for Tecnai F20 consisting of a cup and a clamping ring made of Be to minimize the generation of bremsstrahlung and the detection of stray X-rays, as characteristic X-rays of Be cannot be detected by EDXS.

A Super-X HiVis holder is used for the Titan^3 to insert the specimens. Unfortunately the spacing rings are made of either Cu or Al and the clamps of either Cu or Mo generating detectable stray X-rays.

Figure 2.12 shows an EDX spectrum of Si acquired with the Super-X detector for 15 min. The Fe and Co peak of the objective polepiece and the Cu peaks resulting from the spacing ring and the clamp can be clearly related to their origin. Additionally, small Pb and Zr peaks are visible, but their origin is not clear yet. In this case a quantitative analysis yields following values: c_{Fe} = 0.12 at%, c_{Co} = 0.11 at%, c_{Cu} = 0.43 at% and c_{Zr} = 0.24 at%.

To minimize the effects of stray radiation, the specimen should be kept close to zero tilt. However, in conventional systems tilting the specimen towards the detector is essential to perform reasonable EDXS. The design of the Super-X favors zero tilt analyses being advantageous as stray radiation is minimized.

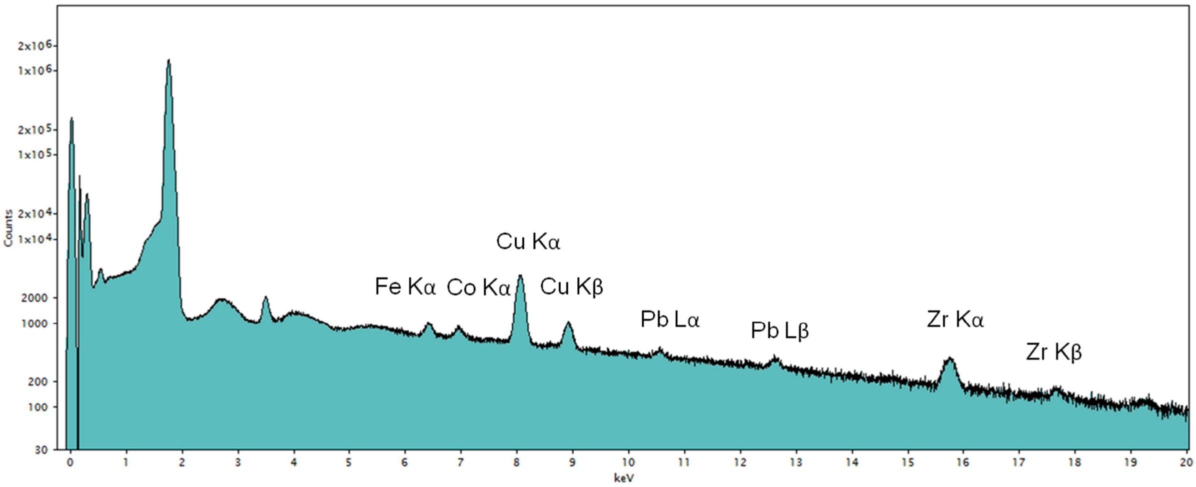

Figure 2.12: EDX spectrum of Si acquired with the Super-X detector and indicated stray radiation.

2.3.3 Orientation of specimen in microscope - Absorption effects

As X-ray absorption effects take place within the specimen and the supporting grids, the orientation of the specimen with respect to the detector has to be chosen thoroughly to acquire EDX spectra representing the specimen with correct peak intensities.

In conventional systems the specimen is fixed in the holder in such a way that the X-rays generated in the specimen are not shadowed by the supporting grid when traveling to the detector. Furthermore when small particles on e.g. a holey carbon film are investigated, one particular edge not being shadowed by the bulk of the particle is chosen for EDXS measurements to prevent X-ray absorption effects within the specimen.

The Super-X detector has the advantage that due to its geometry there is no need of tilting the specimen. But the fact that the quadrants are placed symmetrically around the specimen has to be considered concerning absorption effects.

Figure 2.13A shows a TEM bright-field (BF) image of a $CaMoO_4$ particle, the analyzed region (white circle) and the indicated positions of the quadrants of the Super-X detector. The relative thickness map of the particle indicating the thick bulk of the particle is shown in Figure 2.13B. As the particle was situated in the middle of a mesh the absorption conditions concerning the grid are equal for all quadrants. Figure 2.13C displays EDX spectra of the 4 quadrants. Quadrant 4 acquired the spectrum without additional absorption caused by the bulk of the particle. Thus this spectrum comprises the highest intensities compared to the other quadrants, which received signals with varying degree of absorption due to the bulk of the particle. While quadrants 1 and 3 still got good counting statistics, the majority of the signal traveling in the direction of quadrant 2 was absorbed. Nevertheless the signal detected by quadrant 1 and 3 suffered significant absorption especially in the low energy region. This can be seen clearly when comparing on the one hand the ratios between the Mo L and Ca K with the O K intensity in the spectra and on the other hand the quantitative results of these four EDX spectra with the nominal composition, which are listed in Table 2.1. The quantitative results were obtained by performing the Cliff-Lorimer ratio technique (Cliff & Lorimer, 1975) implemented in the Esprit software of Bruker. This routine does not perform any absorption correction which is the reason for the deviating result of quadrant 4 to the nominal composition. The quantitative results of the EDX spectra acquired with quadrants 1, 2 and 3 are wrong due to absorption effects within the bulk of the specimen taking place to various extents. These spectra can only be used for qualitative identification of the elements in the specimen. Any quantitative analysis of these spectra results in a completely wrong composition. Thus the geometry of the Super-X detector has to be considered carefully and the appropriate quadrants have to be chosen for reliable EDXS analysis.

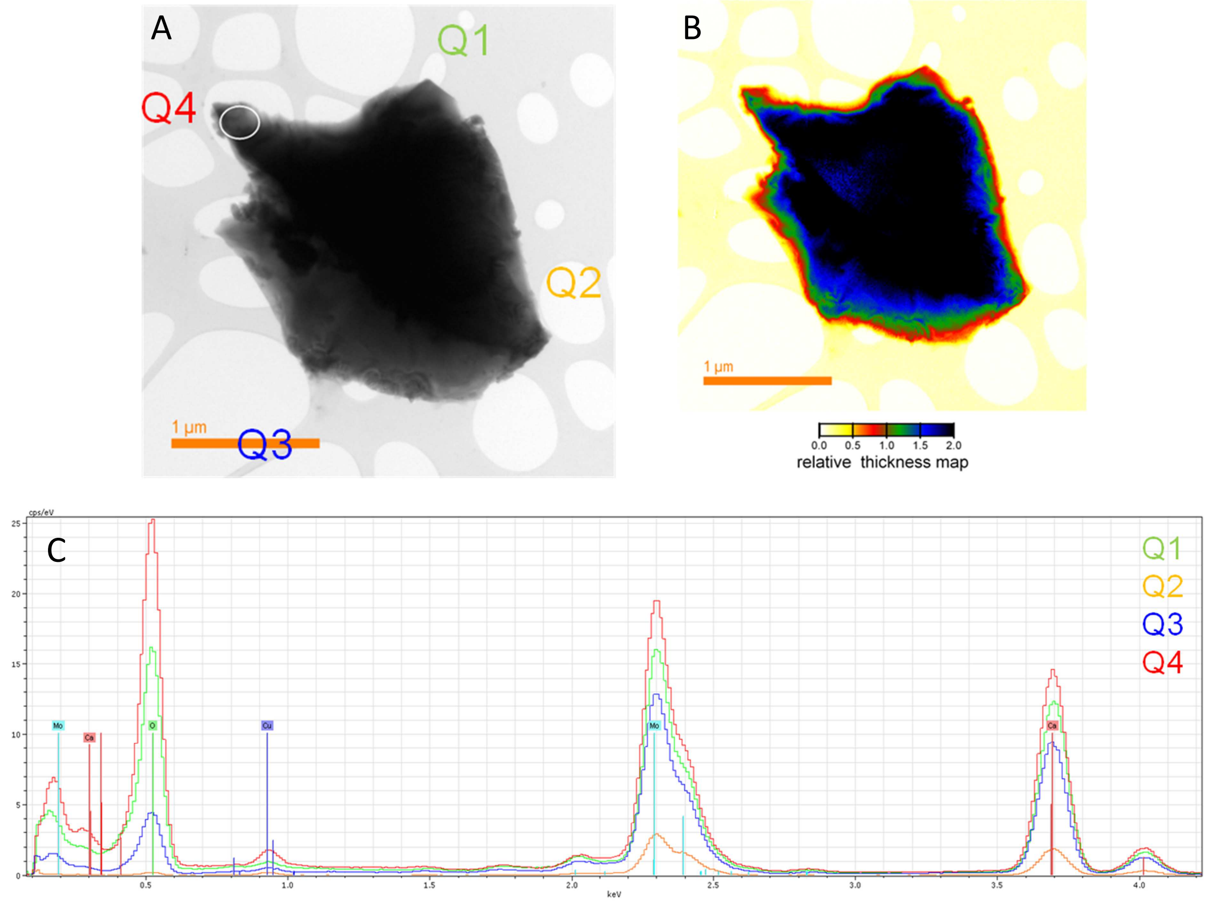

Figure 2.13: A) TEM BF image of a $CaMoO_4$ particle with indicated positions of the quadrants of the Super-X detector and B) relative thickness map of $CaMoO_4$ particle. C) EDX spectra of $CaMoO_4$ acquired with the individual quadrants of the Super-X detector.

Table 2.1: Results of the quantitative analyses (at%) of the EDX spectra of $CaMoO_4$ acquired with the individual quadrants of the Super-X detector together with the nominal composition of $CaMoO_4$.

Quadrant	O	Ca	Mo
Q1	49	25	26
Q2	2	14	84
Q3	23	33	44
Q4	57	22	21
Nominal	66	17	17

As the orientation of the specimen in the Titan^3 relative to the Super-X detector and resulting absorption effects are important for EDXS, right now a diploma thesis is carried out by Margit Schäfer at the Institute of Geometry of the Graz University of Technology to evaluate systematically the geometric situation.

2.4 TEM-EDXS system characterization

For further characterization of the different TEM-EDXS systems a NiOx specimen on a Mo grid (Ted Pella, 2011) was analyzed as described in (Egerton & Cheng, 1994) using a Gatan DigitalMicrograph plug-in (Watanabe, 2009). The analysis of a NiOx spectrum gives information about energy resolution, solid angle, detection efficiency, peak-to-background ratio and stray radiation.

EDX spectra were acquired for both systems for α and β tilt angle series, for different beam currents, specimen positions, high voltages, single quadrants and the entire Super-X detector. Figure 2.14 displays EDX spectra of NiOx acquired with the Si(Li) at 200 kV (green curve) and the Super-X detector at 80 kV, 200 kV and 300 kV (blue, orange and red curve). A beam current of 0.5 nA was used, a specimen area of 0.5 µm² was illuminated and an acquisition time of 100 s was chosen in all four cases.

The above mentioned parameters resulting from the analysis of these NiOx spectra are explained together with theoretical comments in the following chapters.

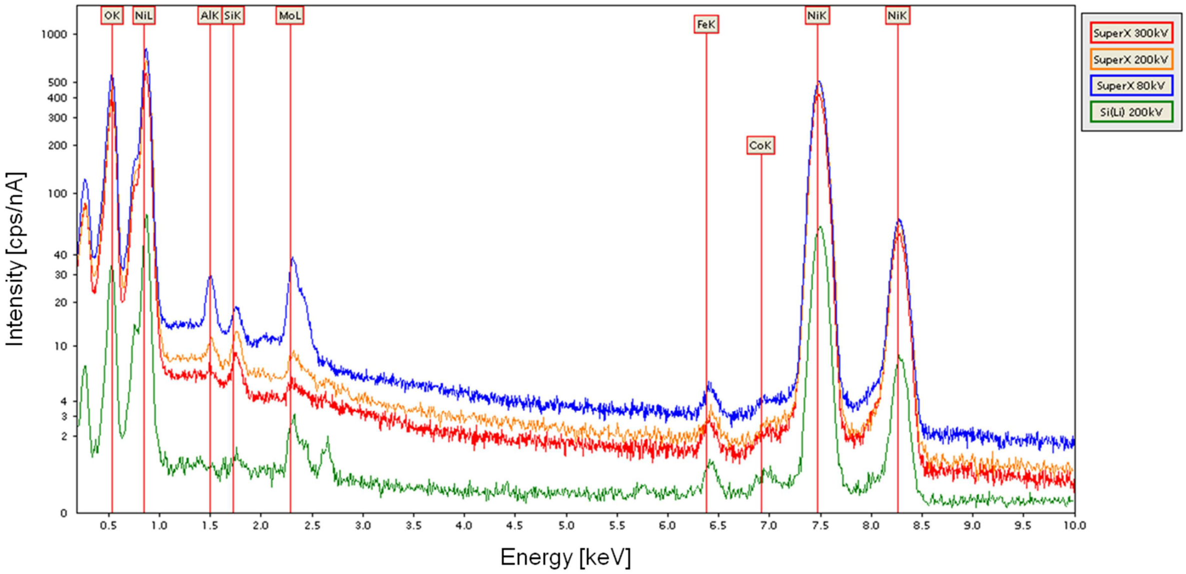

Figure 2.14: EDX spectra of a NiOx specimen acquired with the Si(Li) detector (green), the Super-X detector at 80 kV (blue), 200 kV (orange) and 300 kV (red) in logarithmic scale.

2.4.1 Energy resolution

EDXS detectors cannot measure the energy of a characteristic X-ray with an accuracy corresponding to the natural line width. The measured widths of characteristic X-ray peaks are > 120 eV whereas their natural line widths are only a few eV. The parameter describing this width is the energy resolution which indicates if peaks that are lying close together overlap or can be separated in EDXS. The energy resolution is defined as follows (Lifshin et al., 1975):

$$R^2 = P^2 + 2.35^2(F\varepsilon E) + X^2 \tag{2.4}$$

P … contribution of randomized electronic pulse generation
F … Fano factor (F = 0.1 for Si)
ε … energy for creation of an electron-hole pair in the detector
  (ε = 3.86 eV at 300 K for Si)
E … energy of X-ray line
X … contribution of detector leakage current and incomplete charge collection

Term P is a measure of the quality of the processing electronics, defined as the full width at half maximum (FWHM) of a randomized electronic pulse generator. Term X is the FWHM of detector leakage current and ICC. The middle term describes the intrinsic line width of the detector which is controlled by fluctuations in the numbers of electron-hole pairs that are created by a given X-ray. As the energy resolution depends on the energy of the X-ray line, EDX spectra exhibit different energy resolutions according to the energy of the X-ray peak. Energy resolutions of different EDXS systems are generally compared by measuring the FWHM of the Mn Kα peak at 5.89 keV. (Williams & Carter, 1996)

In our case the energy resolution was determined by analyzing the NiOx spectra for both TEM-EDXS systems. The energy resolution of Mn Kα can be derived from the FWHMs of Ni Kα and O K as described in the publication of Bennett (Bennett & Egerton, 1995). The FWHM values were determined by the DigitalMicrograph plug-in (Watanabe, 2009) by fitting a Gaussian to the peak.

Figure 2.15A displays the energy resolution of the Si(Li) and the Super-X detector as a function of the time constant. The time constant determines the time period that is available for the pulse processor to process the incoming pulse. Short time constants allow to process higher count rates but the energy resolution is degraded as a greater error is done in the assignment of a specific energy to the pulse. Longer time constants give better energy resolution at the expense of a lower count rate. This behavior is clearly depicted for the Si(Li) detector (green triangles) in Figure 2.15A. The shorter the time constant the worse the energy resolution is. The Super-X with its improved electronics and detector design (see chapter 2.2.2) shows a significantly better energy resolution when comparing short time constants.

The energy resolution of the Si(Li) is 134.9 eV for a time constant of 100 µs at 200 kV. The energy resolution of the Super-X detector for a time constant of 1 µs is 139.4 eV at 300 kV, 138.7 at 200 kV and 138.4 at 80 kV. The stated values are mean values of several measurements. Figure 2.15B depicts the energy resolution of the individual quadrants and the entire Super-X detector. It can be seen that quadrants 3 and 4 exhibit better energy resolutions than quadrants 2 and 1, each quadrant reveals a slightly different quality.

Furthermore the energy resolution of the entire detector is the average of the individual quadrants.

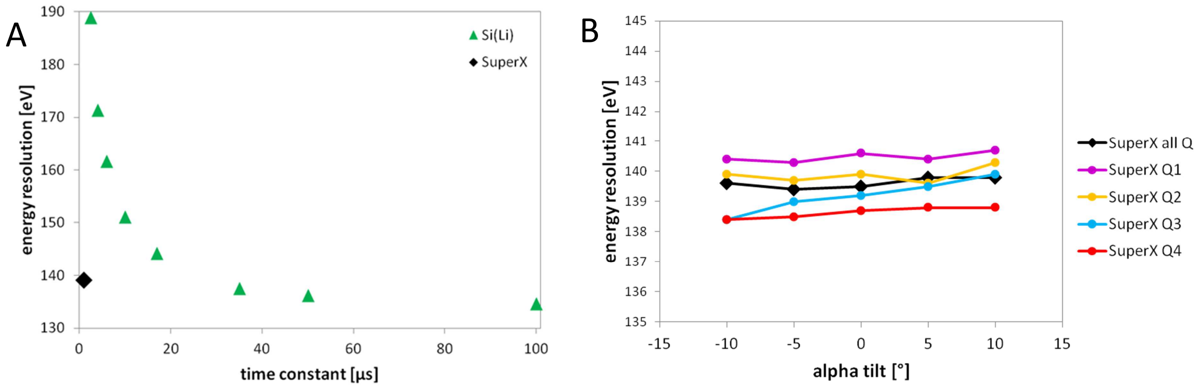

Figure 2.15: A) Energy resolution as a function of the time constant for the Si(Li) and the Super-X detector and B) energy resolution for the individual quadrants and the entire Super-X detector.

2.4.2 Solid angle

The characteristic X-rays of the specimen are emitted in all directions (4π sr), but only a small fraction is detected by the detector. This circumstance is described by the detector collection or solid angle (Ω) and can be seen in Figure 2.16, which displays the interface between the EDXS detector and the TEM stage. The solid angle is determined by geometrical factors and can be analyzed by measured EDXS data.

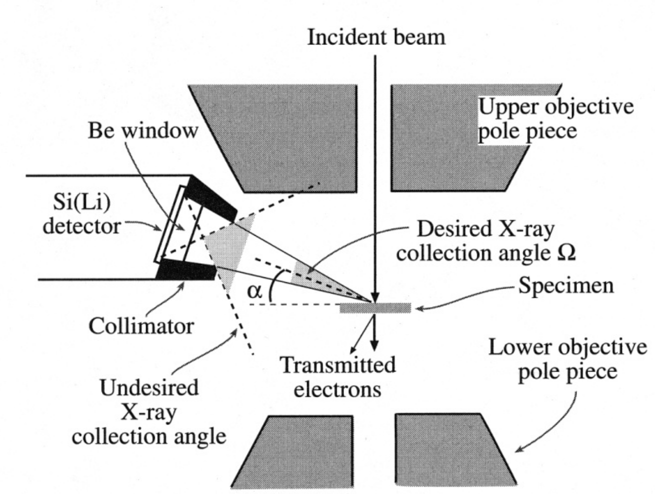

Figure 2.16: The interface between the EDXS detector and the TEM stage and indicated solid angle. (Williams & Carter, 1996)

The geometrical calculation is based on following equation:

$$\Omega = \frac{A \cdot \cos \delta}{S^2} \tag{2.5}$$

A … active area of the detector

S … distance between the detector and the specimen

δ … angle between the normal to the detector face and a line from the detector to the specimen

If a window is placed in front of the detector usually the area of the grid on which the window is mounted is subtracted for the calculation of the solid angle of the TEM-EDXS system. Such calculations imply only geometrical circumstances and do not take into account the real interface of the TEM-EDXS system, e.g. shadowing of the holder.

The actual situation for X-rays concerning the solid angle can be determined by analyzing measured EDX spectra of a NiOx specimen using following equation, which is derived from equation (4.6):

$$\Omega = \frac{C \cdot I\,[Ni\,K\alpha]}{t \cdot \tau \cdot I_b} \tag{2.6}$$

C … constant depending on incident beam energy
I [Ni Kα] … Intensity of the Ni Kα peak above background
t … film thickness
τ … acquisition time
I_b … beam current

When comparing this equation with equation (4.6) it can be seen that the constant C depends amongst other parameters on the ionization cross-section, whose value is an uncertain parameter at high tensions used in TEM, which is explained in detail in chapter 4.1. This consecutive uncertainty of the exact value of the constant C affects the absolute value of the solid angle as well. Nevertheless the experimental determination of the solid angle is an important indication of the real circumstances of the TEM-EDXS interface.

Thus EDX spectra of α and β tilt angle series of a NiOx specimen were analyzed for the determination of the solid angle for the Si(Li) and the Super-X detector using the DigitalMicrograph plug-in (Watanabe, 2009). Figure 2.17A shows the solid angle as a function of the α tilt for the Si(Li) detector, the single quadrants and the entire Super-X detector.

The Si(Li) detector shows the typical solid angle characteristics of a conventional EDXS system. At zero tilt the solid angle is at 50% of its maximum value as half of the detector cannot be illuminated by X-rays originating from the specimen as the specimen holder causes shadowing effects by absorbing the X-rays. The specimen needs to be tilted towards the detector to gain bigger solid angles. In the case of the Si(Li) the maximum solid angle is in the range of 0.1 sr (0.8 % of all emitted X-rays), which is reached with an α tilt angle of at least 15° (β = 0°).

The Super-X detector possesses a solid angle in the range of 0.4 sr (3.2 % of all emitted X-rays), which is significantly bigger than the solid angle of the Si(Li) detector. For the Super-X detector the holder position of the highest solid angle is at zero tilt. Getting the biggest solid angle at zero tilt is an advantage as stray radiation is minimized (see chapter 2.3.2). Figure 2.17A displays the characteristics of the solid angle and the decrease with increasing α tilt in both directions (+α and -α). The solid angle of the entire Super-X detector is the sum of solid angles of the single quadrants. Tilting the holder to one side increases the illumination of 2 quadrants while the 2 opposite quadrants are shadowed and the sum of solid angles is in total smaller than for zero tilt.

Detailed diagrams for the quadrants are displayed in Figure 2.17B and C for tilt angle series of α and β respectively. Note, that tilting α tilts the whole holder whereas tilting β moves only the ring and the holder structure is fixed in its position. The Super-X HiVis holder is displayed in Figure 2.18 with the indicated positions of the quadrants when inserted. The α as well as the β tilt angle series reveal that quadrants 1 and 4 exhibit bigger solid angles than quadrants 2 and 3. Additionally, it can be seen that the solid angle for these two quadrants is at its maximum if the holder is tilted at least 5° to 10°. The maximum solid angle is 0.116 sr for quadrant 1, 0.101 sr for quadrant 2, 0.097 sr for quadrant 3 and 0.111 sr for quadrant 4 when tilting α. For β tilting the maximum solid angles are similar for quadrants 1 and 4 whereas the maximum solid angles for quadrants 2 and 3 are decreased by at most 0.017 sr.

The difference in solid angles between quadrants 1 and 4 and quadrants 2 and 3 is attributed to the design of the Super-X HiVis holder. The Super-X HiVis holder is depicted in Figure 2.18 in top and side view. At the end of the holder the structure holding the ring is lower as the ring, whereas in the direction to the bar, the thickness of the structure increases stepwise and already at the position of the ring, the structure is above the ring and as a consequence shadows quadrants 2 and 3. FEI is working on improvements.

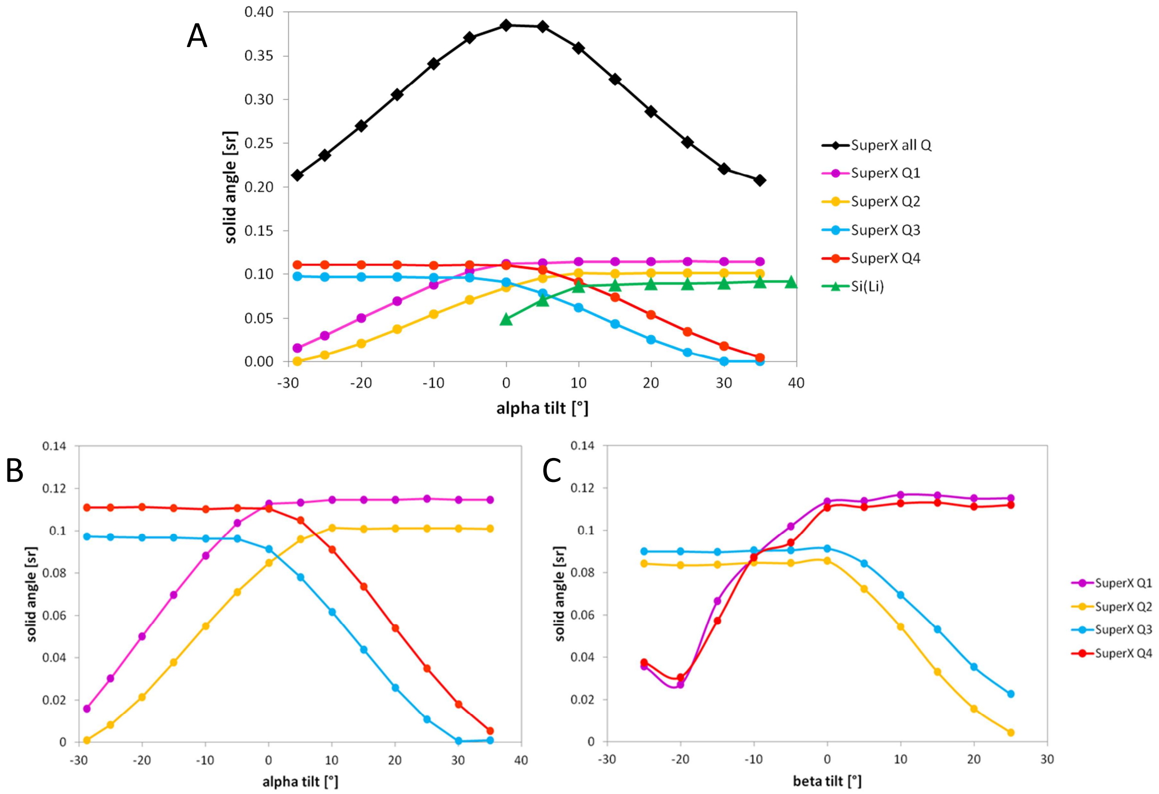

Figure 2.17: A) Solid angle as a function of the tilt angle α for the Si(Li) and the Super-X detector and its quadrants. Solid angle of the quadrants of the Super-X detector as a function of the tilt angle B) α (β = 0°) and C) β (α = 0°).

In Figure 2.17C an increase in solid angle can be seen for quadrants 1 and 4 again at β tilt angles of -25°. This increase can be deduced from detected X-rays from below the holder and because the ring is tilted enough, these X-rays from below the holder can be detected by quadrants 1 and 4.

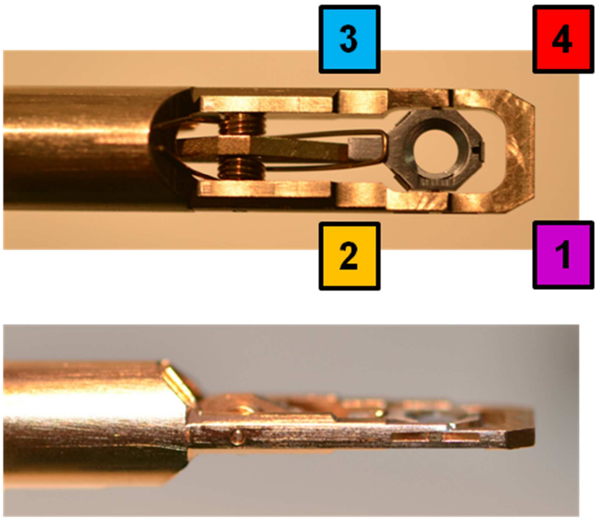

Figure 2.18: The Super-X HiVis holder in top view with indicated positions of the quadrants of the Super-X detector and in side view.

2.4.3 Further parameters

Further EDXS parameters that can be deduced from the analyses of spectra of a NiOx specimen on a Mo grid are the detection efficiency, the Fiori peak-to-background ratio and the Mo K/L ratio and they are discussed in this chapter.

Figure 2.19 displays the detection efficiency, in particular the Ni Kα intensity normalized to the acquisition time and the beam current for the Si(Li) and the Super-X detector for high voltages of 80 kV, 200 kV and 300 kV. As already described above (see chapter 2.2.3 and 2.3.1) the Super-X detector has a substantially higher detection efficiency in comparison to the Si(Li) detector. Additionally, in this graph the X-ray generation dependence on the high voltage can be seen. The lower the beam electron energy the higher is the ionization cross-section.

An important parameter for the quality of an EDXS system and its detection sensitivity is the peak-to-background ratio (P/B ratio), which provides another measure of the performance of an EDXS system. The Fiori P/B ratio is defined as the peak intensity above background divided by the background intensity at a single channel. With a NiOx specimen, the Ni Kα peak is the most suitable for the accurate calculation of the Fiori P/B ratio (Bennett & Egerton, 1995). Figure 2.19 depicts the Fiori P/B ratio for the Si(Li) and the Super-X detector for the three possible high voltages. The higher the Fiori P/B ratio is the better is the performance of the EDXS system. The Si(Li) detector shows the lowest Fiori P/B ratio. For the

Super-X detector a dependence on the high voltage can be seen. The Fiori P/B ratio is highest for the highest high voltage of 300 kV and decreases with decreasing high voltage. Thus the lowest Fiori P/B ratio has the lowest high voltage of 80 kV. This high tension dependence arises from the generation of the characteristic X-rays and the bremsstrahlung X-ray background which depends both on the high tension via the respective cross-sections. The P/B ratio plays an important role for the detection sensitivity and the minimum detectable amount of a particular element. The influence of the P/B ratio on the detection sensitivity is discussed in chapter 2.5.

Additional to the Ni and O signals of the NiOx specimen Mo signals are detected in the EDX spectra. This Mo signal originates from the specimen grid. Characteristic X-rays of Mo can be produced by (i) stray X-rays and (ii) stray electrons. High energetic bremsstrahlung X-rays rather generate high energetic Mo Kα X-rays whereas stray electrons rather excite Mo Lα than Mo Kα X-rays. Thus the Mo K/L ratio gives information about the stray radiation of the system. Stray X-rays produce a high Mo K/L ratio whereas stray electrons lower the ratio. Figure 2.19 displays the Mo K/L ratio for the Si(Li) and the Super-X detector for different high voltages. The Si(Li) has a higher Mo K/L ratio than the Super-X detector. They are two different TEM-EDXS systems with different geometries and illumination conditions and thus different stray radiation. For the Super-X detector again a dependence on the high voltage is visible. The higher the high voltage, the higher is the Mo K/L ratio.

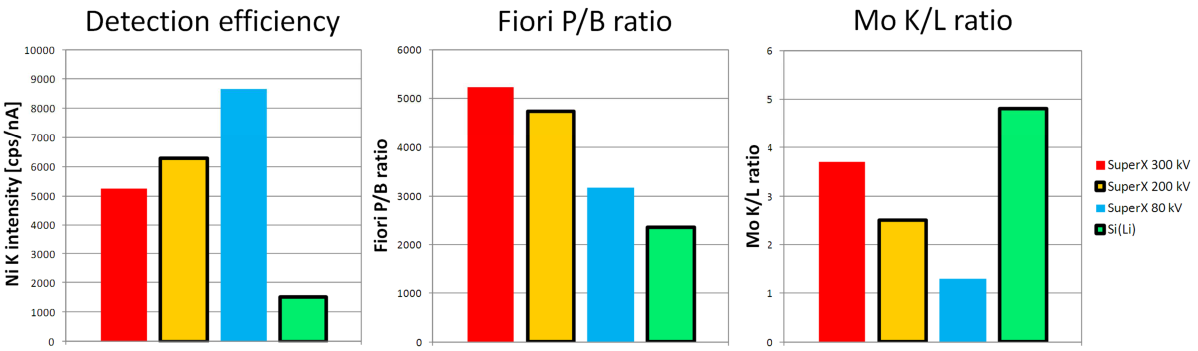

Figure 2.19: Detection efficiency, Fiori peak-to-background ratio and Mo K/L ratio of the Si(Li) and the Super-X detector for high voltages of 80 kV, 200 kV and 300 kV.

2.5 Detection sensitivity

The detection sensitivity can be described by the minimum amount of a particular element that can be detected with the TEM-EDXS system. One parameter describing the smallest detectable amount is the minimum mass fraction (MMF). The smaller the MMF is the more sensitive is the TEM-EDXS system to detecting trace elements.

On the one hand the MMF can be related to the practical aspects of analysis through the expression of Ziebold (Ziebold, 1967):

$$MMF \propto \frac{1}{\sqrt{P \cdot (P/B) \cdot n \cdot \tau}} \tag{2.7}$$

P … peak intensity
P/B … peak-to-background ratio
n … number of analysis
τ … acquisition time

To minimize the MMF the parameters of the denominator need to be raised. To increase the peak intensity either the beam current can be increased and/or a thicker specimen region can be analyzed. The P/B ratio can be increased by working at higher high voltages as explained in chapter 2.4.3. The other parameters are the acquisition time and the number of analyses which are in direct control of the operator.

On the other hand the MMF can be defined by a purely statistical criterion. If the peak intensity is greater than three times the standard deviation of the counts of the background than the peak is present. Thus following equation is valid for the MMF:

$$MMF = \frac{3 \cdot \sqrt{2 \cdot I_b} \cdot c}{I - I_b} \tag{2.8}$$

c … concentration of element of interest
I … intensity of element of interest
I_b … background intensity

For our TEM-EDXS systems the MMFs were determined by analyzing a well defined NIST SRM 611 standard containing around 500 ppm of 61 elements (Ti, V, Cr, Mn, Fe, Co, Ni, Cu, Zn, Ga, Ge, As, etc.) embedded in glass (Reed, 1992). EDX spectra were acquired for different beam currents, specimen thicknesses, acquisition times and high voltages for both EDXS systems. In Figure 2.20 EDX spectra of the NIST standard are shown for the Si(Li) and the Super-X detector for different high voltages. For all four spectra the beam currents were about 1 nA, the specimen thicknesses were about 190 nm and the illuminated specimen areas were 0.1 µm², the acquisition times were 600 s and 300 s for the Si(Li) and the Super-X detector respectively. In Figure 2.20 the EDX spectra are displayed with intensities normalized to the acquisition time and the beam current and the trace elements are detectable in all four EDX spectra. Unfortunately certain trace elements are superimposed by stray radiation.

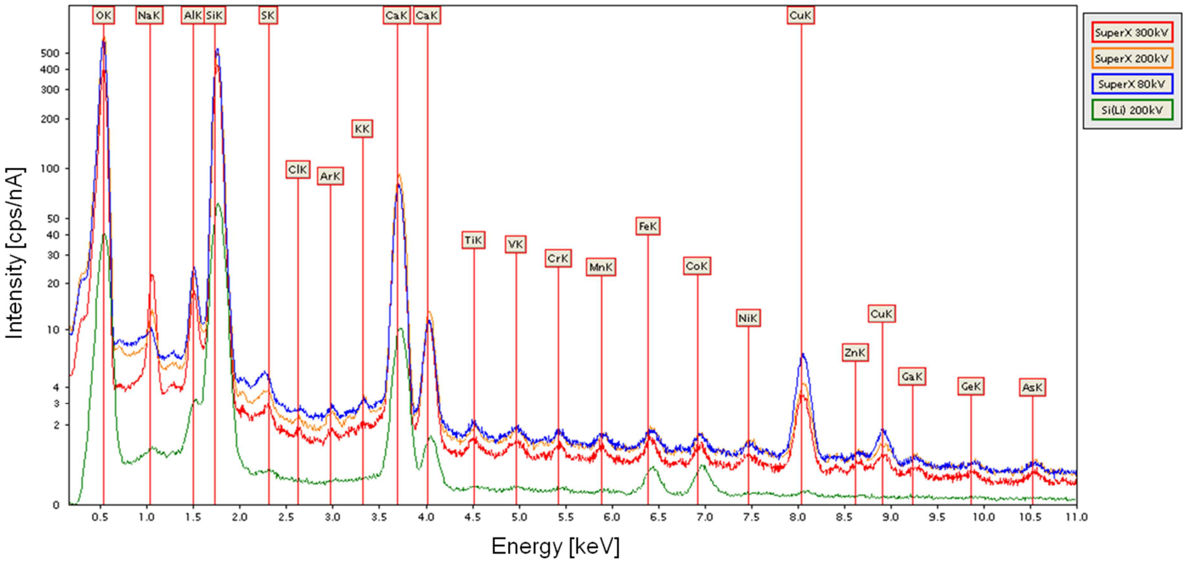

Figure 2.20: EDX spectra of a NIST SRM 611 standard acquired with the Si(Li) detector (green), the Super-X detector at 80 kV (blue), 200 kV (orange) and 300 kV (red) in logarithmic scale.

Various EDX spectra were analyzed and the normalized intensity of the elements Ti, V, Ni, Ge and As are displayed in Figure 2.21 for the Si(Li) and the Super-X detector at the three possible high voltages of Titan^3. The measured intensities for Ti are 1 cps/nA for the Si(Li) detector and for the Super-X 12 cps/nA, 14 cps/nA and 16 cps/nA for 300 kV, 200 kV and 80 kV, respectively. Thus it could be once more shown that the Super-X detector with its better detection efficiency reveals significant higher intensities for all detectable elements. Again the dependence of the intensity on the beam electron energy is obvious.

Using equation (2.8) the MMFs were calculated for the elements Ti, V, Ni, Ge and As measured for the 4 possible TEM-EDXS setups. The results of the MMFs are displayed in Figure 2.21. The Si(Li) detector exhibits higher MMFs for all elements in comparison to the Super-X detector. Comparing at 200 kV, the MMF of the Si(Li) detector is by a factor of 2.4 worse.

The detection sensitivity of the Super-X detector is significantly higher and trace elements can be detected in much shorter times and better statistics. Only 50 – 60 ppm of Ti, V and Ni are detectable using the Super-X detector. Again a dependence on the high voltage can be seen in the results of the MMFs. For the minimum detectable amount of a material the P/B ratio (see equation (2.7)) plays a decisive role. As The P/B ratio increases with increasing high voltage (see chapter 2.4.3) the MMF at 300 kV is better than at 80 kV although the normalized intensity is higher at 80 kV.

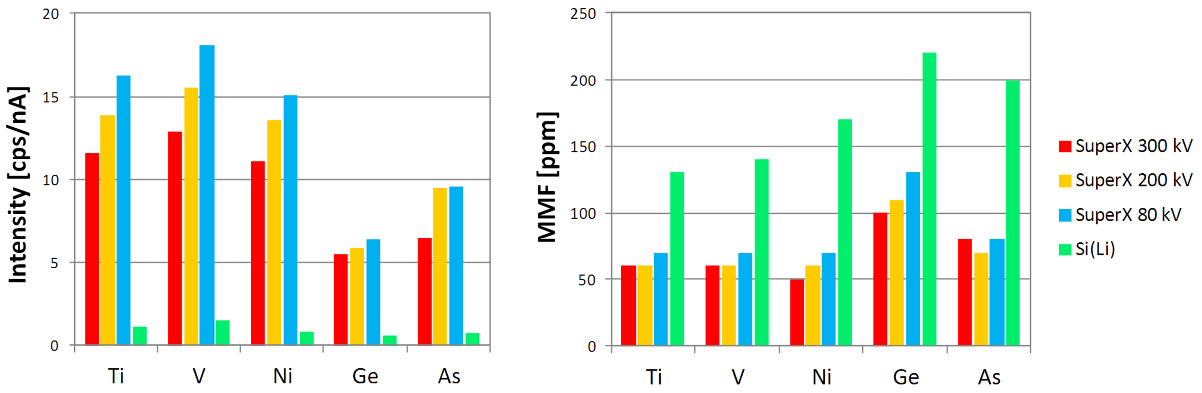

Figure 2.21: Normalized intensity and minimum mass fraction for different elements of the NIST SRM 611 standard (Ti, V, Ni, Ge and As) for the Si(Li) (green) and the Super-X detector at 80 kV (blue), 200 kV (orange) and 300 kV (red).

2.6 Coherent bremsstrahlung

The bremsstrahlung spectrum is known as a smooth, slowly varying intensity distribution as function of the energy, see chapter 2.1 and equation (2.2). This assumption is perfectly reasonable when bulk polycrystalline materials are analyzed by electrons with energies < 30 keV. If thin crystalline specimens are investigated using high energetic electrons it is possible that the generated bremsstrahlung spectrum contains small peaks known as coherent bremsstrahlung (CB). The CB signal can be used to deduce a geometrical parameter of the TEM-EDXS system being the take-off angle. (Williams & Carter, 1996)

The CB effect has been experimentally proven for high energy particle physics (MeV – GeV) in 1962 (Barbiellini et al., 1962). In 1983 CB was detected for the first time in TEM (Spence et al., 1983) and Pantel (Pantel, 2011) recently published a work investigating CB for Si under various acquisition conditions.

Figure 2.22 describes the generation of CB. An electron traveling with a speed v parallel to the atomic row of a single crystal with the atoms placed at equal distance L encounters at time t_0 the potential field of a “first” atom. As a consequence a bremsstrahlung X-ray X_1 is emitted and travels at speed c. At time $t_0 + L/v$ the electron interacts with a “second” atom and a second bremsstrahlung X-ray X_2 is emitted. If the path difference of these two bremsstrahlung X-rays traveling in direction to the EDXS detector is equal to an integer multiple of their wavelength, then they will add up coherently when arriving at the detector. Due to the periodic collision along the trajectory of the electron coherent bremsstahlung is emitted. (Pantel, 2011)

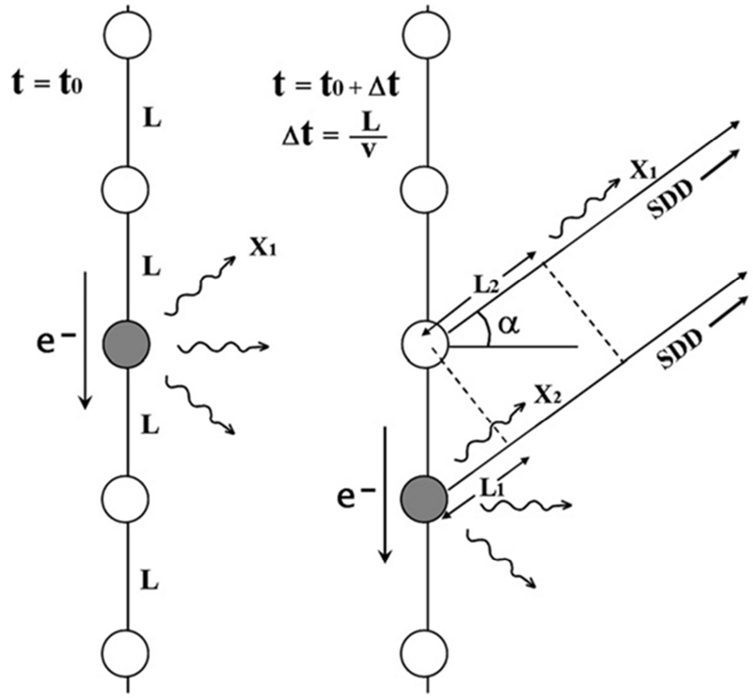

Figure 2.22: Representation of an electron traveling along an atomic row producing bremsstrahlung. The EDXS detectors collect the X-rays in the direction indicated by the take-off angle α. (Pantel, 2011)

According to these circumstances the following equation describes the energy of CB peaks (Reese et al., 1984):

$$E_{CB}(keV) = \frac{n \cdot 12{,}4 \cdot \beta}{L(\text{Å}) \cdot [1 - \beta \cdot cos(90 + \alpha)]} \tag{2.9}$$

E_{CB}(keV) … energy of coherent bremsstrahlung peak in keV
n … index of coherent bremsstrahlung peak
β … electron velocity divided by the velocity of light
L(Å) … real lattice spacing in the beam direction
α … take-off angle of EDXS detector

The CB energy depends on the lattice periodicity of the crystalline specimen along the beam trajectory, the electron speed that depends on the high voltage and the geometry of the TEM-EDXS system being expressed as the take-off angle. As the CB intensity is a very weak signal, the detection of CB was limited in older EDXS systems due to the low detection efficiency and the necessity to tilt the specimen.

For the investigation of CB peaks and subsequent determination of the take-off angle the Super-X detector was chosen as it obtains a high detection efficiency and there is no need of tilting the specimen for EDXS acquisition. A single crystalline Si specimen was investigated in

[100] zone axis as the CB peak intensity is highest when the beam is close to a low-index zone axis. To orient the Si specimen in zone axis α was tilted to 3.1° and β to 0.0°. As the tilt angles are quite small all quadrants see big solid angles. For the acquisition the Titan³ was operated at a high voltage of 300 kV, a beam current of 0.6 nA and an acquisition time of 15 min were chosen. The count rate for each quadrant was in the range of 7 – 11 kcps, thus giving a count rate of 35 kcps for the entire Super-X detector. Despite the high count rate the acquisition time was required to be 15 min as the CB is a very low signal. Thus large specimen areas of 2 – 10 µm² were scanned during EDXS acquisition to minimize radiation damage. Figure 2.23 shows one of several EDX spectra of Si [100] with above mentioned acquisition parameters. The Si peak, the sum peak of Si (2xSi), stray radiation (Fe, Co, Cu), signals from the contact layer (Al) and the CB peaks manifesting as periodic peaks with decreasing intensity (1, 2, 3 and 4) are indicated. The spectrum is displayed using a logarithmic intensity scale to display the Si and the CB peaks and their intensity difference in one spectrum. The intensity of the second CB peak is only 0.3 % of the intensity of the Si K peak.

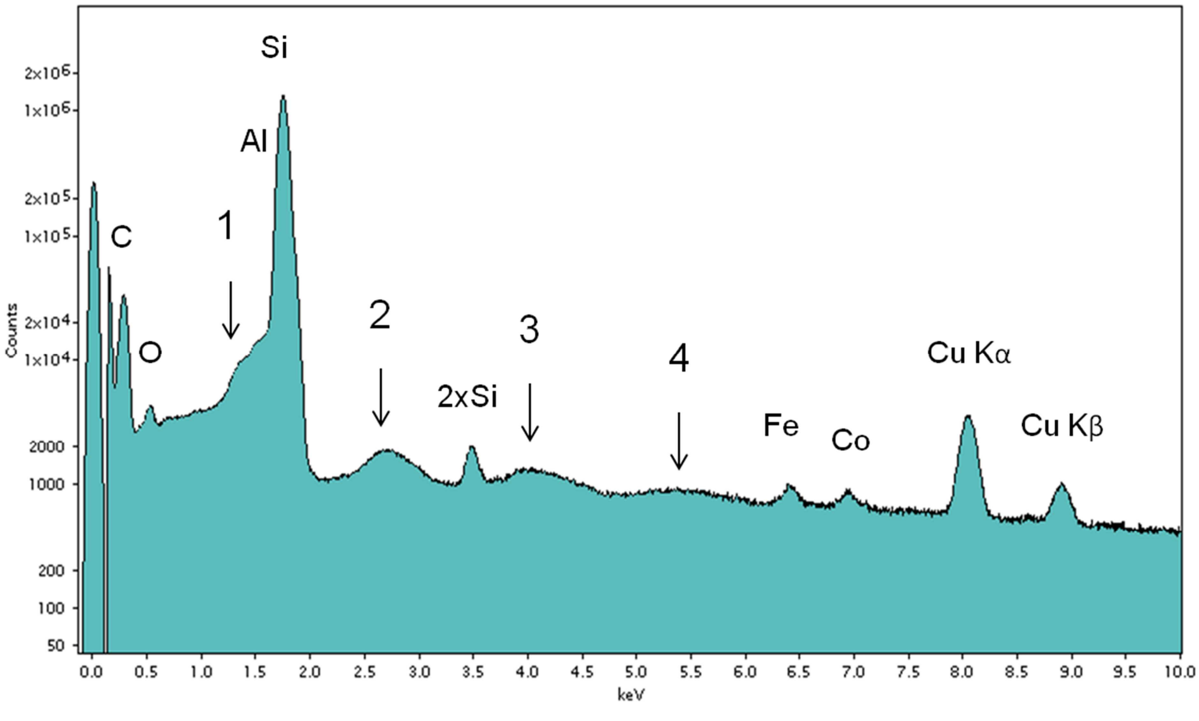

Figure 2.23: EDX spectrum of Si in [100] zone axis acquired with the Super-X detector and indicated coherent bremsstrahlung peaks (1, 2, 3 and 4).

The first CB peak overlaps for this acquisition conditions with the Si K peak. Thus the CB peaks starting with the second were extracted from the spectrum for further analysis. The extracted CB peaks can be seen in Figure 2.24. According to equation (2.9) the CB peaks were used to determine the take-off angle. Corresponding to FEI the Super-X detector has an elevation angle of 18° and a detector angle of 5° when installed in a Titan³. This means that the normal of the detector face is not parallel to the line between the specimen and the detector or in other words the X-rays arriving at the detector do not impinge under an angle of 90°. This geometrical circumstance causes that the CB peaks are asymmetrical. If the detector would be mounted in such a way that the X-rays impinge under an angle of 90° the CB peaks would be symmetrical. The widths of the CB peaks originate from the take-off angle range (minimum to maximum take-off angle).

The median, minimum and maximum take-off angles were calculated by applying equation (2.9). The lattice spacing for Si [100] is 5.431 Å and $\beta = 0.777$ for 300 kV. The median take-off angle was determined by using the energy values of the peak maxima of the second, third and fourth CB peak of various EDX spectra. The average take-off angles analyzed from the different CB peaks were consistent and thus a median take-off angle was found reproducibly being $\alpha_{median} = 23.8° \pm 0.5°$. The minimum and maximum take-off angles were determined by using the peak feet of only the second CB peaks, as the third and fourth are not as defined as the second CB peak. As results $\alpha_{min} = 12° \pm 3°$ and $\alpha_{max} = 40° \pm 3°$ were obtained. The take-off angles are indicated in Figure 2.24.

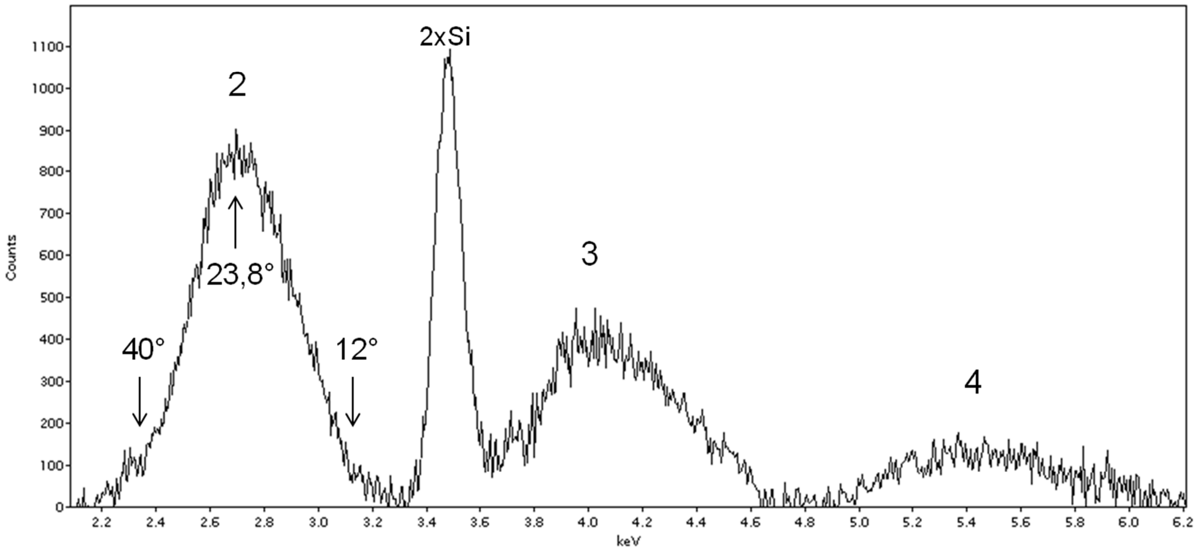

Figure 2.24: Detail of the second, third and fourth coherent bremsstrahlung peaks of Si [100] together with the Si sum peak and indicated minimum, median and maximum take-off angles.

Differences in the take-off angles appear when comparing the experimentally determined take-off angles with the geometrical information obtained from FEI. The same deviations between experimentally determined and nominal take-off angles were already published in the paper of Pantel (Pantel, 2011). Furthermore the experimentally determined minimum take-off angle is higher than the angle expected from the detector geometry. This is probably due to shadowing of the Super-X HiVis specimen holder, which was already claimed analyzing the solid angle of the detector (see chapter 2.4.2).

3 Organic semiconducting devices

The field of organic electronics evolved in recent years due to its potential of low production costs, flexible devices and device miniaturization. Thus organic semiconducting devices already cover a huge number of applications as organic solar cells (Brabec et al., 2001, Peumans et al., 2003), organic thin film transistors (Dimitrakopoulos & Malenfant, 2002, Klauk, 2010), organic light emitting devices (Burroughes et al., 1990, Friend et al., 1999), organic opto-chemical sensors (Wolfbeis, 2005, McDonagh et al., 2008), etc.

The performance and efficiency of organic electronic devices depend on several aspects, such as intrinsic material properties, the topography and roughness of the interfaces as well as the thicknesses of the individual layers. Especially the roughness of organic/metal interfaces and material diffusion distinctly influence the device performance. Furthermore, the influence of organic blocking layers introduced into device structures in combination with different deposition techniques of metal electrodes are of particular importance. (Fladischer et al., 2012)

To elucidate these parameters influencing the device performance different investigation methods are used. In this work different techniques like TEM, scanning electron microscopy (SEM), atomic force microscopy (AFM) and X-ray scattering techniques like X-ray reflectivity (XRR) and grazing incidence X-ray diffraction (GIXD) were used to perform nanoanalytical characterization.

In this work a product of the successful collaboration of the research project cluster ISOTEC was investigated, which is an organic opto-chemical sensor (Lamprecht et al., 2010, Lamprecht et al., 2011, Kraker et al., 2008). Such sensors are able to detect oxygen, carbon dioxide, pH, temperature and ammonia. Thus they are used in wide-ranging applications in chemical and biological analysis and clinical diagnostics utilized in medicine, food industry and environmental technologies. (Wolfbeis, 2005, McDonagh et al., 2008)

A typical organic opto-chemical sensor is composed of an organic light emitting device (OLED) as the light source and an organic photodiode (OPD) as the detection unit in combination with a sensor spot (Savvate'ev et al., 2002, Pais et al., 2008). During the ISOTEC project the integration of a ring-shaped OPD for fluorescence detection in a multisensor chip was developed. The schematic setup and a photographic picture of six organic opto-chemical sensors are shown in Figure 3.1. Light generated by an OLED, illuminating the sensor spot through the central hole of the OPD ring, is absorbed by the fluorescent molecules of the sensor material. Depending on the luminescent concentrators fluorescence light is partly reemitted into the substrate. The substrate serves as a waveguide and guides the fluorescence light to the ring-shaped OPDs. The special ring-shaped design of the OPDs guarantees that the majority of the fluorescent light is collected. As the OPDs are integrated on the opposite substrate side of the sensor spot, the OPDs are protected from the gas contamination of the analysis. According to the detected fluorescence light an electrical signal arises at the OPD. Sensor schemes using this special design for the chemical parameters carbon dioxide, pH, temperature and ammonia utilizing this sensor platform are proposed in the publications of Kraker et al. and Lamprecht et al. (Kraker et al., 2008, Lamprecht et al., 2010, Lamprecht et al., 2011).

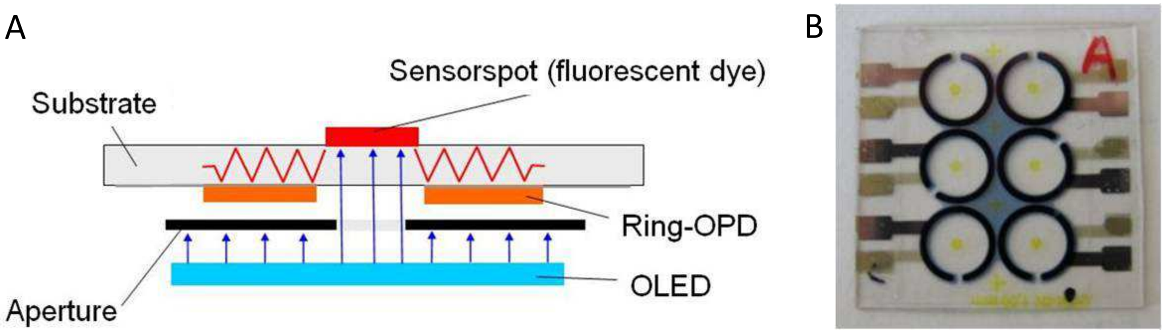

Figure 3.1: A) Schematic setup of an organic opto-chemical sensor and B) photographic picture of an organic opto-chemical sensor array.

3.1 Organic photodiode

In this work organic photodiodes used as detection units in organic opto-chemical sensors were characterized with regard to the appearance of the different interfaces and the thicknesses of the individual layers. Furthermore, material diffusion and the influence of different organic blocking layers introduced into the device structures in combination with different deposition techniques of metal electrodes were studied.

As this work is the product of the results of different investigation methods and the collaboration of different scientists, the involved scientists and their contributions are outlined in this paragraph. The production of the devices and their electrical characterization (I-V measurements and four-point probe measurements) were performed by E. Kraker and B. Lamprecht from the Institute for Surface Technologies and Photonics of the Joanneum Research Forschungsgesellschaft. The X-ray measurements were performed by A. Neuhold and R. Resel from the Institute of Solid State Physics of the Graz University of Technology. The following work was performed at the Institute of Electron Microscopy and Nanoanalysis of the Graz University of Technology: SEM investigations by S. Mitsche and A. Reichmann, specimen preparation using the focused ion beam (FIB) instrument by M. Sezen and T. Haber, specimen preparation using ultramicrotomy by C. Mayrhofer and TEM as well as AFM investigations by me.

In our case, the setup of the OPD is based on the well-known Tang photodiode (Tang, 1986), consisting of stacked layers of copper phthalocyanine (CuPc, p-type material) and perylene tetracarboxylic bisbenzimidazole (PTCBi, n-type material). A thin Au layer was used as semitransparent bottom electrode and an opaque Ag layer was deposited as top electrode. As additional layers between the organic stack and the cathode are reported to improve the device performance (Song et al., 2005), tris-8-hydroxyquinolinato-aluminum (Alq_3, n-type material) was introduced as a blocking layer between the organic stack and the cathode. During the period of this work the organic blocking layer material was changed to 4,7-diphenyl-1,10-phenanthroline (Bphen, n-type material) (Huang et al., 2006), as this material exhibits better blocking layer properties in our setup. Figure 3.2 shows a schematic diagram and the working principle of an OPD and a photographic picture of six OPDs using Alq_3 as blocking layer.

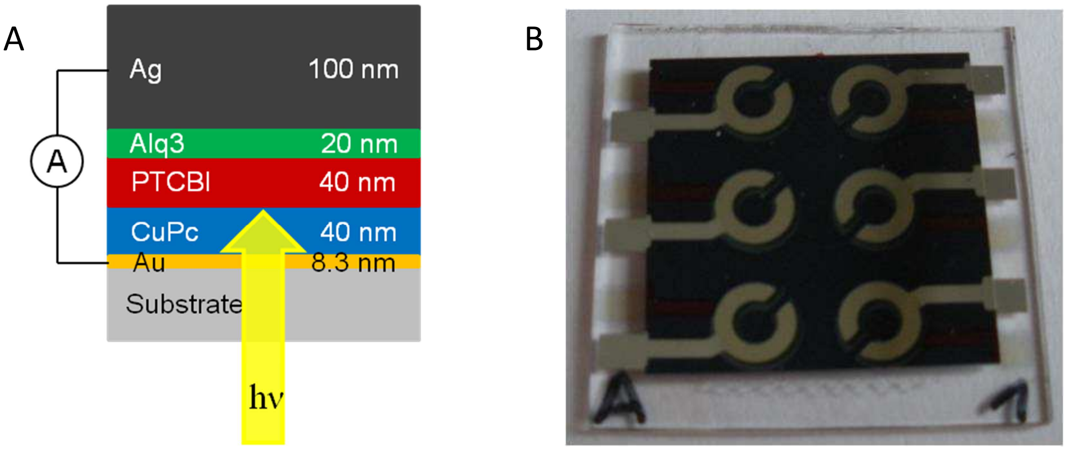

Figure 3.2: A) Schematic diagram and B) photographic picture of organic photodiodes

All samples were produced in a high-vacuum clustertool (Oerlikon Leybold Vacuum GmbH) including a metal deposition chamber (electron beam deposition (EBD), ion beam sputtering (IBS) and vacuum thermal evaporation (VTE)) and an organic material deposition chamber (4 effusion cells). A transfer chamber connects the metal and the organic deposition chamber without breaking the vacuum during the whole sample fabrication procedure. All evaporated layers were thus prepared under high vacuum conditions (1×10^{-6} mbar) at room temperature by rotating the substrate to ensure homogeneous coating. The film thickness was controlled with a quartz thickness gauge.

For the OPDs, either thermally oxidized silicon (SiO_2), microscope glass slides or Mylar were used as substrates. For the semitransparent anode, a Au layer was deposited by sputtering. The organic layers CuPc (p-type semiconductor, purchased from Fluka), PTCBi (n-type semiconductor, purchased from Sensient Imaging Technologies GmbH), Alq_3 and Bphen (blocking layers, both purchased from Sigma Aldrich) were evaporated by VTE. As top-electrode an opaque Ag layer was deposited with an area of 9 mm^2, which determines the active device area.

In the period of my work not only the blocking layer material was changed but also the layer thicknesses due to performance improvements. At the beginning the nominal thicknesses indicated in Figure 3.2A were used triggered with a quartz thickness gauge. After some changes we ended up with 6 nm Au, 30 nm CuPc, 30 nm PTCBi, 37 nm Alq_3 or Bphen and 80 nm Ag. All layer thicknesses except for the blocking layer were reduced and the thickness of the blocking layer was increased. The chemical structures of the respective molecules and the layout of the OPDs are depicted in Figure 3.3.

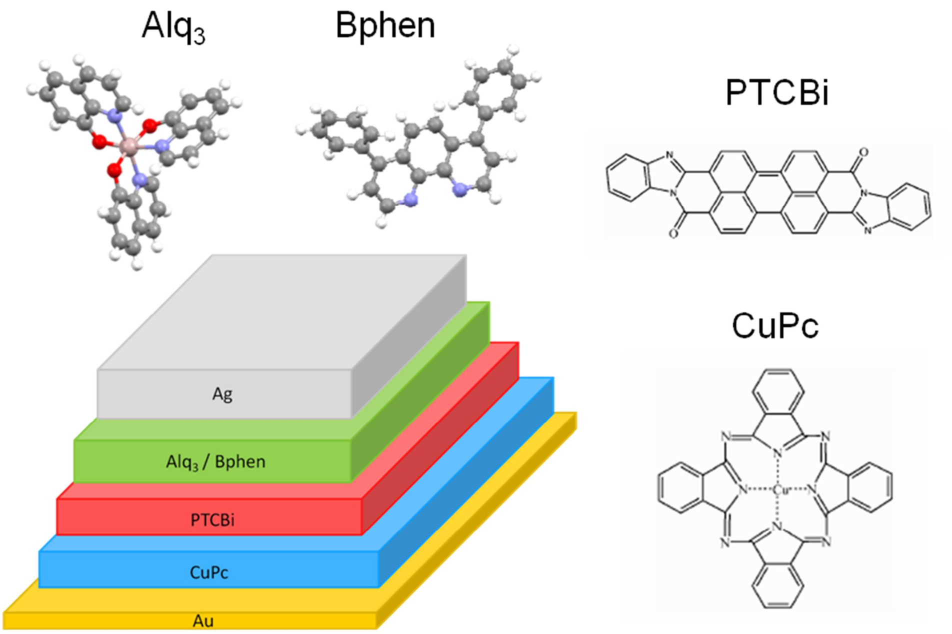

Figure 3.3: Layout of the organic photodiodes and chemical structures of CuPc, PTCBi and the blocking layer materials Alq_3 and Bphen.

3.2 Preparation of OPDs for TEM investigation

The preparation of organic semiconducting devices for TEM investigation is challenging as organic materials are very sensitive to both, beam and physical damage. To obtain cross-section specimens of the OPDS in this work two different preparation methods were used, ultramicrotomy and the focused ion beam (FIB) instrument.

3.2.1 Preparation of OPDs with flexible substrates

The first approach to prepare TEM cross-section specimens of OPDs on flexible substrates was ultramicrotomy. This method has the advantage of leaving the chemistry of the specimen unchanged and producing uniformly thin films of multiphase materials. The disadvantage of ultramicrotomy is the possible fracturing and deformation of the specimen.

In this work a lot of different attempts were made to get a reliable cross-section of the OPD by ultramicrotomy. For the attempts a Leica Ultracut UCT was used operated at both, room temperature and low temperature (cryo-ultramicrotomy). Different epoxy resins such as SpeziFix-40 Kit, Acrifix 192, Agar 100 Kit and Uhu+ were used additionally to different substrates (Mylar, PET and PMMA). Figure 3.4 shows TEM BF zero loss (ZL) filtered images of different cross-section preparations of the OPDs. In Figure 3.4A-C delaminations of the organic materials from either Au or Ag can be seen. In Figure 3.4D-F the OPDs do not show delaminations, but serious fractures and deformations. These fractures and deformations could not be avoided with any variation in the preparation. Note that the thin Au layer is always deformed and thus no reliable cross-section could be prepared.

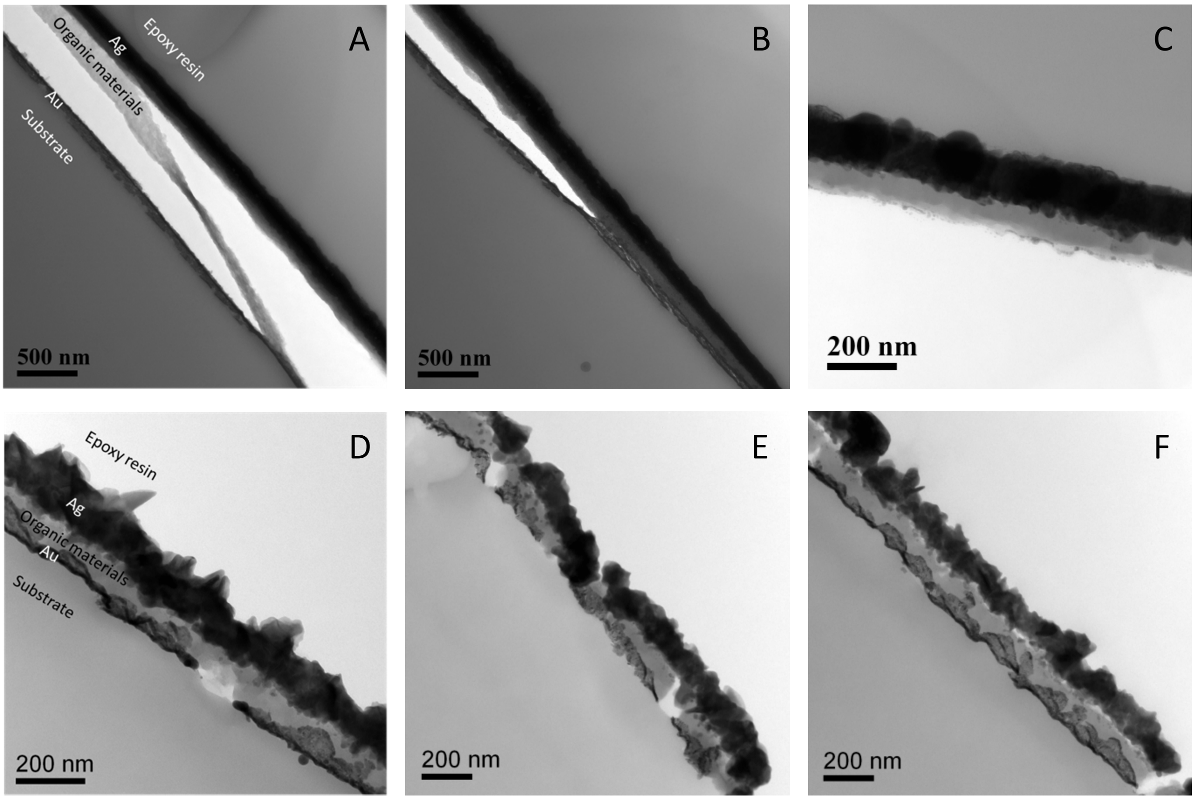

Figure 3.4: TEM BF ZL images of cross-sections of OPDs prepared by ultramicrotomy using different approaches. The specimens exhibit preparation artifacts such as delaminations (A-C) and fractures and deformations (D-F).

Unfortunately the disadvantages of ultramicrotomy could not be solved in our case for cross-section preparations of OPDs. Thus OPDs with flexible substrates were prepared in a FIB instrument.

An FEI FIB/SEM Dual Beam Microscope Nova200 was used for cross-section preparations of OPDs. The in situ lift-out technique (Langford & Clinton, 2004) was chosen to realize homogeneously thin cross-section lamellas. To protect the surface from ion beam damage Pt layers were grown in the FIB by electron-beam induced deposition followed by ion-beam assisted deposition. Figure 3.5A-C depict the conventional FIB preparation where the lamella is mounted at the side of the grid bar. To maintain stability only a small window of the lamella consisting of soft materials is milled, which can be seen in Figure 3.5B. Nevertheless the lamella is bent, which is visible in top view in Figure 3.5C and again in Figure 3.12B.

Hence the mounting place of the lamella was changed from the side of the grid bar to the top of the grid bar to enhance the stability of the lamella. Figure 3.5D-F show a FIB preparation with the lamella mounted on top of the grid bar and again only a window was milled. Unfortunately this approach did not show the designated effect. Although the lamella is straight, the milled window is bent, which can be seen in Figure 3.5F and again in Figure 3.12F and G.

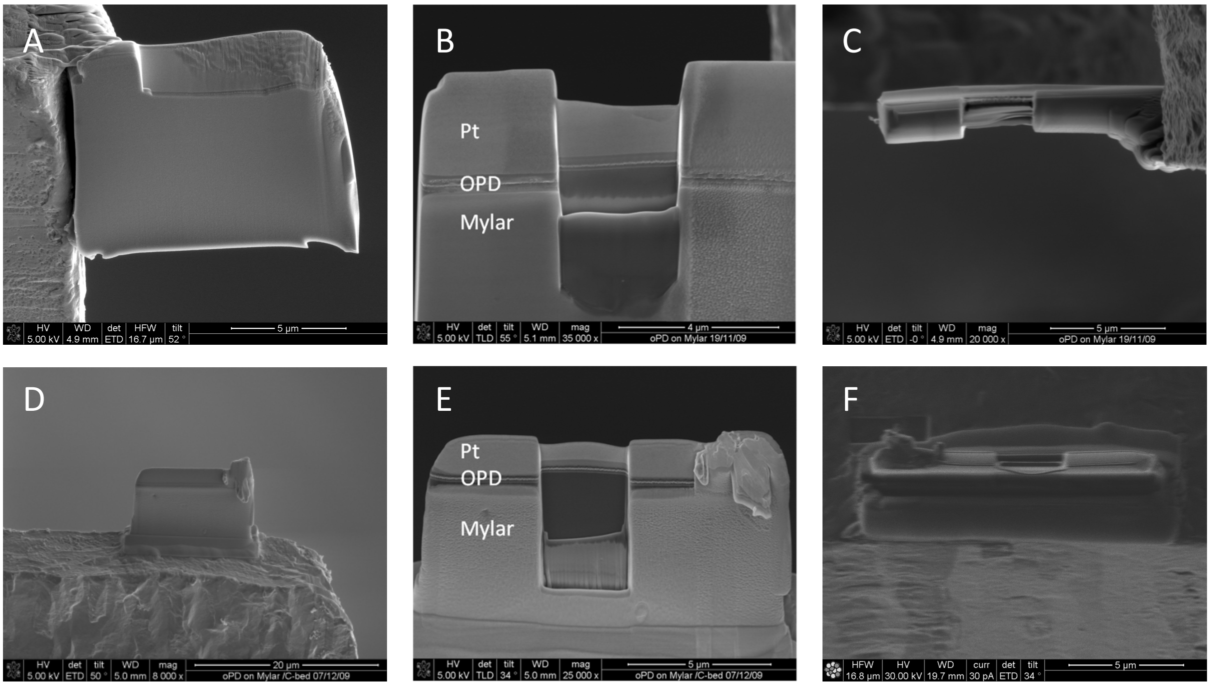

Figure 3.5: SEM images of cross-section preparations of OPDs using a FIB instrument. A-C) The specimen is mounted at the side of the grid bar and D-F) on top of the grid bar.

Our goal was to compare TEM results of the OPDs with results obtained from XRR investigations. Thus we changed to use silicon wafers with 150 nm thermally oxidized SiO_2 (from Siegert Consulting e.K.) as substrates because on the one hand undistorted cross-section preparation using the FIB is feasible and on the other hand the Mylar substrate of the OPDs did not allow reliable XRR investigations.

3.2.2 Preparation of OPDs with rigid substrates

The OPDs on Si/SiO_2 substrates were as well prepared by cross-section preparations in the FIB using the in situ lift-out technique. Figure 3.6A and C show STEM HAADF images of cross-sections of the OPD prepared in the FIB instrument. The EDX spectrum (Figure 3.6B) was acquired at the indicated region of Figure 3.6A. A Ag particle is located in the middle of the organic stack and additionally a significant amount of Pt is detected. Also the indicated regions in Figure 3.6C were proven to be Pt particles.

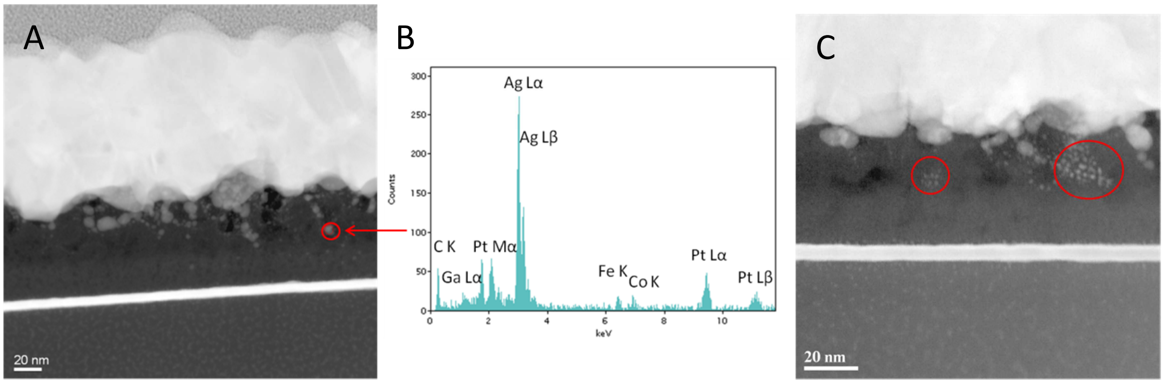

Figure 3.6: A,C) STEM HAADF images of cross-sections of OPDs prepared using a FIB and B) EDX spectrum of indicated analyzed region

These Pt particles originating from the protection layer and diffusing into the organic layer during the milling process are artifacts interfering the analysis of the organic materials. Additionally, diffusion of Ag particles is possibly enhanced by the milling process. Thus to avoid artificial ion beam induced Ag and Pt diffusion into the organic materials upside down milling was used for subsequent cross-section preparations of OPDs.

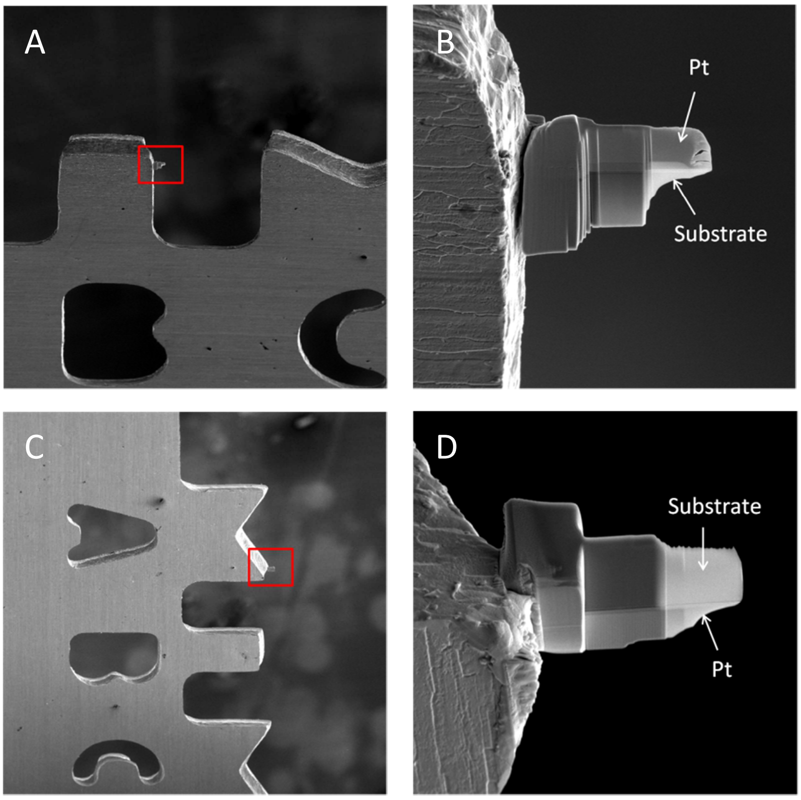

Figure 3.7: Cross-section preparations of OPDs using a FIB and A-B) conventional milling and C-D) upside down milling.

Figure 3.7 demonstrates the difference of FIB preparations using conventional (A and B) and upside down milling (C and D). In the case of conventional milling, the lamella is mounted at the grid bar and the milling process is performed in direction from the Pt protection layer down to the substrate. In the case of upside down milling, the lamella is mounted at the top of the grid bar under an angle of 90°. Then the whole grid is turned around by 180° and the milling is performed upside down in direction from the substrate to the Pt protection layer. Due to this upside down milling artificial ion beam induced Ag diffusion and diffusion of Pt into the organic materials were avoided.

Nevertheless organic materials are sensitive to beam damage and the preparation process using Ga ions can damage the material. Figure 3.8A displays a TEM BF ZL filtered image of an OPD exhibiting delamination of the organic layers, which is affirmed by the corresponding relative thickness map (Figure 3.8B) showing zero thickness for the delamination region. Although in most cases the cross-section preparation of OPDs worked properly using the FIB, damage cannot be prevented always.

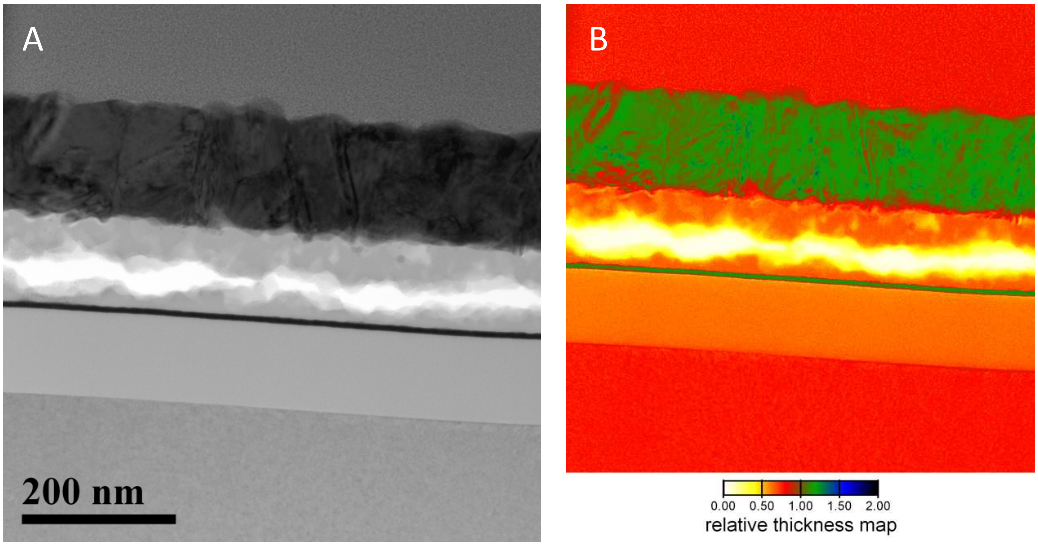

Figure 3.8: A) TEM BF ZL image and B) relative thickness map of the cross section of an OPD prepared using a FIB showing delamination of the organic layers.

In summary it can be said that in our case the cross-section preparation using the FIB worked properly when considering certain aspects, whereas ultramicrotomy did not yield reliable cross-section specimens for our OPDs. In the case of OPDs on flexible substrates the FIB preparation would have yielded proper cross-section lamellas if further refinements of the milled window size had been made concerning the stability aspect. But as these flexible substrates were not suitable for the XRR measurements, they were replaced by Si/SiO_2 substrates. Reliable cross-section lamellas of the OPDs on rigid Si/SiO_2 substrates can be prepared in the FIB instrument if upside down milling is used to avoid artificial ion beam induced Ag diffusion and diffusion of Pt into the organic materials in combination with low ion beam currents to prevent the organic materials from damage.

3.3 Challenges of OPDs concerning TEM investigations

The cross-section specimens of the OPDs posed challenges for the TEM investigations concerning the sensitivity of organic materials to beam damage, the hydrocarbon contamination and the alteration of Ag when exposed to ambient air. These three topics are discussed in the following three chapters.

3.3.1 Organic materials

A well-known fact is the sensitivity of organic materials to beam damage. Beam damage is a severe problem in TEM and its mechanisms are already well investigated and understood. Organic materials suffer mainly from radiolysis effects being inelastic electron-electron interactions breaking the chemical bonds, changing the structure and/or removing material (mass loss). (Egerton et al., 2004, Egerton, 2012) These effects may be attenuated but cannot be avoided completely.

In Figure 3.9 the effects of beam damage can be seen. Figure 3.9A and B display TEM BF ZL filtered images of a cross-section of an OPD before and after the acquisition of EFTEM images. On the one hand delamination between the Au and the organic layers is obvious as a result of beam damage and on the other hand deformations and contrast changes of the illuminated areas are clearly visible in Figure 3.9B. Figure 3.9C depicts the beam damage caused by STEM investigations. The indicated area represents the area of an EDXS line scan. The organic materials were damaged in such a drastic way, that no material remained along the line scan.

Beam damage was minimized by performing TEM investigations as fast as possible with dose rates being as low as possible. However, as a certain amount of signal is necessary to perform reliable analyses beam damage is always a crucial point.

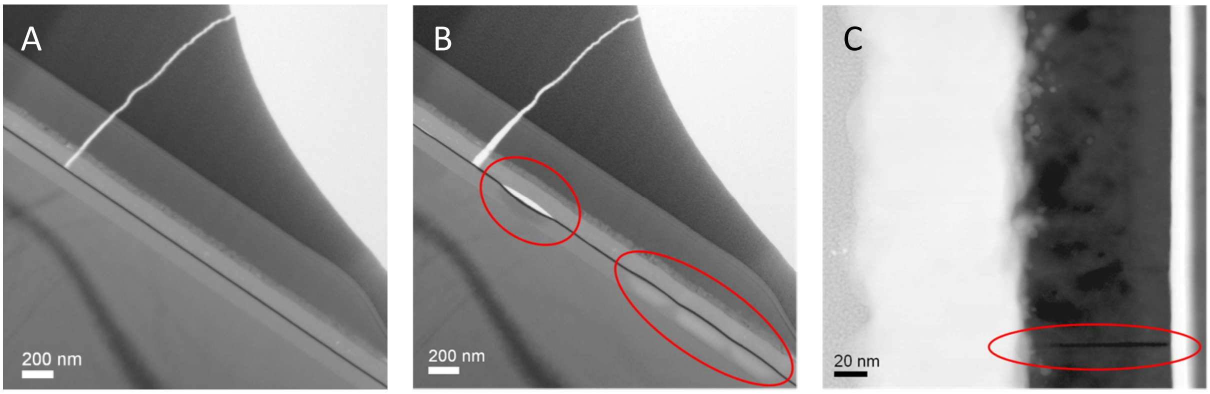

Figure 3.9: TEM BF ZL images of a cross-section of an OPD A) before and B) after TEM investigations and C) STEM HAADF image after an EDXS line scan.

3.3.2 Hydrocarbon contamination

Another problem every electron microscopist is confronted with is hydrocarbon contamination. Hydrocarbon molecules can be cracked under the electron beam and carbonaceous material deposits on the specimen. Sources of hydrocarbons and thus contamination are the microscope vacuum, the specimen holder and the specimen itself. Especially organic materials can easily introduce hydrocarbon contaminants resulting in contamination of the analyzed areas. (Egerton et al., 2004, Williams & Carter, 1996)

Depending on the conditions of the vacuum and the specimen more or less contamination occurs. Figure 3.10A and B show STEM HAADF images of cross-sections of OPDs and contamination of varying amount generated during the acquisition of line scans. Figure 3.10A only exhibits little contamination spots whereas Figure 3.10B shows a severe contamination trail. This severe contamination was additionally investigated in an SEM and is displayed in Figure 3.10C-E. Figure 3.10C and D show SEM images of the lamella in top view with the indicated illumination direction of the TEM electron beam and Figure 3.10E in side view. It is really amazing how the contamination forms on both sides of the lamella looking like a sword spearing the lamella and in which dimensions contamination can grow. In this case the contamination grew more than 1 µm yielding these fascinating images.

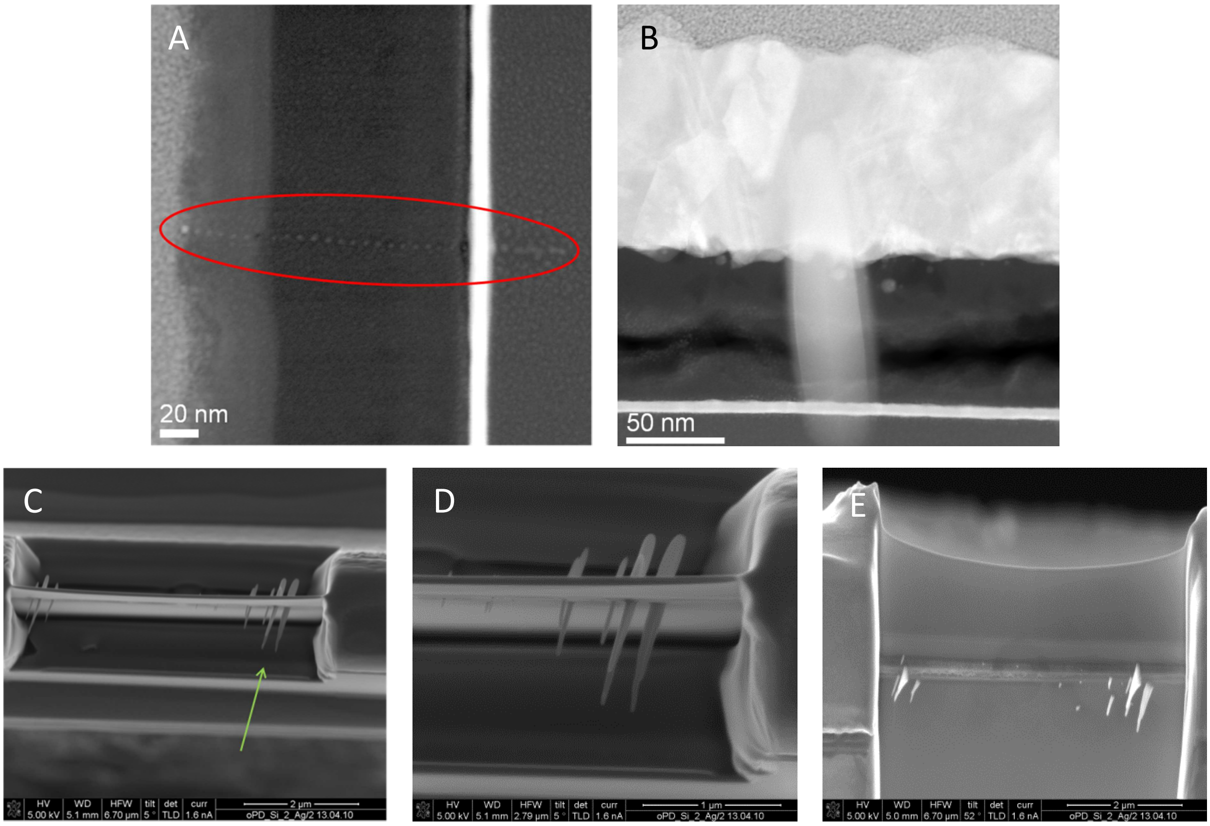

Figure 3.10: A,B) STEM HAADF images of the cross-section of OPDs and contamination trails of performed line scans. C-E) SEM images of the OPD lamella (B) displayed in C,D) top view with indicated illumination direction of the TEM electron beam (green arrow) and E) side view after STEM line scan investigations showing contamination spots.

3.3.3 Ag alteration

Additionally to the sensitive organic materials, also Ag which was used as a top contact material for the OPDs posed a challenge. Ag is known to tarnish when exposed to air containing hydrogen sulfide H_2S forming silver sulfide tarnish films. (Bennett et al., 1969) This phenomenon is well known thinking about the dark colored tarnish of silver coins or silver jewelry.

In microscopic dimensions this tarnishing effect can be seen in an impressive manner. The first time this tarnishing effect was detected in this work was when analyzing an OPD prepared by ultramicrotomy. Figure 3.11 displays a STEM HAADF image with the indicated area of an EDXS spectrum image (SI). Figure 3.11B and C show the Ag K and S K EDXS signals of the SI and an EDX spectrum of the Ag layer is displayed in Figure 3.11D. The analysis showed that the whole Ag layer exhibits a huge amount of S.

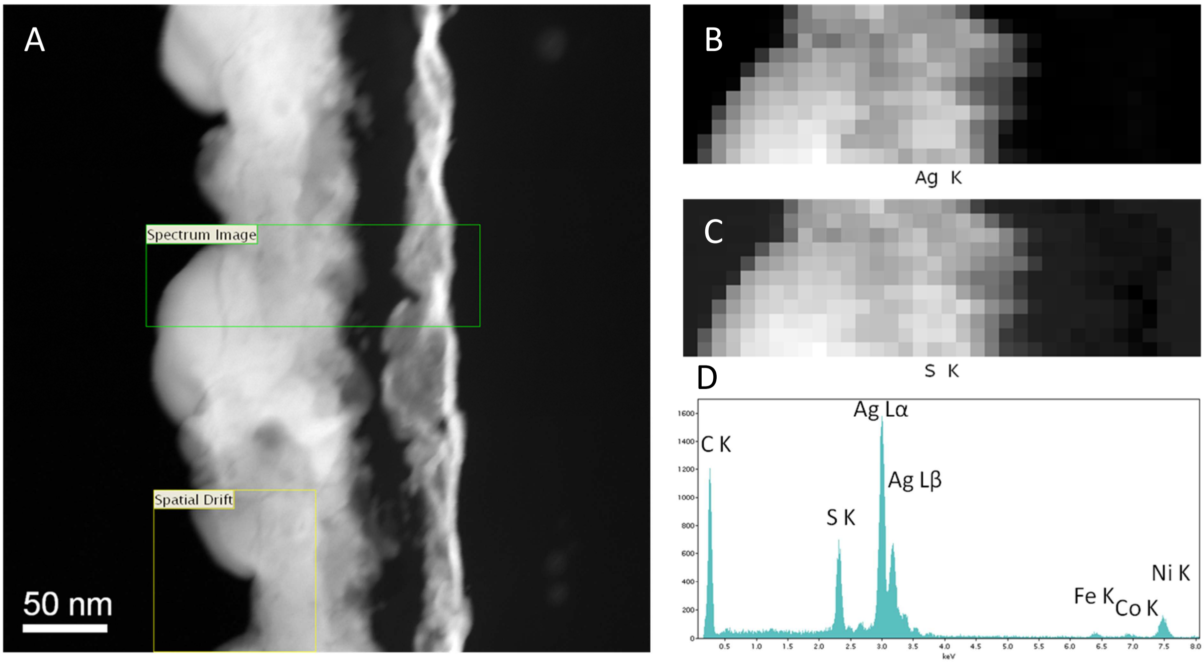

Figure 3.11: A) STEM HAADF image of an OPD prepared using ultramicrotomy and indicated area of the EDXS SI. SIs for B) Ag K and C) S K signals and D) an EDX spectrum of the Ag layer.

In a first step we believed that maybe the epoxy resin partakes in this effect. But this tarnish effect could also be detected in specimens prepared using the FIB. Figure 3.12 shows pictures of the Ag alterations. Figure 3.12A-C represent SEM images of an OPD lamella from both sides and in top view being the equivalent to the TEM BF ZL filtered image of Figure 3.12D. Equally the SEM images of Figure 3.12F and G are the equivalent to the TEM BF ZL filtered image of Figure 3.12E showing another OPD. Immense excrescences can be seen in all images. In the TEM images it can be seen that these excrescences cover the whole OPD inhibiting any analysis of the cross-section of the OPD. In the SEM images the immense expansions of these excrescences are clearly visible. EDXS analysis of these excrescences showed a huge amount of S and Ag similar to the EDX spectrum shown in Figure 3.11D.

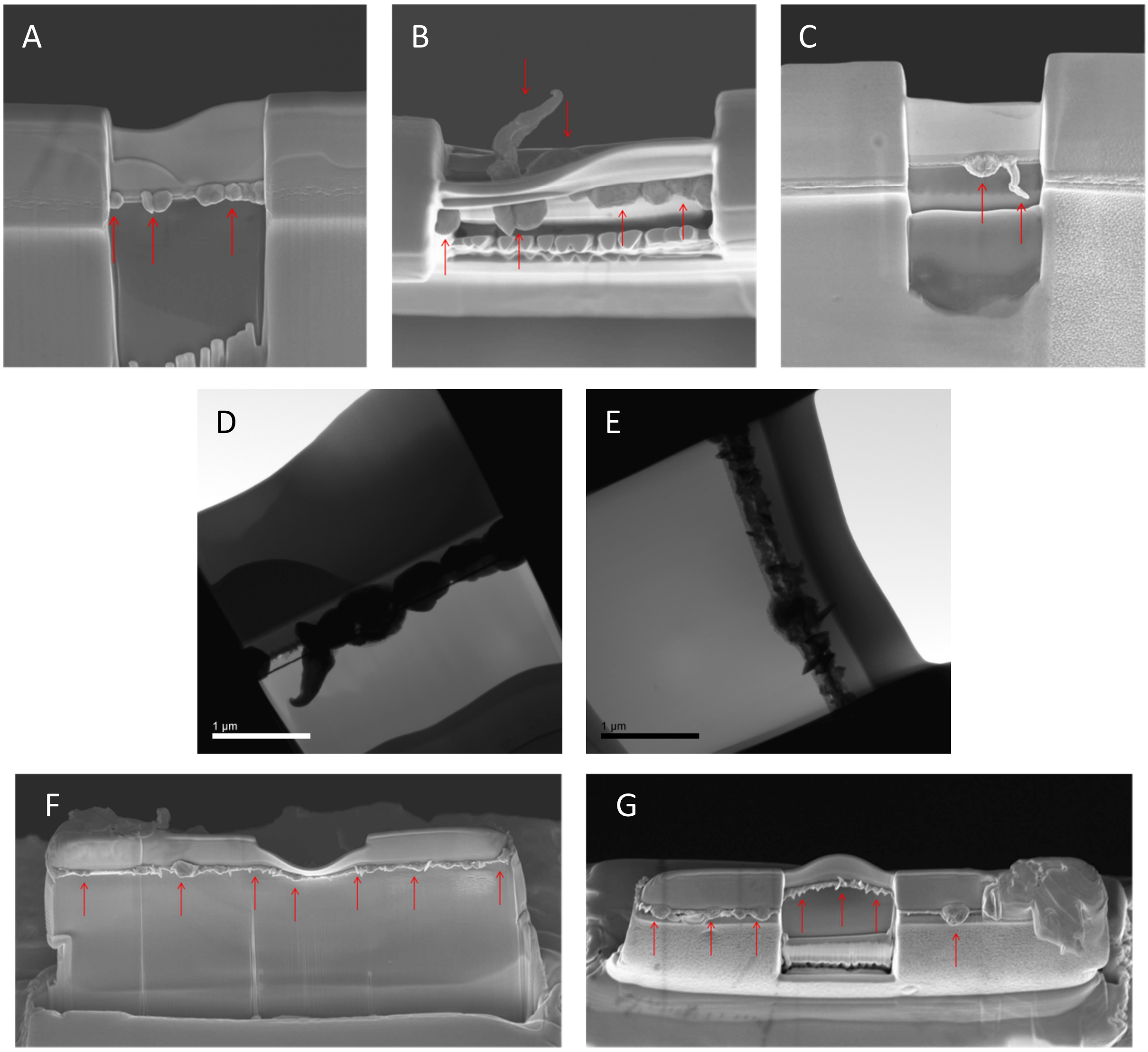

Figure 3.12: A-C,F-G) SEM images and D-E) TEM images of two OPDs prepared using the FIB and indicated Ag alterations.

These two lamellas were kept in ambient air for the period of time between the preparation in the FIB and the TEM investigation, which lasted 15 and 9 days respectively. As a consequence the tarnishing effect was initiated by the ambient air containing hydrogen sulfide. Figure 3.13 confirms the time dependence and the influence of the air as the cross-section of an OPD is shown immediately after the preparation in the FIB and 12 days later. Immediately after the preparation a homogeneously thin cross-section is visible with defined interfaces of the organic layers to the top Ag layer (Figure 3.13A). This lamella was stored in ambient air for 12 days and then again investigated in the TEM. In this time period in ambient air the Ag alternated significantly destroying the original Ag layer (Figure 3.13B).

As a consequence all further OPD cross-sections were investigated in the TEM immediately after the preparation in the FIB to avoid any tarnishing effects of Ag.

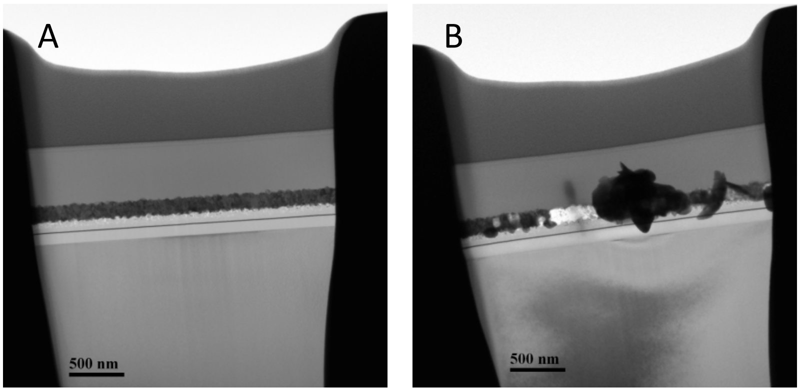

Figure 3.13: TEM images of the cross-section of an OPD acquired A) immediately after the preparation process and B) a couple of days later.

Despite the different challenges of the organic materials, the contamination and the Ag alteration reliable TEM results could be obtained by (i) performing the TEM investigation immediately after the preparation in the FIB, (ii) working with a clean specimen holder and a good vacuum and (iii) using low dose rates for the TEM investigations.

3.4 Nanoanalytical characterization of OPDs

In OPDs the topography and roughness of the interfaces as well as the thicknesses of the individual layers decisively influence the device properties. Thus these parameters of the multilayer system were elucidated using different investigation methods such as TEM, SEM, AFM and XRR. In addition GIXD was performed to characterize the crystallographic properties of the materials.

3.4.1 Interface topography, roughness and layer thickness

In this work we started with the characterization of the OPD using Alq_3 as blocking layer material, which is depicted in Figure 3.2A. For the determination of the topography and the roughness of the layers, samples were investigated after each processing step, i.e. for each layer a sample was prepared that consists of the relevant and the subjacent layers. We investigated the surfaces of these samples by SEM, AFM and XRR. The obtained results were published in the paper of Neuhold et al. (Neuhold et al., 2011).

SEM was performed with a Zeiss Ultra 55 microscope equipped with a FEG. The high resolution images were recorded with a high efficiency in-lens secondary electron detector at an acceleration voltage of 3 kV.

AFM measurements were performed on a Dimension 3100 microscope equipped with a hybrid closed loop scan head and a Nanoscope IVa controller (Digital Instruments, VEECO). All measurements were done in tapping mode with different Olympus cantilever (2 to 40 N/m) depending on the sample characteristics.

XRR measurements were performed at the Institute of Solid State Physics with a Bruker D8 Discover diffractometer setup in Bragg-Brentano configuration using Cu Kα radiation. GIXD experiments were performed at the G2 beamline at the synchrotron Cornell High Energy Synchrotron Source. A detailed description of the measurements and the analyses of XRR and GIXD data are described in the publication of Neuhold et al. (Neuhold et al., 2011).

SEM and AFM results are shown in Figure 3.14 for the five stacked layer systems. The topography is shown nicely in the SEM images. AFM investigations show similar topographies and furthermore lead to the roughness values of the individual stacked layer systems. The organic materials were challenging for the AFM measurements. After several different measurement settings the surfaces of the SiO_2_Au_CuPc and SiO_2_Au_CuPc_PTCBi stacks could be imaged nicely whereas the surface of the SiO_2_Au_CuPc_PTCBi_Alq_3 stack caused difficulties as the material is very soft and sticky and some distortions are still visible in the respective AFM image (Figure 3.14D). The root mean square (RMS) roughness values of the surfaces of the individual stacked layer systems determined from the AFM investigations are listed in Table 3.1 together with the roughness values obtained from XRR measurements.

The results of the different techniques are in good agreement and are displayed in Figure 3.14 and Table 3.1. It could be shown that the semitransparent Au layer (Figure 3.14A) is very smooth. CuPc crystallizes in the α-phase and forms islands on top of the Au layer resulting in a spherical grained surface (Figure 3.14B) with significantly increased surface roughness. PTCBi (Figure 3.14C) grows with randomly distributed crystallites in a worm-like structure on top of the spherical grained surface of CuPc. The deposition of amorphous Alq_3 does not lead to a new topography (Figure 3.14D); the worm-like structure of the subjacent PTCBi layer is adapted and the surface is flattened. The top Ag cathode exhibits a rough surface (Figure 3.14E). Thus it could be shown that the roughness increases with each layer except for amorphous Alq_3, which smoothes the surface a little bit. This roughness progression (Table 3.1) suits well with the topography resulting from SEM investigations.

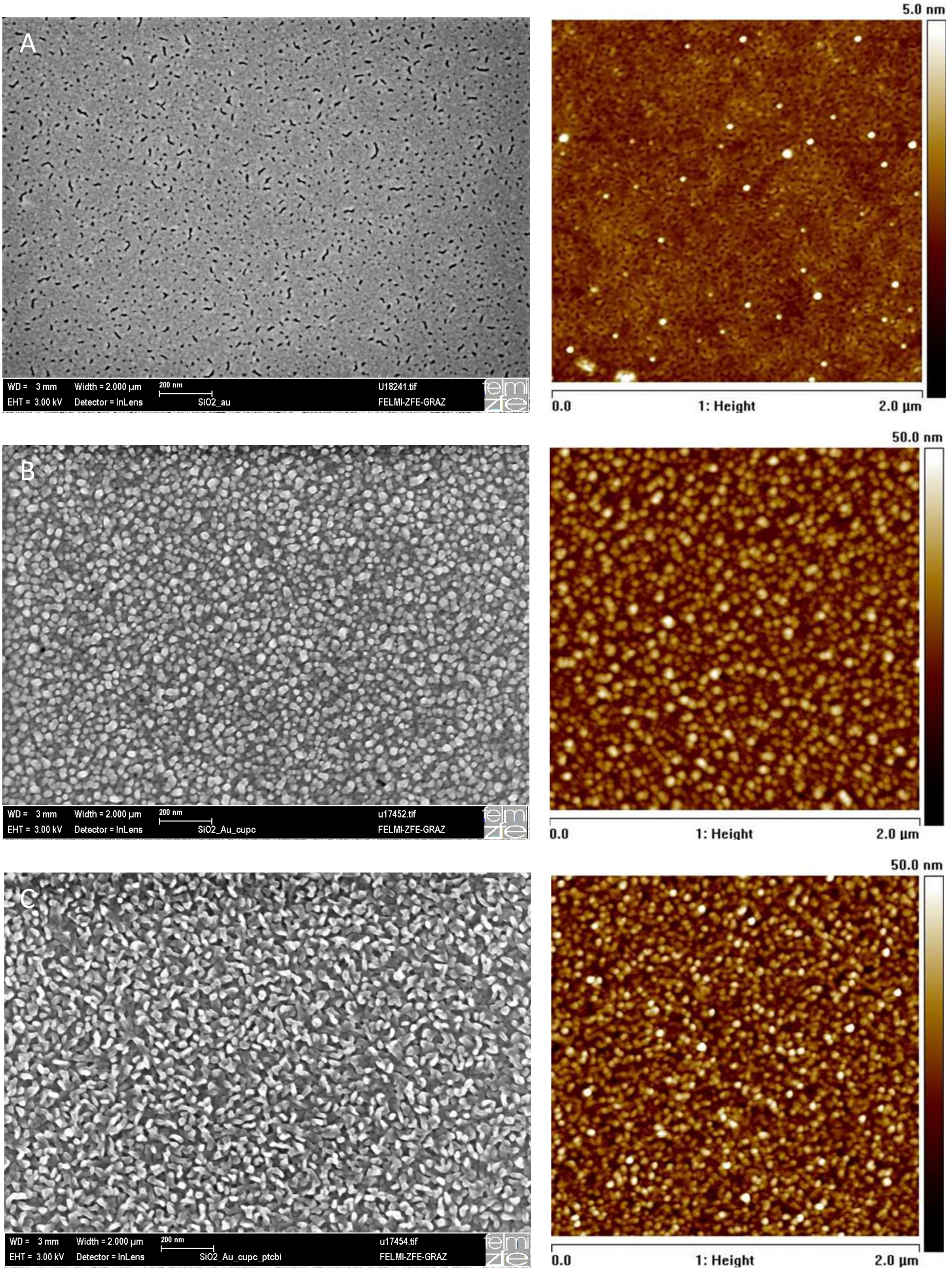
A
WD = 3 mm
Width = 2.000 µm
200 nm
U18241.tif
EHT = 3.00 kV
Detector = InLens
SiO2_au
FELMI-ZFE-GRAZ
5.0 nm
0.0
1: Height
2.0 µm
B
WD = 3 mm
Width = 2.000 µm
200 nm
u17452.tif
EHT = 3.00 kV
Detector = InLens
SiO2_Au_cupc
FELMI-ZFE-GRAZ
50.0 nm
0.0
1: Height
2.0 µm
C
WD = 3 mm
Width = 2.000 µm
200 nm
u17454.tif
EHT = 3.00 kV
Detector = InLens
SiO2_Au_cupc_ptcbi
FELMI-ZFE-GRAZ
50.0 nm
0.0
1: Height
2.0 µm

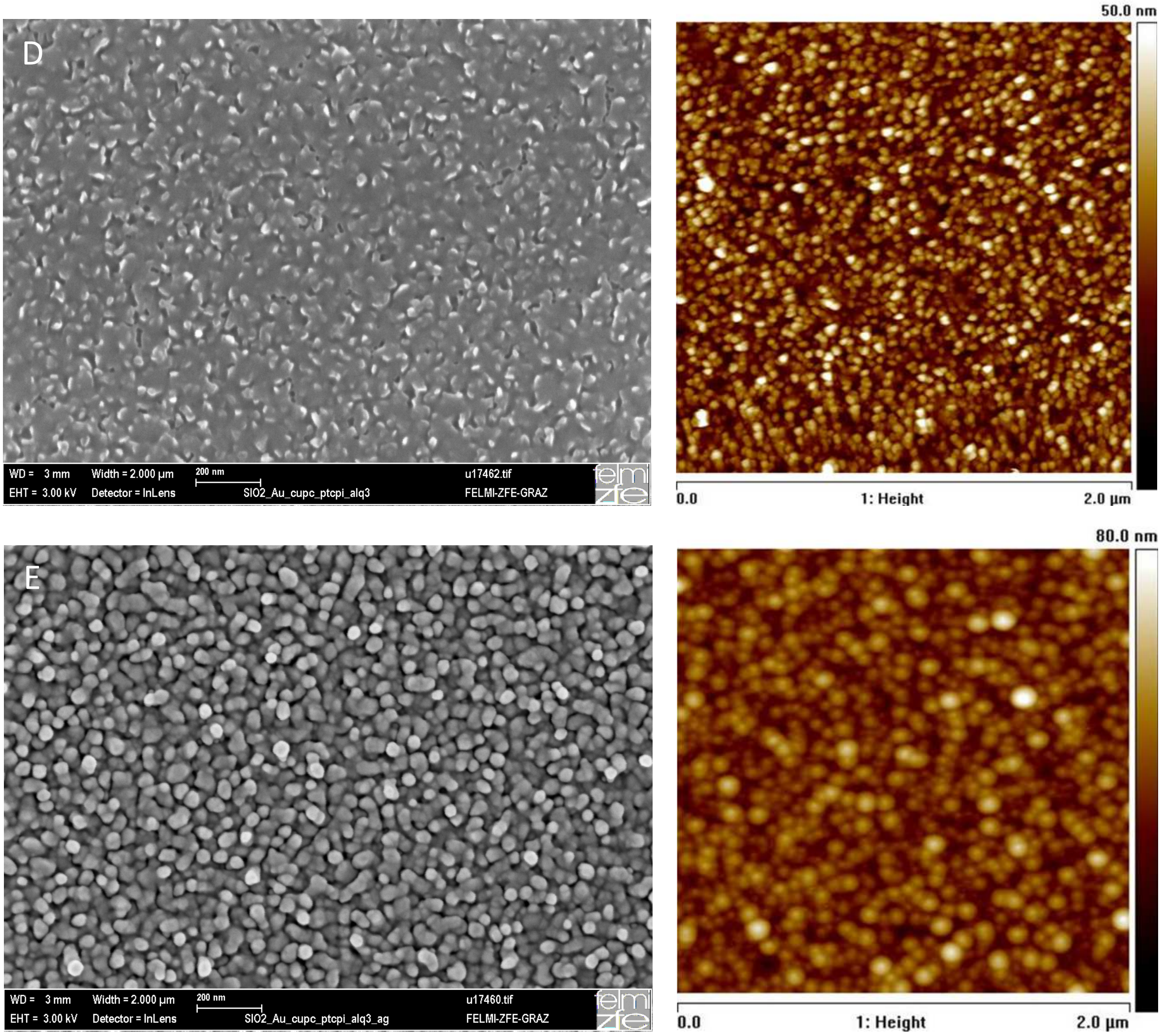

Figure 3.14: SEM and AFM images of the surfaces of stacked systems of a SiO_2 substrate and A) a Au layer B) and a CuPc layer C) and a PTCBi layer D) and a Alq_3 layer E) and a Ag layer. (Neuhold et al., 2011)

Table 3.1: Roughness and thickness values obtained from AFM and XRR measurements for the different stacked layer systems of an OPD.

Sample	AFM Roughness [nm]	XRR Roughness [nm]	XRR Thickness [nm]
SiO_2_Au	0.3	0.5	6.2
SiO_2_Au_CuPc	6.1	5.5	30.9
SiO_2_Au_CuPc_PTCBi	7.4	6.4	36.0
SiO_2_Au_CuPc_PTCBi_Alq_3	6.9	5.8	19.7
SiO_2_Au_CuPc_PTCBi_Alq_3_Ag	8.0	6.8	53.5

For the characterization of the OPD in the TEM cross-section lamellas were prepared in the FIB. As this investigation was performed at the beginning of the work, the preparation was made using conventional milling as described in chapter 3.2.2. The TEM investigations were performed using the Tecnai F20 which is described in chapter 2.3. A TEM BF ZL filtered image and a STEM HAADF image of the same area of the cross-section of an OPD is shown in Figure

3.15 with indicated layer materials. The Au and the Ag layers are clearly identifiable with these imaging techniques. Due to the similarity of the three organic layers regarding the mass-thickness and the atomic numbers, they show low contrast and can therefore not be separated by imaging techniques. For the distinction of the organic materials analytical methods like EDXS, EELS and EFTEM are necessary. The analytical results are presented in the following chapter.

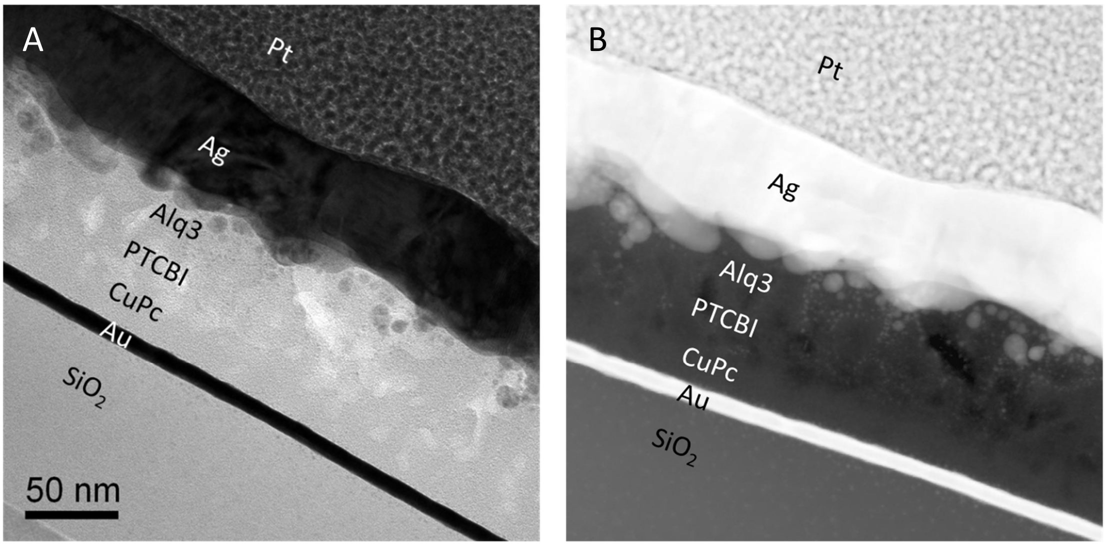

Figure 3.15: A) TEM BF ZL filtered image and B) STEM HAADF image of the same area of the cross-section of an OPD.

The thicknesses of the metallic and organic layers were measured as depicted in Figure 3.16. Depending on the exact analysis position of the OPD the thickness values of the individual layers vary. The thicknesses determined by XRR are listed in Table 3.1. XRR is an integral method averaging over the analyzed region which is in our case 4 cm² in contrast to TEM with its high spatial resolution. Comparing the thickness values of TEM and XRR investigations shows that the results are in good agreement.

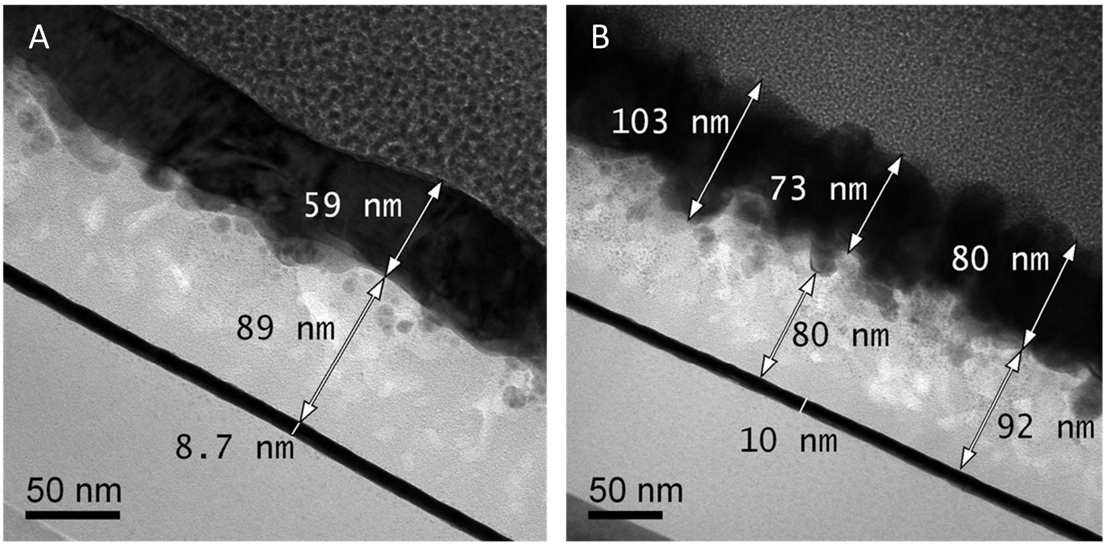

Figure 3.16: BF ZL filtered images of two areas of the cross-section of an OPD with indicated layer thicknesses.

3.4.2 Distinction of organic materials in TEM

As the organic layers of the OPD exhibit similar mass-thicknesses for the cross-section lamellas they are not distinguishable with imaging techniques in TEM, which can be seen in Figure 3.15. Thus this chapter is addressed to the distinction of organic materials using analytical methods like EDXS, EELS and EFTEM.

Since organic devices comprise elements of low and high atomic number due to active materials and metal electrodes, EDXS is advantageous because all elements can be detected simultaneously. Additionally, EELS and EFTEM investigations were performed using their light element sensitivity to separate organic materials at high spatial resolution. The combination of these analytical methods allows identification of all materials with best possible sensitivity and resolution.

The following two chapters discuss the distinction of the different layers of two types of OPDs, using either Alq_3 or Bphen as blocking layer material.

3.4.2.1 OPDs using Alq_3 as blocking layer material

In this chapter an OPD using Alq_3 as a blocking layer material as depicted in Figure 3.2A is the object of investigation. The chemical structures of the organic molecules CuPc ($C_{32}H_{16}N_8Cu$), PTCBi ($C_{36}H_{16}N_4O_2$) and Alq_3 ($C_{27}H_{18}N_3O_3Al$) are displayed in Figure 3.3. Their chemical compositions and concentration ratios of distinct elements are listed in Table 3.2 in at%. As these three materials are organic materials they contain C, H, N and O in different concentrations. Additionally CuPc and Alq_3 exhibit characteristic elements not contained in the other materials, Cu and Al respectively. These two characteristic elements enable the distinction of the materials in the stack of the OPD using EDXS.

Table 3.2: Chemical composition and concentration ratios of the organic materials CuPc, PTCBi and Alq_3 in at%.

	CuPc	PTCBi	Alq_3
H	28.1	27.6	34.6
C	56.1	62.1	51.9
N	14.0	6.9	5.8
O		3.4	5.8
Al			1.9
Cu	1.8		
N/C	0.25	0.11	0.11
O/C		0.06	0.11

Figure 3.17 shows the result of an EDXS line scan along the cross-section of the OPD acquired at the Tecnai F20. For the investigation the specimen holder was tilted 15° towards the EDXS detector as this condition yields the best detector solid angle, which is explained in detail in chapter 2.4.2. Figure 3.17A displays a STEM HAADF image of the OPD with an indicated EDXS line scan. Figure 3.17C-F show EDX spectra of the layers containing

characteristic elements, which are the Au, Ag, CuPc and Alq_3 layers. The Pt peak in the EDX spectrum of Alq_3 derives from a preparation induced Pt particle as this lamella was one of the first which was still prepared by conventional milling (see chapter 3.2.2). The difference of the X-ray production of the metals and the organic materials is clearly visible when comparing the counting statistics of the EDX spectra, which were acquired under equal conditions. Furthermore the characteristic elements are detected in the different materials with different intensities. The Au and Ag peaks in Figure 3.17C and D are dominant features whereas the Cu and Al peaks in Figure 3.17E and F are small signals. Nevertheless the distinction of the organic materials based on the Cu and the Al signal was successful. Figure 3.17B displays the EDXS signals of the line scan of Si, Ag, Au, Cu and Al, aligned vertically to clearly identify the individual layers. The Si, Ag and Au signals clearly indicate the SiO_2, Au and Ag layers. The organic materials were assigned based on the Cu and Al signals. Thus all layers of the OPD could be identified as indicated in Figure 3.17B and their thicknesses are indicated in Figure 3.17A corresponding nicely to the XRR measurements (see Table 3.1).

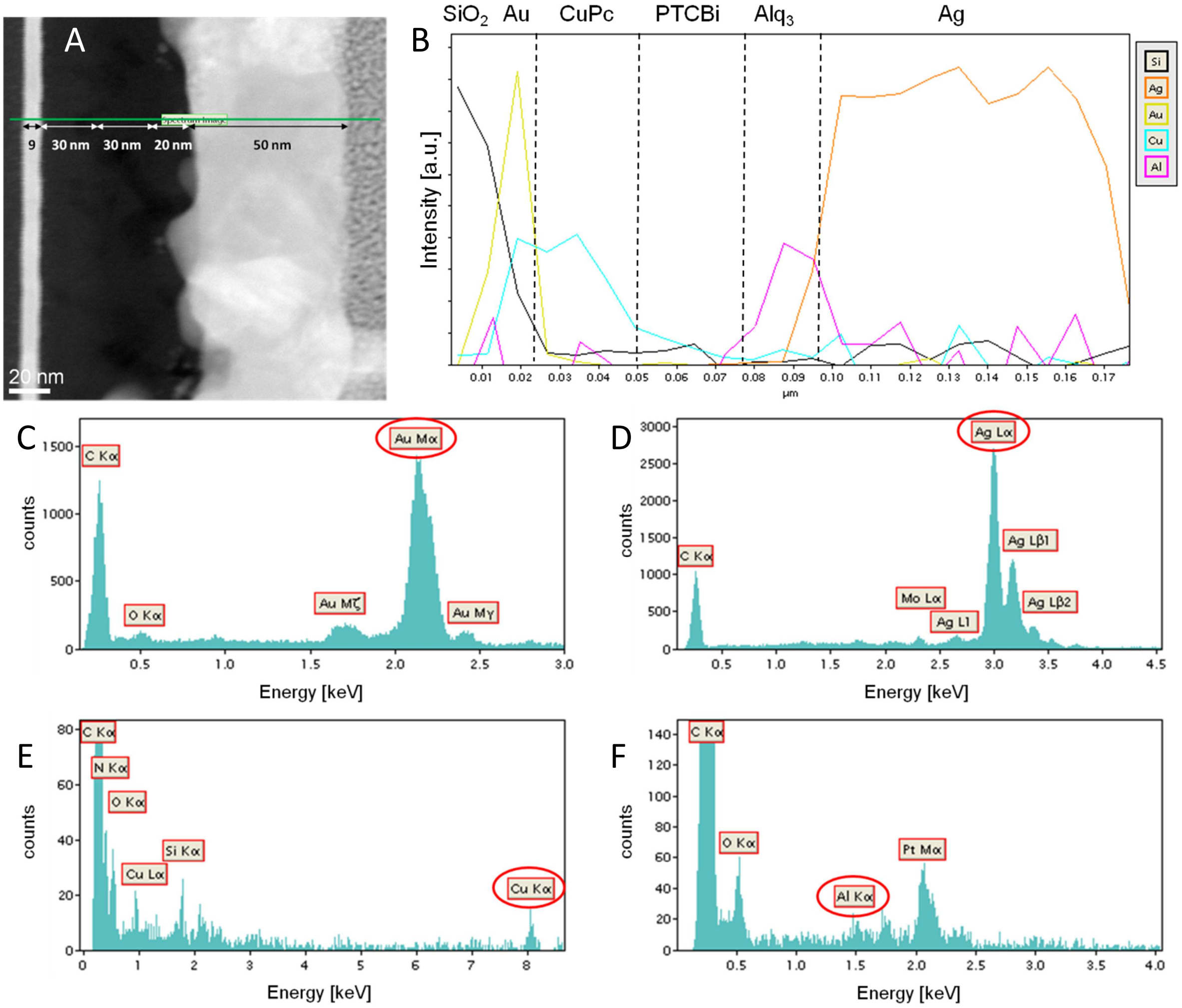

Figure 3.17: A) STEM HAADF image of the cross-section of an OPD using Alq_3 as blocking layer material and indicated EDXS line scan. B) EDXS signals of the line scan of Si, Ag, Au, Cu and Al. EDX spectra of C) Au layer, D) Ag layer, E) CuPc layer and F) Alq_3 layer.

In addition to EDXS measurements EELS measurements were performed. The characteristic elements of the organic materials (Cu and Al) exhibit unfavorable energies for EELS, as the Cu M and Al L edges at 74 eV and 73 eV respectively are at similar energy positions and additionally are swamped by the plasmon signal. The Cu L and Al K edges at 931 eV and 1560 eV respectively exhibit too small signals for the chosen acquisition parameters. Thus the distinction of the organic materials was performed using the elements C, N and O exhibiting their K edges at 284 eV, 401 eV and 532 eV respectively. Figure 3.18 shows the results of an EELS line scan along the cross-section of an OPD using Alq_3 as blocking layer material. The STEM HAADF image with an indicated EELS line scan is shown in Figure 3.18A. In Figure 3.18C three EEL spectra of the line scan according to the three organic materials CuPc, PTCBi and Alq_3 are displayed showing the C, N and O edges with their different intensities. Figure 3.18B depicts the edge intensities (background subtracted) of C, N and O of the EEL spectra of the line scan aligned vertically to clearly identify the individual layers. The organic materials were identified by their different contents of C, N and O as well as by their concentration ratios which are listed in Table 3.2. CuPc exhibits the highest N content of the three organic materials, which is clearly demonstrated in the EELS data. The subsequent PTCBi layer exhibits the highest C content, a small O content and the N content is reduced by half. Consequently the N/C ratio is reduced and the O/C ratio is increased when going from CuPc to PTCBi. This progression is revealed by the EELS data displayed in Figure 3.18B. In comparison Alq_3 exhibits the lowest C content, the highest O content with only 5.8 at% and a slightly reduced N content. The N/C ratio stays the same whereas the O/C ratio is increased. The EELS data demonstrate the different compositions and ratios. The nominal changes (Table 3.2) of the C, N and O contents of CuPc, PTCBi and Alq_3 are in good agreement with the results of the EELS line scan and thus the organic materials could be distinguished as indicated in Figure 3.18B and their thicknesses are indicated in Figure 3.18A. The interface of CuPc to Au is demonstrated by the decrease of the signals of C, N and O. Similarly the C, N and O contents decrease at the interface between Alq_3 and Ag. The pretended increase of N is attributed to the Ag signal as the Ag M edge at 367 eV overlaps with the N edge at 401 eV.

The different layers of the OPD could be identified and distinguished with EDXS and EELS measurements. The interfaces of the different layers were studied in chapter 3.4.1 resulting in the knowledge of rough interfaces between the organic materials. Analyses of the AFM measurements showed that the RMS roughness values of 6 - 7 nm result from height variations of up to 30 nm. Thus in the analytical data the changes from one organic material to the other are not abrupt but slight variations take place as shown in Figure 3.17B and Figure 3.18B. As a consequence thereof and the thickness variation of the Ag layer, which can be seen in Figure 3.17A and Figure 3.18A, the indicated thickness values are average values for the OPD.

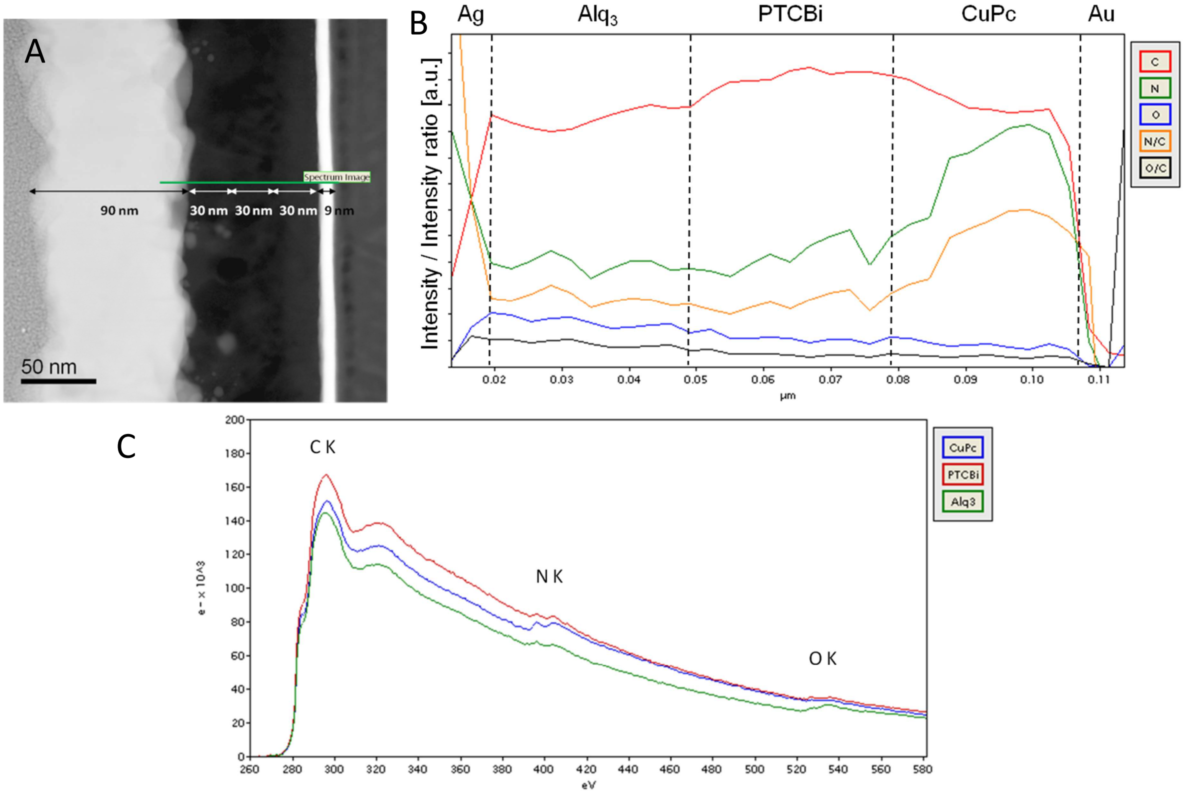

Figure 3.18: A) STEM HAADF image of the cross-section of an OPD using Alq_3 as blocking layer material and indicated EELS line scan. B) EELS signals of the line scan of C, N and O and their ratios. C) EEL spectra of the CuPc, PTCBi and Alq_3 layers.

In this work only results of line scans and no 2-dimensional spectrum images are presented as the damage of the organic material increases with each line and thus the reliability of the data decreases. Figure 3.19 demonstrates this behavior showing a STEM HAADF image of the cross-section of an OPD after acquisition of an EELS spectrum image of eight lines. The first line does not show any damage visible in the STEM HAADF image whereas with increasing line number the damage gets more and more severe resulting in mass losses and even holes in the organic material. Thus reliable results could only be obtained from line scans acquired with low dose rates.

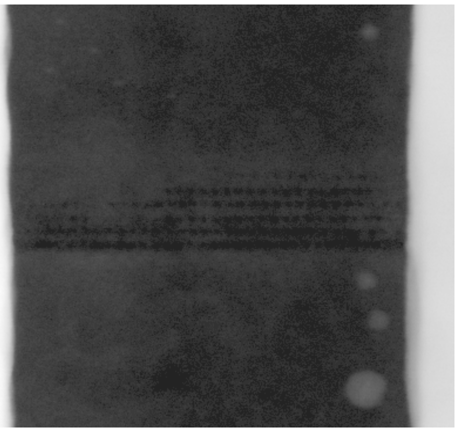

Figure 3.19: STEM HAADF image of the cross-section of an OPD after acquisition of a spectrum image. The caused damage of the organic materials is clearly visible.

3.4.2.2 OPDs using Bphen as blocking layer material

This chapter discusses the characterization of an OPD using Bphen as a blocking layer material. During the period of my work the blocking layer material of the OPDs was changed from Alq_3 to Bphen as OPDs using latter blocking layer exhibited better device performances.

For the distinction of the organic material stack a sample was prepared using Al as top contact material as Al does not alter in such a way as Ag does, which is described in chapter 3.3.3 and eliminates the possibility to investigate the specimen again at a later date. Thus the investigated OPD is represented by the schematic diagram displayed in Figure 3.20. The chemical structures of the organic molecules CuPc ($C_{32}H_{16}N_8Cu$), PTCBi ($C_{36}H_{16}N_4O_2$) and Bphen ($C_{24}H_{16}N_2$) are displayed in Figure 3.3 and their chemical compositions and concentration ratios of distinct elements are listed in Table 3.3 in at%.

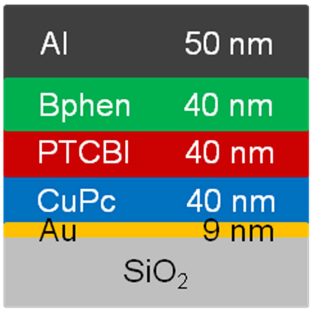

Figure 3.20: Schematic diagram of the OPD using Bphen as blocking layer material.

Table 3.3: Chemical composition and concentration ratios of the organic materials CuPc, PTCBi and Bphen in at%.

	CuPc	PTCBi	Bphen
H	28.1	27.6	38.1
C	56.1	62.1	57.1
N	14.0	6.9	4.8
O		3.4	
Cu	1.8		
N/C	0.25	0.11	0.08
O/C		0.06	

TEM BF ZL filtered images of the cross-section of such an OPD are displayed in Figure 3.21 with the indicated different materials. The interface between Bphen and Al is noticeable as an additional layer seems to be present. Analytical investigations confirmed this finding and the additional layer was identified as an AlO_x layer. To display the AlO_x layer EFTEM measurements were performed and elemental maps were determined using the three-window method (Bonnet et al., 1988). The elemental maps of Al and O of the specimen area shown in Figure 3.21B are depicted in Figure 3.22 together with a composite color overlay of both elements visualizing the AlO_x layer in purple.

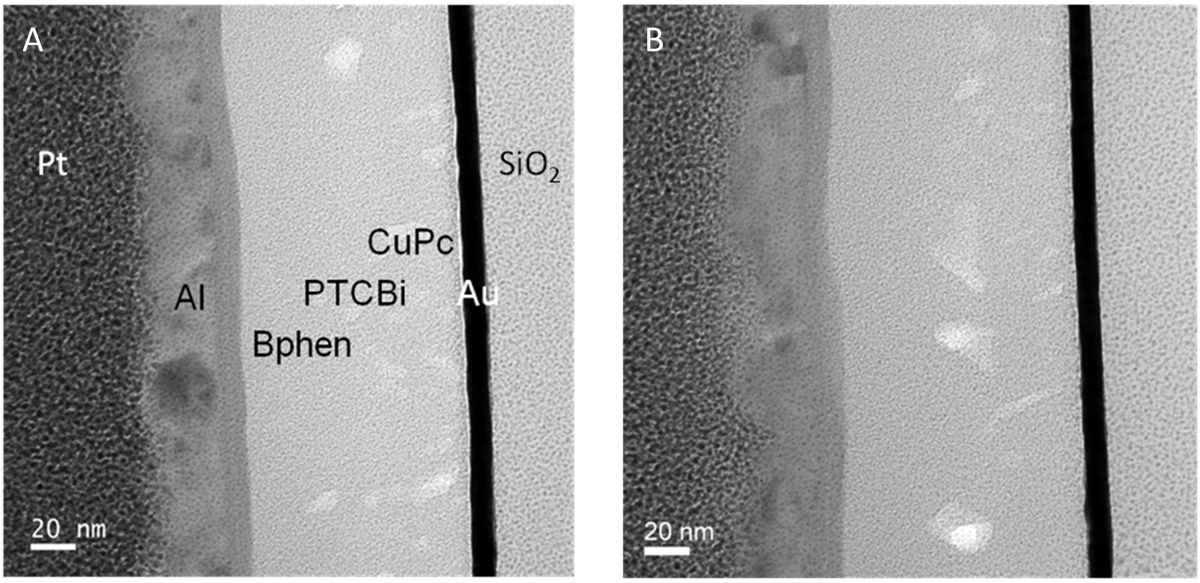

Figure 3.21: TEM BF ZL filtered images of an OPD using Bphen as blocking layer and Al as top contact.

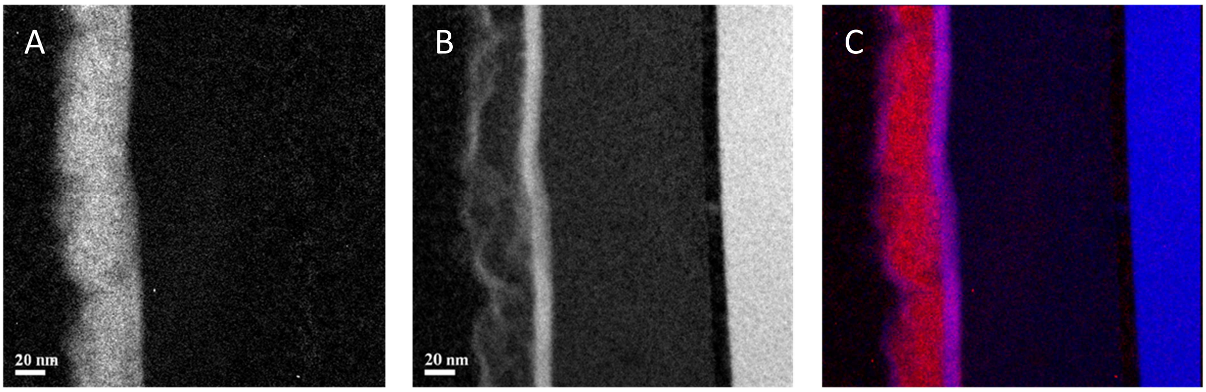

Figure 3.22: Elemental maps of A) Al and B) O and C) a composite color overlay of Al (red) and O (blue).

The combination of the organic materials CuPc, PTCBi and Bphen only shows one characteristic element for the analytical investigation not contained in the other materials, which is Cu in CuPc (see Table 3.3). Additionally PTCBi is the only material exhibiting O. But O is present only in a very low concentration giving a very weak analytical signal. Thus the combination of analytical techniques as EDXS, EELS and EFTEM is necessary to identify and distinguish the different materials in the OPD using Bphen as blocking layer material. As the materials of this OPD exhibit the same elements as OPDs using Alq$_3$ as a blocking layer the EELS investigations concentrated again on the elements C, N and O due to the same reasons as explained in chapter 3.4.2.1. The analyses of EDXS investigations were performed using the signals of all detectable elements being Cu, Al, Au, C, N and O.

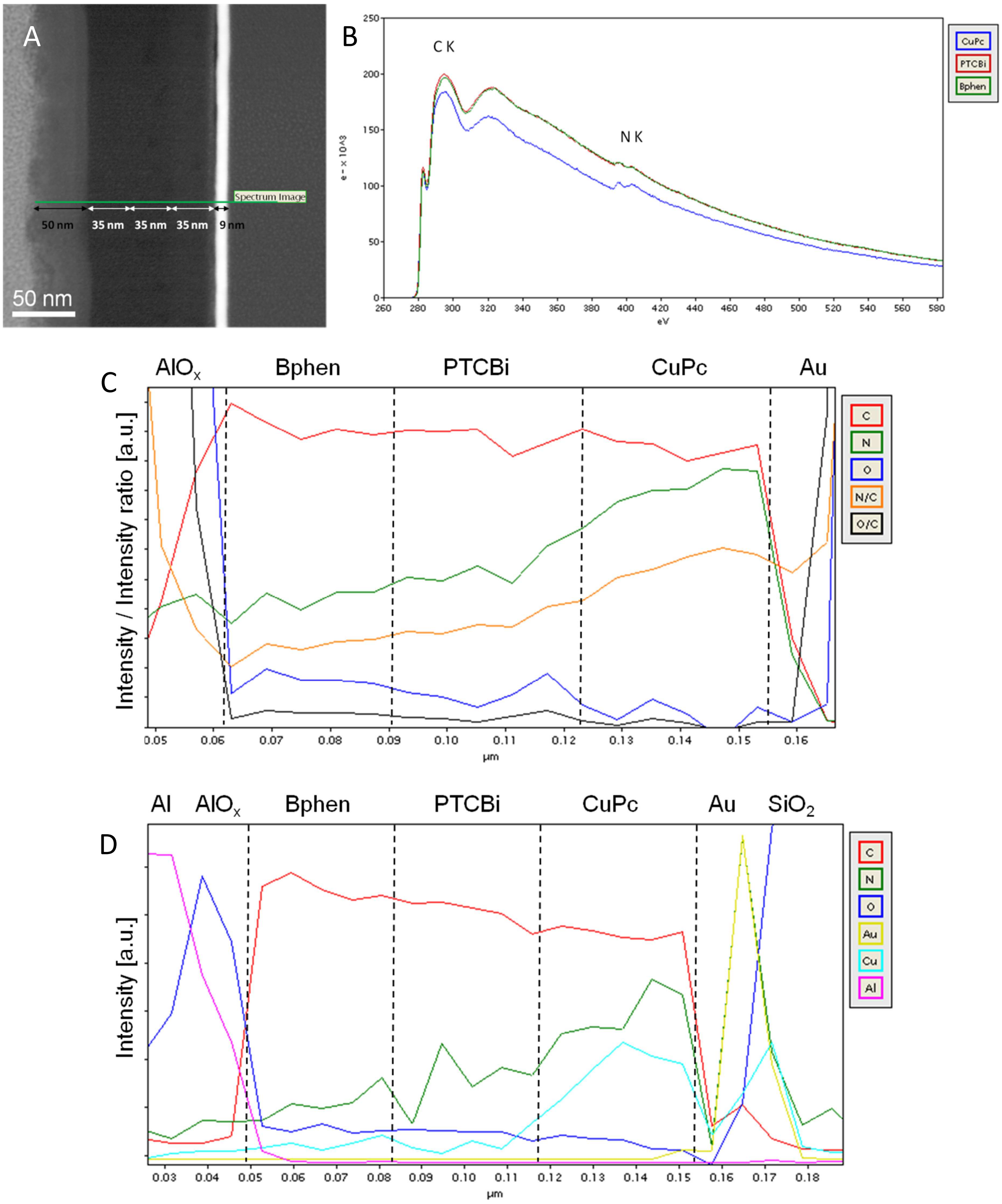

Figure 3.23: A) STEM HAADF image of the cross-section of an OPD using Bphen as blocking layer and indicated line scan. B) EEL spectra of CuPc, PTCBi and Bphen layers. Line scan results for C) EELS signals of C, N and O and their ratios and D) EDXS signals of C, N, O, Au, Cu and Al.

The first analytical results were acquired at the Tecnai F20 and are presented in Figure 3.23 as two line scans with optimized acquisition parameters for both EDXS and EELS. Figure 3.23A displays a STEM HAADF image of the cross-section of an OPD using Bphen as blocking layer and the indicated EELS line scan. In Figure 3.23B three EEL spectra of the line scan according to the three organic materials CuPc, PTCBi and Bphen are displayed showing the C, N and O edges with their different intensities. The edge intensities (background subtracted) of C, N and O of the EEL spectra are displayed in Figure 3.23C. Figure 3.23D shows the EDXS intensities of C, N, O, Au, Cu and Al of another line scan. The Au and Al layers are clearly identified in the EDXS data. The AlO_x layer is derived from the immense increase of the O signal in both EDXS and EELS. The distinction of CuPc and PTCBi is similar to the description in chapter 3.4.2.1. CuPc is identified by the Cu signal of the EDXS data and the biggest N content of all three organic materials which is detected in EDXS and EELS. The distinction of PTCBi and Bphen is only based on different concentrations of C, N and O as well as their concentration ratios. According to nominal values O is only present in PTCBi with a concentration of only 3.4 at%. In this case the analytical signals of O are too small to distinguish the materials accurately. The C signals of both EDXS and EELS show deviating results from the nominal compositions. According to the nominal composition the C content is smaller for Bphen but the analytical results show an increase of the C signal which is attributed to contamination. Contamination is discussed in chapter 3.3.2 and resulting contamination of an EELS line scan is depicted in Figure 3.10A explaining deviations of the nominal C content. Thus only the N signal can be used for the distinction of PTCBi and Bphen. But the concentration difference of N between PTCBi and Bphen is only 2.1 at%. The N signal and the ratio N/C decrease from the interface of CuPc/PTCBi till the AlO_x layer, but no accurately defined separation of PTCBi and Bphen could be achieved. Nevertheless the layers and their estimated thicknesses are indicated in Figure 3.23A and B.

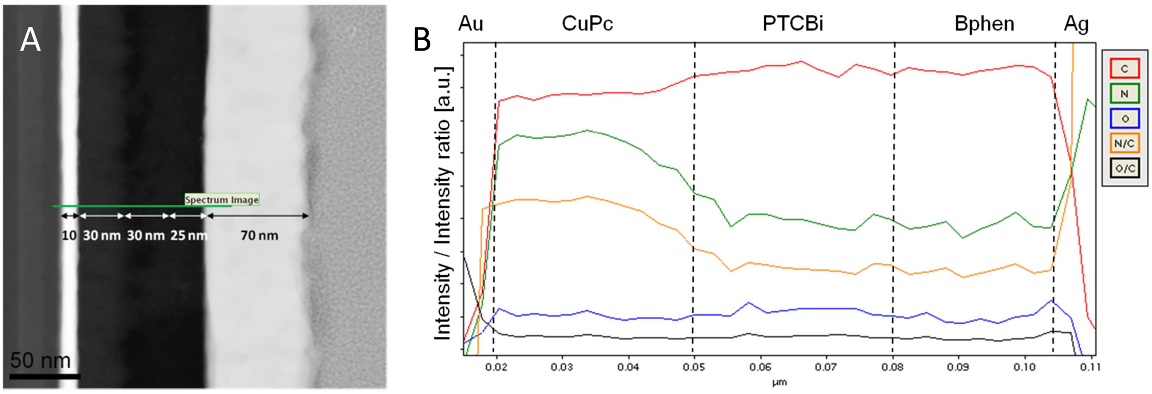

Figure 3.24: A) STEM HAADF image of the cross-section of an OPD using Bphen as blocking layer and indicated EELS line scan. B) EELS signals of the line scan of C, N and O and their ratios.

At a later date analytical investigations were performed on the Titan³ benefiting from its better analytical sensitivity. Figure 3.24 shows the results of an EELS line scan with higher spatial resolution of an OPD using Ag as top contact material. Note that the pretended increase of N at the position of the Ag layer is again attributed to the overlapping Ag signal, which is explained in chapter 3.4.2.1. The CuPc is observable by its highest N and lowest C content in comparison to the other organic materials. In this case PTCBi and Bphen can be distinguished by the O signal. Again the C intensity for Bphen does not decrease to the nominal value, which is again attributed to contamination. The layers and their thicknesses are indicated in Figure 3.24A and B.

EDXS investigations of the OPD using Al as top contact layer were performed with the Super-X detector of the Titan³. The ChemiSTEM technology (see chapter 2.3) permits fast mapping and the acquisition of “hypermaps”. Hypermaps are similar to spectrum images using dwell times in the order of 100 µs resulting in the acquisition of many frames to achieve the whole pixel time. Thus the beam is repeatedly scanned over the region of interest and the EDXS signals are added to the corresponding pixels. The acquisition method using short dwell times and many iterations is gentler to the specimen with respect to beam damage in comparison to the acquisition method where the pixel time is acquired at once (see Figure 3.19) and thus allows for higher spatial resolution when drift correction is performed.

Figure 3.25 shows the results of a hypermap acquired along the cross-section of an OPD using Bphen as blocking layer. Figure 3.25A displays an STEM HAADF image and the indicated region of the hypermap. The hypermap consists of 300 x 64 pixels and was acquired with a dwell time of 250 µs and a total acquisition time of 4002 s. The EDXS signals of the hypermap are shown in Figure 3.25B for Al, Au, Cu, C, N and O in the indicated colors. The Al layer appears in pink, the Au layer in yellow and the AlO_x layer results in violet. The CuPc is a mixture of Cu, C and N resulting in a mixture of turquoise, green and red. The increase of C in the CuPc layer at the bottom right is attributed to contamination. For a more detailed analysis the intensities of the different elements of the hypermap were integrated perpendicular to the indicated yellow line in the hypermap in Figure 3.25B. The results of the summed intensity profiles are displayed in Figure 3.25C and D for the whole lateral extension of the OPD and zoomed to the organic material stack. The different elements are represented by the same colors as in the hypermap. The Au, Al and AlO_x layer are identified clearly. The CuPc is characteristic with the Cu signal and the highest N signal. The N and O signals of the EDXS data show correct relative values and progressions for the organic materials with high spatial resolution. The C signal cannot be used as contamination took place during the acquisition time of 4002 s covering the signal originating from the organic materials. The distinction of PTCBi and Bphen is based on N and O and due to the sensitivity of the Super-X detector the EDXS signals are more accurate. Thus the N signal forms a plateau next to the CuPc/PTCBi interface. This plateau represents the PTCBi layer and the following decrease represents the interface to the Bphen layer. As the interfaces between the organic materials are rough, which is discussed in chapters 3.4.1 and 3.4.2.1, the change in the analytical signals is smooth. This fact can nicely be seen at the interface of CuPc and PTCBi in the smooth change of the Cu and N signals.

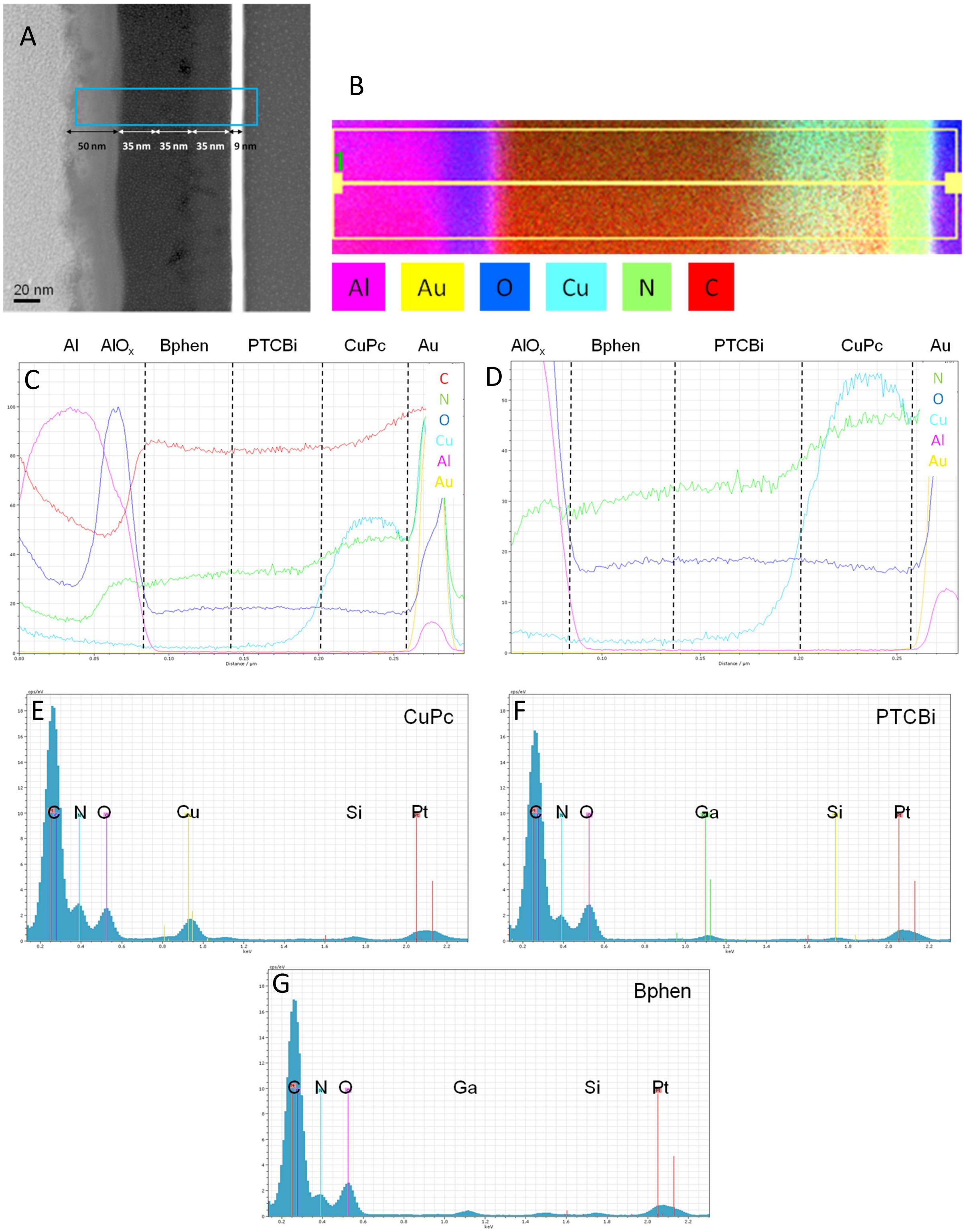

Figure 3.25: A) STEM HAADF image of the cross-section of an OPD using Bphen as blocking layer and indicated region of the hypermap. B) EDXS signals of Al, Au, Cu, C, N and O of the hypermap. C,D) Intensity profiles of the EDXS signals of the hypermap C) for the whole lateral extension of the OPD and D) zoomed to the organic material stack. E-G) EDX spectra of CuPc, PTCBi and Bphen.

Furthermore EDX spectra of the hypermap corresponding to the organic materials CuPc, PTCBi and Bphen are displayed in Figure 3.25E, F and G respectively. Pt peaks are visible in all three EDX spectra as the Pt injection system of the FIB instrument had a locking problem during the specimen preparation. Due to increased detection efficiency the EDX spectra show good counting statistics enabling accurate analysis.

In addition to EDXS and EELS, EFTEM measurements were performed to distinguish the organic materials, especially PTCBi and Bphen. Based on the EFTEM images elemental maps were determined using the three-window method and the results are shown in Figure 3.26. Figure 3.26A and B display a TEM BF ZL filtered image of the cross-section of an OPD using Bphen as blocking layer and Al as top contact material and its relative thickness map. The elemental maps of exactly the same specimen area are displayed in Figure 3.26C-F for the elements C, N, O and Cu showing their elemental distributions. The K edges of C, N and O and the L edges of Cu were used. For the distinction of the organic materials analyses were performed using the intensity profiles of the elemental maps. Therefore an area of homogeneous thickness of the organic materials was chosen and is indicated in the TEM BF image, the relative thickness map and the elemental maps. The intensities were integrated over 200 pixels perpendicular to the indicated arrow and are displayed in Figure 3.26G. The AlO_x layer can be determined by the huge increase in the O signal, and the Au layer by the decrease of all displayed elements. CuPc is identified by the Cu, the highest N and the lowest C concentration. PTCBi exhibits the highest C concentration and the N content decreases significantly. Bphen can be identified by the decrease of the C and the N signal in comparison to PTCBi (see Table 3.3). Using EFTEM the C signal decreases for Bphen in comparison to PTCBi. This nominal pretended behavior could not be detected using EDXS and EELS due to successive acquisition of the signals yielding different contamination conditions for successive analysis points and thus distorting the C signal of the different organic materials. Using EFTEM the acquisition conditions for all three organic materials are equal and the signal for each pixel is acquired at the same time. As the images for the elemental map of C were acquired at first, contamination could still be neglected and the resulting C signal could be used to distinguish PTCBi and Bphen. As already mentioned above the interfaces between the organic materials appear as smooth changes in analytical signal as the interfaces are rough exhibiting RMS roughnesses of 6 – 7 nm and thus height differences of up to 30 nm (see chapter 3.4.1 and 3.4.2.1). Additionally the layers and their thicknesses are indicated in Figure 3.26A and G.

The different layers of the OPD using Bphen as blocking layer could be identified and distinguished using the combination of analytical techniques like EDXS, EELS and EFTEM and their determined thicknesses are in good agreement.

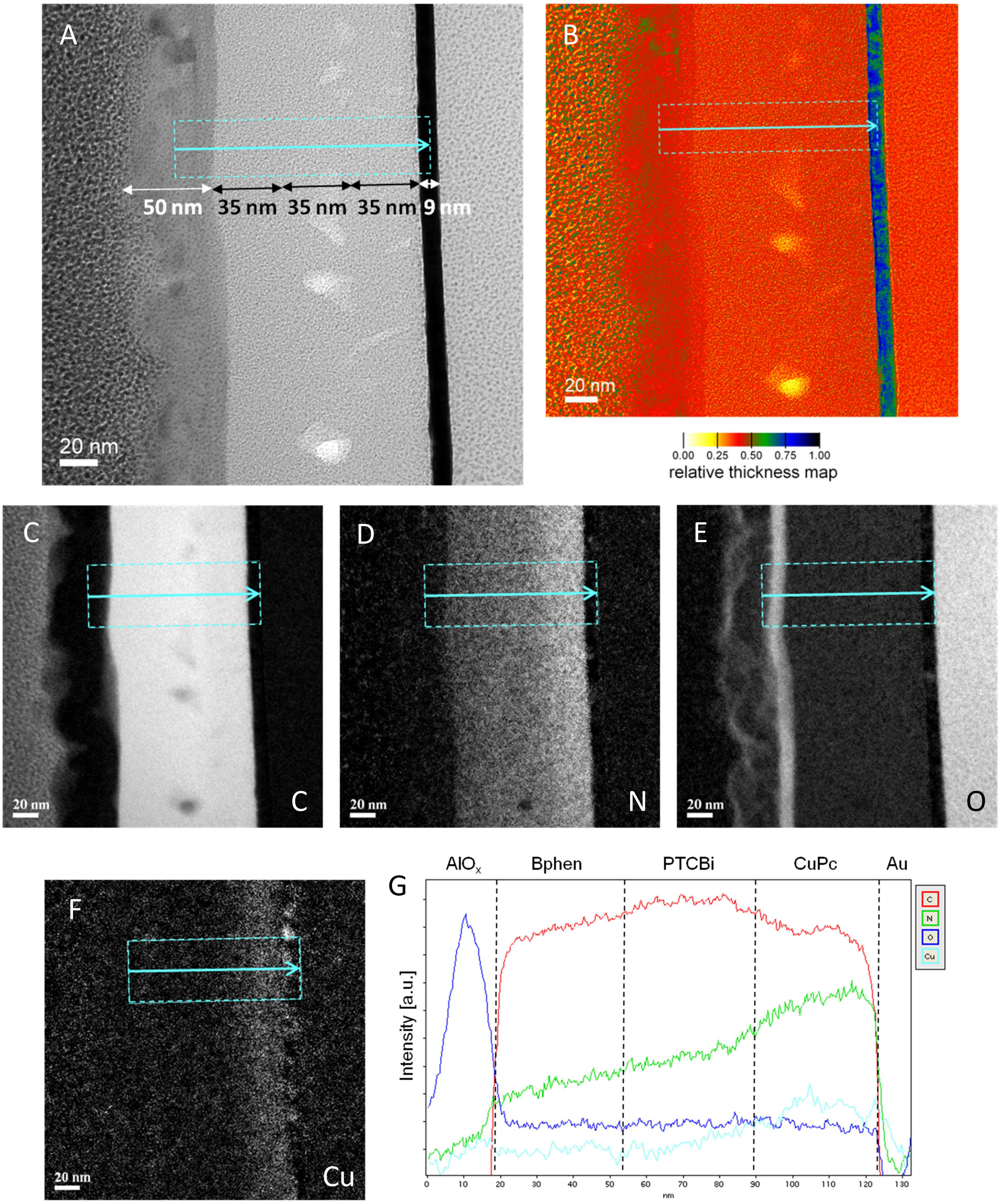

Figure 3.26: A) TEM BF ZL filtered image of the cross-section of an OPD using Bphen as blocking layer and B) its relative thickness map. C-F) Elemental maps of C) C, D) N, E) O and F) Cu. G) Intensity profile of the elemental map signals of C, N, O and Cu of the indicated region.

3.5 Diffusion of Ag into organic semiconducting materials

As organic/metal interfaces play an important role for the device performance, numerous studies on metal diffusion into organic layers have been carried out (Hirose et al., 1996, Faupel et al., 1998, Strunskus et al., 1998, Song et al., 2001a, Song et al., 2001b, Turak et al., 2002, Grandin et al., 2003, Wang et al., 2007, Scharnberg et al., 2005, Dürr et al., 2003, Gautier et al., 1996) within which a variety of experimental techniques have been used including TEM (Faupel et al., 1998, Strunskus et al., 1998, Dürr et al., 2003), X-ray reflectivity (Dürr et al., 2003, Gautier et al., 1996), X-ray photoelectron spectroscopy (Strunskus et al., 1998, Song et al., 2001b, Turak et al., 2002, Wang et al., 2007), secondary ion-mass spectrometry (Song et al., 2001a, Grandin et al., 2003), radiotracer measurements (Faupel et al., 1998, Strunskus et al., 1998, Scharnberg et al., 2005), and Rutherford backscattering (Faupel et al., 1998, Grandin et al., 2003, Dürr et al., 2003). Although some data on Ag diffusion into Alq_3 was already reported (Song et al., 2001a, Song et al., 2001b, Turak et al., 2002, Grandin et al., 2003, Wang et al., 2007), to the best of our knowledge, no study was carried out on Ag diffusion into Bphen yet. The above-mentioned studies report conflicting results on Ag diffusion into Alq_3 including clear evidence that diffusion does occur (Song et al., 2001a, Song et al., 2001b) and the presence of well-defined interfaces without chemical reactions (Turak et al., 2002, Grandin et al., 2003). (Fladischer et al., 2012)

In this work, we investigated Ag diffusion into both Alq_3 and Bphen with respect to different Ag deposition techniques such as electron beam deposition (EBD), ion beam sputtering (IBS), and vacuum thermal evaporation (VTE) at various deposition rates and published the results recently (Fladischer et al., 2012). The interfaces were characterized combining transmission electron microscopy (TEM), favored for its high spatial resolution, and X-ray reflectivity (XRR) as bulk characterization tool. Herewith, the dependence of interfacial parameters such as roughness and material diffusion on the fabrication procedure of the top Ag cathode was investigated. Finally, the findings for the interfaces were related to the device performances.

OPDs were fabricated as outlined in chapter 3.1 with latter mentioned layer thicknesses on microscope glass slides used as substrates. For the application of the Ag electrode four different deposition techniques were used: electron beam deposition (EBD), ion beam sputtering (IBS), and vacuum thermal evaporation (VTE) with deposition rates of 0.02 and 0.3 nm/s. To provide reproducibility for the current to voltage characteristic measurements, we fabricated every OPD configuration differing in the organic material and/or the Ag deposition technique 6 times.

The OPDs were characterized by current to voltage (I-V) measurements to gain insight into the electrical behavior and the performance of the devices. I-V characteristics were determined using a 150 W EKE halogen lamp positioned under a glass window as described in the publication of Fladischer et al. (Fladischer et al., 2012). The samples were placed on the glass window and contacted from the top with contact needles. The I-V characteristic was measured using an MB1020 parameter analyzer from mb-technologies. Additionally, the measurement desk was equipped with an opaque shield to block ambient light during the measurements.

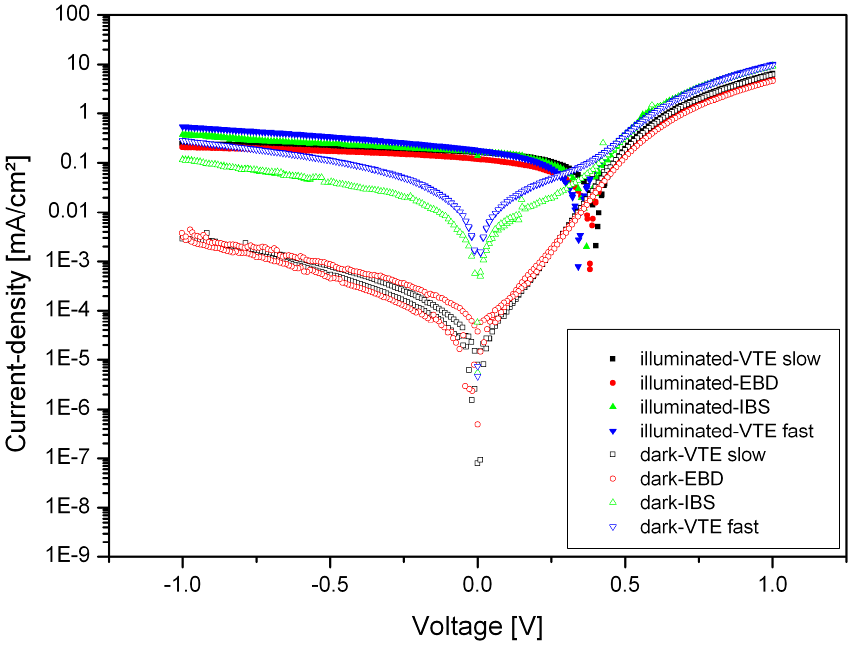

Figure 3.27: Current-density vs voltage characteristics of OPDs using Bphen as blocking layer under illumination (10 mW/cm²) and in dark. The Ag electrodes were produced by vacuum thermal evaporation (VTE), electron beam deposition (EBD) and ion beam sputtering (IBS). (Fladischer et al., 2012)

The investigated OPDs are employed as detection units in opto-chemical sensor applications. Such integrated sensor OPDs are used to quantify changes of light corresponding to different kinds of gas concentrations as described in the publication of Lamprecht et al. (Lamprecht et al., 2011). Note that a high ON/OFF ratio (ON: photodiode current under illumination, OFF: dark current) of the corresponding OPDs is essential to reach a high resolution of the sensor. ON/OFF ratios (measured at 0 V) of more than 1×10^3 are necessary for reliable sensor performance.

The I-V characteristics of the investigated OPDs showed (i), that the two organic blocking layer materials lead to different device performances and, (ii), that the different Ag deposition techniques significantly impact the I-V characteristics. Figure 3.27 depicts representative I-V characteristics in dark and under white light illumination for the OPDs using Bphen as blocking layer.

OPDs with Ag deposited slowly by VTE (Figure 3.27, black lines) reached the highest ON/OFF ratios of 1×10^5, followed by EBD (red lines) yielding an ON/OFF ratio of 1×10^4, whereas devices fabricated by IBS (green lines) and fast VTE (blue lines) reached only 1×10^2. (Fladischer et al., 2012)

For TEM investigations all samples were prepared in the FIB instrument using upside down milling to avoid artificial ion beam induced Ag diffusion into the organic material (see chapter 3.2.2). To prevent Ag from degradation in ambient air (see chapter 3.3.3), we started TEM investigations immediately after preparing the lamella. All TEM investigations concerning the Ag diffusion were performed at the Tecnai F20 (see chapter 2.3). To elucidate the interfaces, we chose TEM bright-field (BF) and high-angle annular dark field (HAADF) imaging techniques. Figure 3.28 shows TEM BF ZL filtered images and STEM HAADF images of cross-sections of OPDs using (A,B) Alq_3 and (C,D) Bphen as blocking layer materials and Ag electrodes deposited by VTE, which were characterized previously by I-V measurements. The interfaces between Alq_3/Ag and Bphen/Ag appear different in the images. In the case of Alq_3 the organic/metal interface is very rough and Ag diffusion takes place whereas in the case of Bphen a well-defined interface without Ag diffusion is visible.

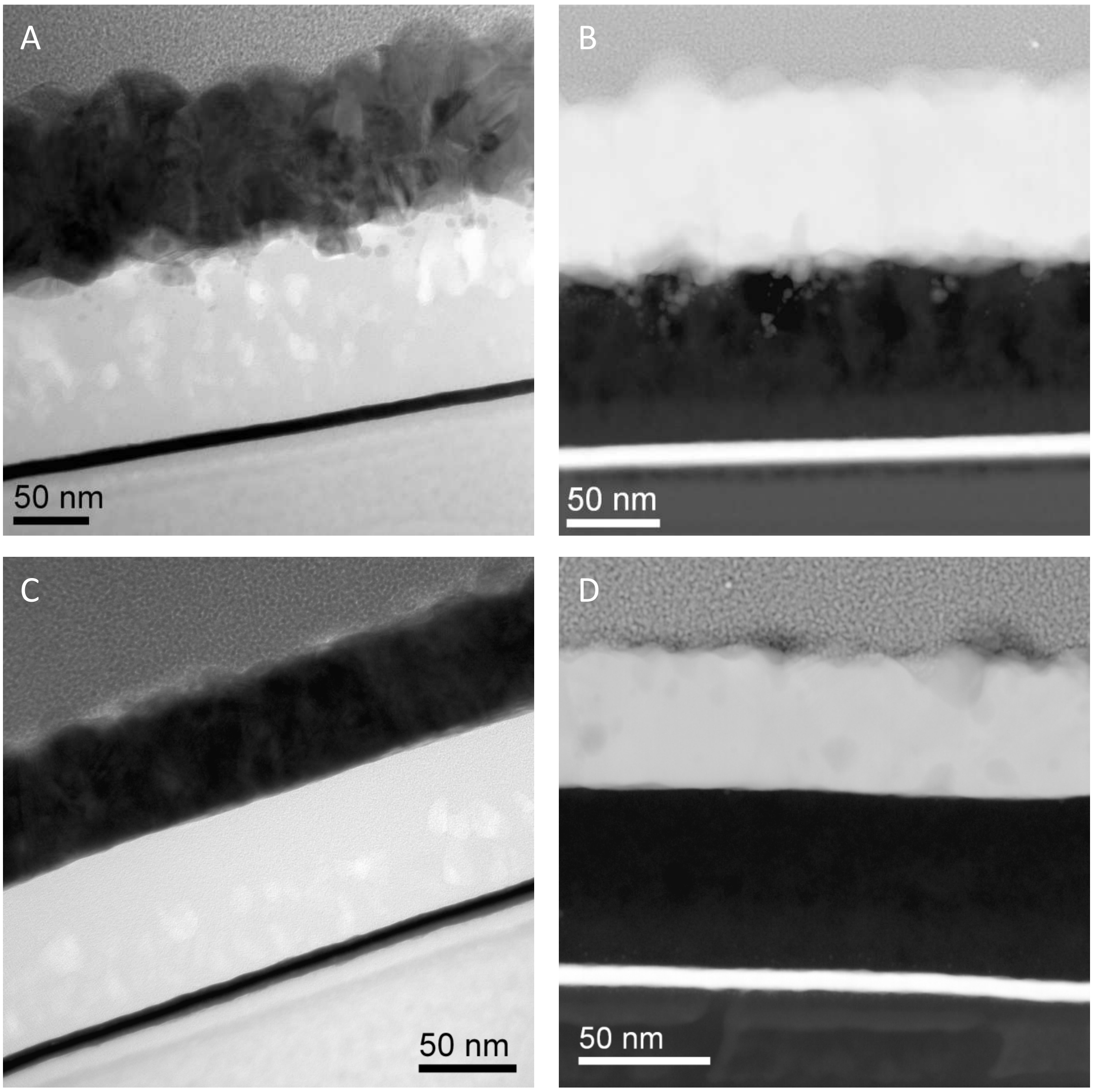

Figure 3.28: A,C) TEM BF ZL filtered images and B,D) STEM HAADF images of cross-sections of OPDs using A,B) Alq_3 and C,D) Bphen as blocking layer materials and Ag electrodes deposited by vacuum thermal evaporation.

3.5.1 The Ag layer

For the study of the Ag diffusion into organic materials additional test structures were fabricated comprising Alq_3 and Bphen layers with top Ag layers only. To enable accurate XRR measurements the Ag layer needs to be as thin as possible. Therefore the minimum Ag layer thickness creating a continuous layer was determined by fabricating Ag layers with different thicknesses and measuring their sheet resistance using the four-point probe method. Thus Ag layers with thicknesses of 5 nm, 10 nm, 15 nm, 20 nm and 25 nm were deposited on 40 nm Alq_3 by VTE. Additionally SEM measurements were performed to elucidate the morphology of these samples. The SEM results are displayed in Figure 3.29. Figure 3.29A shows a Ag film thickness of 5 nm and only small Ag islands are visible. In Figure 3.29B, representing a Ag film thickness of 15 nm, the islands are larger and start growing together. The black gaps in the Ag layer display the subjacent organic material. A Ag film thickness of 25 nm is displayed in Figure 3.29C. Gaps are still visible but their number is reduced. The growth process of Ag starts by forming small islands, which increase in size and grow together with increasing layer thickness.

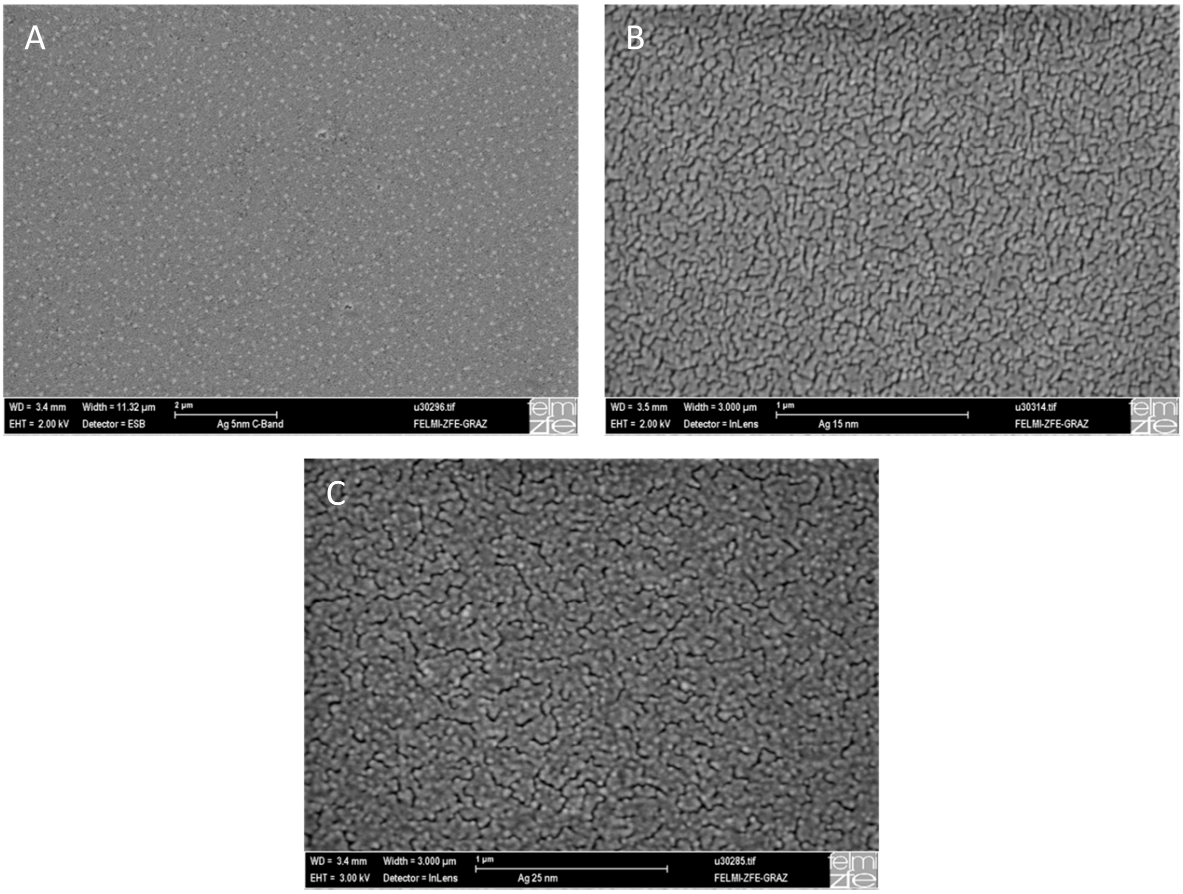

Figure 3.29: SEM images of Ag layers of A) 5 nm, B) 15 nm and C) 25 nm thickness on Alq_3.

This growth process can also be shown by sheet resistance measurements displayed in Figure 3.30. The more the Ag islands are grown together the smaller is the sheet resistance. In our case the sheet resistance of 20 nm Ag is significantly reduced in comparison to 15 nm Ag. Thus we assume that a continuous layer is formed at a minimum film thickness of about 20 nm Ag.

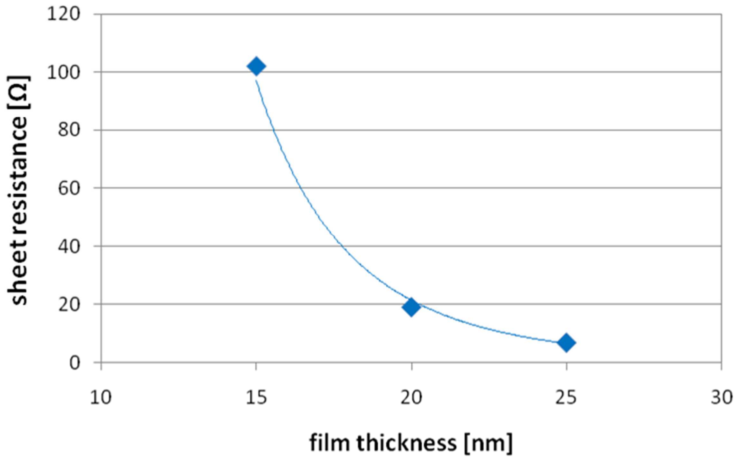

Figure 3.30: Sheet resistance as a function of film thickness of Ag.

For TEM investigations a Ag layer of 25 nm thickness was prepared as a plan view specimen. Therefore Ag was deposited by VTE on PEDOT:PSS printed on a glass slide. To float off the Ag layer, the sample was put into a vessel with distilled water, where PEDOT:PSS dissolved, and the Ag layer was transferred to a TEM supporting grid. Figure 3.31 shows optical microscope images of the Ag plan view specimen of a thickness of only 25 nm.

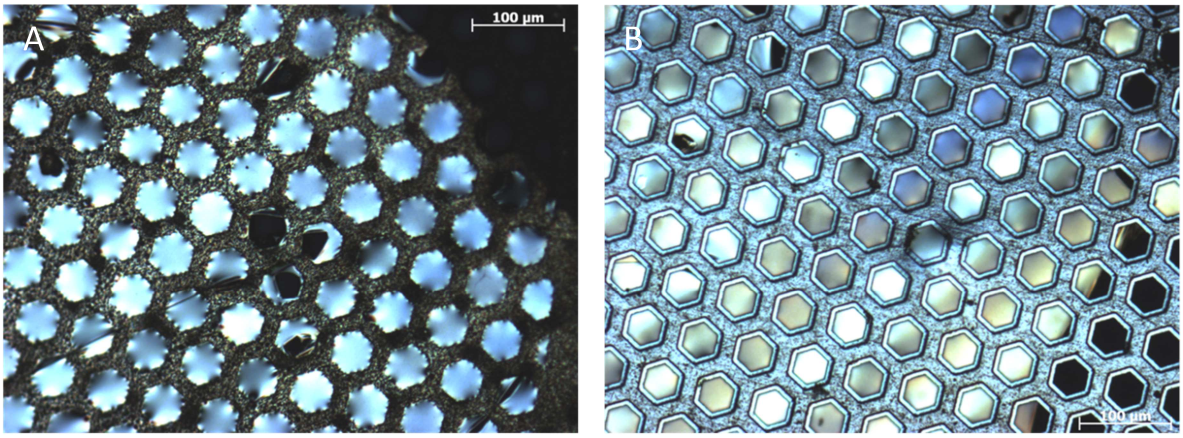

Figure 3.31: Optical microscope images of the plan view specimen of Ag with a thickness of 25 nm on a supporting grid in A) top view and B) bottom view.

This plan view Ag specimen was investigated by TEM. TEM BF ZL filtered images of different magnifications are shown in Figure 3.32. The white gaps correspond to the gaps observed in the SEM images in Figure 3.29. The Ag grains exhibit different sizes, small grains with diameters of only 15 nm are detected next to grains with diameters of 30 – 50 nm, which form the majority. Additionally some grains with diameters of 120 nm are detected as well (see Figure 3.32).

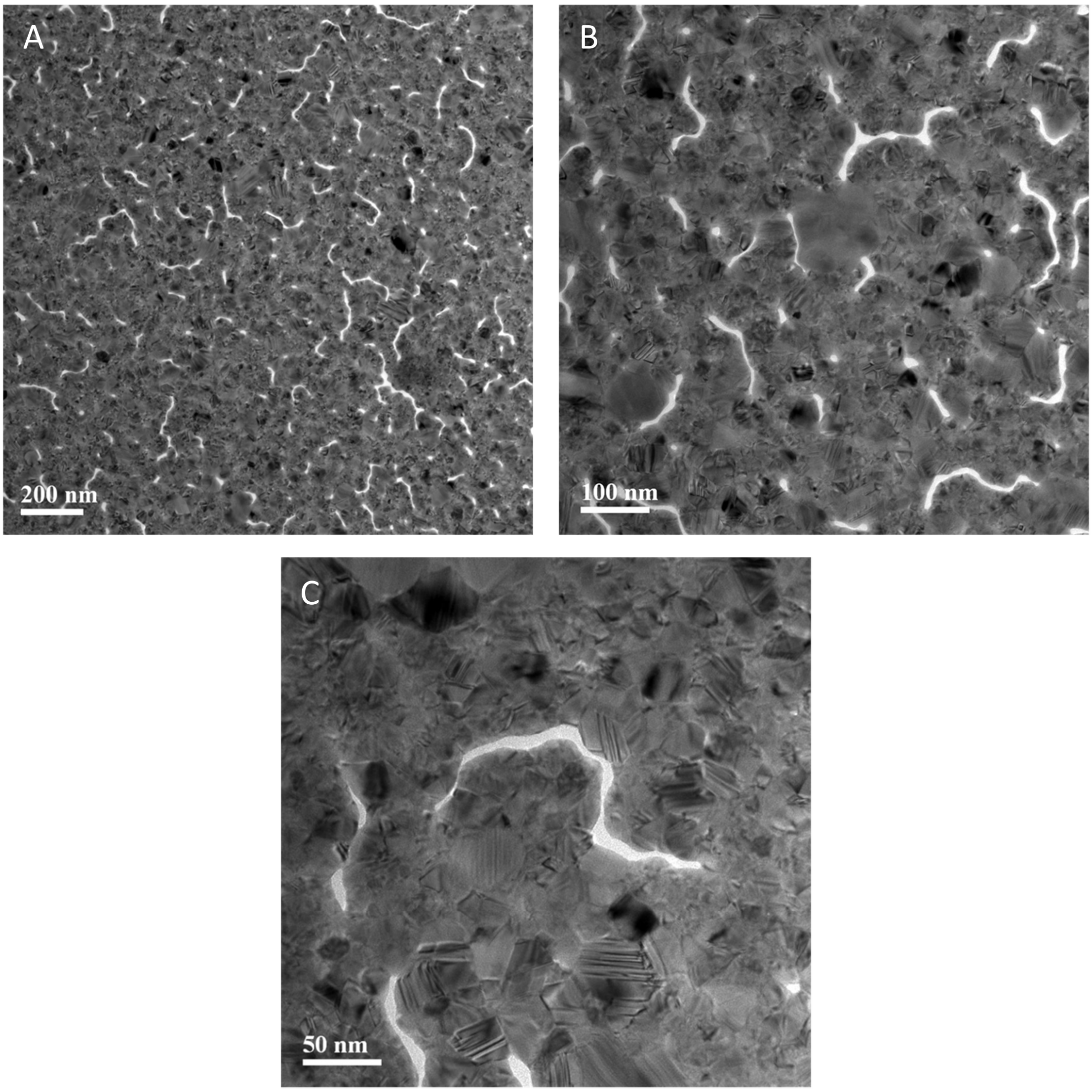

Figure 3.32: TEM BF ZL filtered images of a plan view Ag specimen of 25 nm thickness using different magnifications.

3.5.2 Diffusion of Ag into Alq_3 and Bphen

To probe the crystallographic structure of the organic layers Alq_3 and Bphen GIXD was used. The measurements were performed at the beamline W1 of the synchrotron radiation source HASYLAB (DESY, Hamburg, Germany) using a wavelength of 0.118 nm as described in the publication of Fladischer et al. (Fladischer et al., 2012). The results are presented as integrated intensities of the reciprocal space map as a function of the in-plane component q_p of the scattering vector **q**.

Figure 3.33 depicts line scans extracted from individual reciprocal space maps integrated up to 0.65 $Å^{-1}$ along the out-of-plane component of the scattering vector (q_z) of the pristine SiO_2 substrate (black curve), the Alq_3 layer (red curve), and the Bphen layer (blue curve) as a function of the in-plane component of the scattering vector (q_p). SiO_2 was used as substrate for both organic materials due to its low surface roughness. Our data clearly evidence amorphous growth of Alq_3 on the amorphous SiO_2 substrate and, in contrast, crystalline growth of Bphen. The Bphen diffraction peaks were indexed by the unit-cell parameters published recently by Li et al. (Li et al., 2007). (Fladischer et al., 2012)

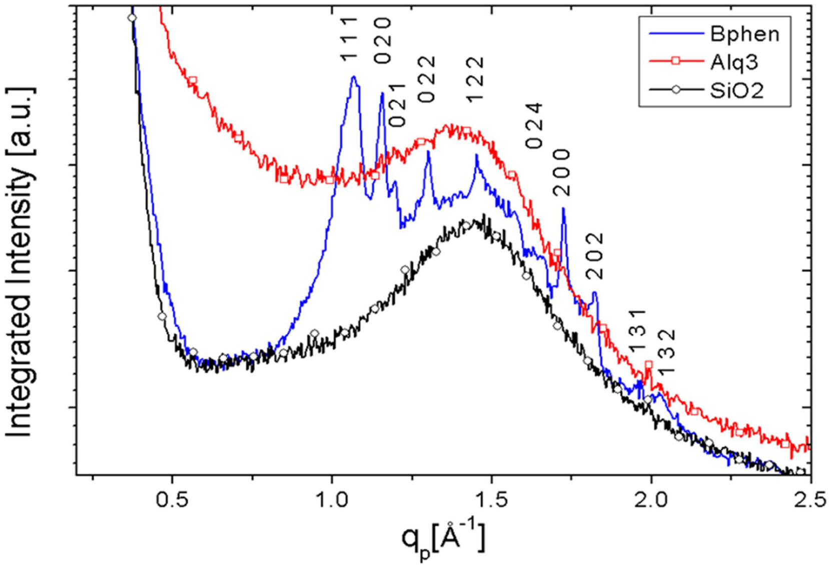

Figure 3.33: Intensity of the reciprocal space map (integrated along q_z) as a function of the in-plane component of the scattering vector (q_p) from GIXD. Black curve: amorphous SiO_2 substrate; red curve: amorphous Alq_3 layer; blue curve: crystalline Bphen layer with the corresponding Miller indices. (Fladischer et al., 2012)

Samples for studying the interfaces were deposited on silicon wafers with 150 nm thermally oxidized SiO_2 (from Siegert Consulting e.K.). The organic blocking layer materials Alq_3 and Bphen were deposited with a nominal film thickness of 40 nm. For these samples a 20 nm thin Ag layer was chosen enabling accurate XRR measurements. For each organic/Ag configuration two samples, one for TEM and one for XRR investigations, were produced simultaneously to guarantee their equality. Ag deposition using VTE was performed at different deposition rates, 0.02, 0.1, 0.5, and 1 nm/s. The deposition rates for EBD and IBS were 0.03 and 0.7 nm/s, respectively.

For the TEM characterization of the present organic/metal interfaces BF imaging was performed to get spatially resolved information about the morphology of the different materials and their interfaces. Additionally, HAADF imaging was used to gain contrast between the organic materials and the Ag layer due to the dependence of electron scattering on the atomic number. For each specimen the interfaces were investigated over a range of 5 µm (i.e., width of lamella) and the presented images are representative for the whole lamella.

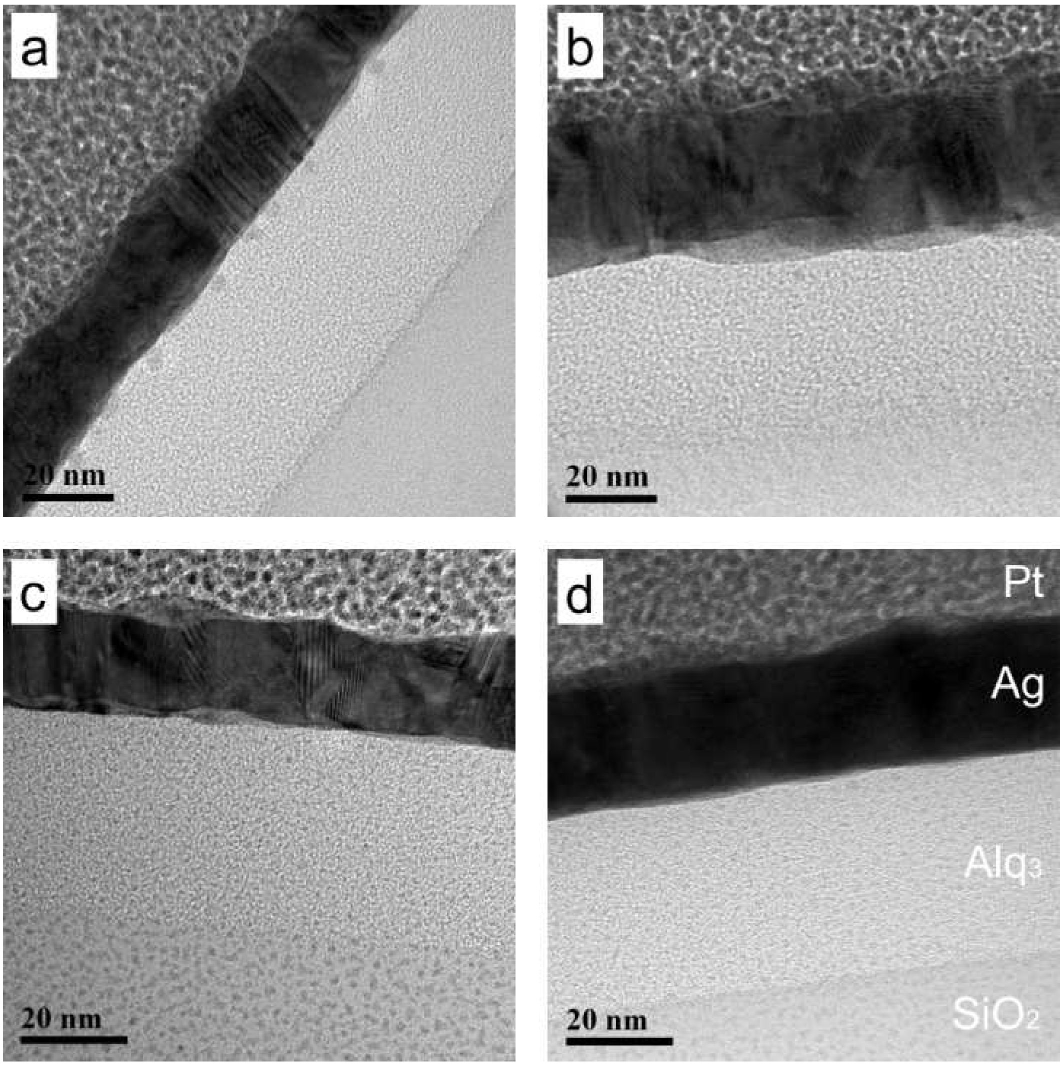

Figure 3.34: TEM cross-section images of the SiO_2/Alq_3/Ag stack with an additional Pt protection layer. The Ag layers were deposited on Alq_3 by (a) vacuum thermal evaporation with a deposition rate of 0.02 nm/s and (b) 1 nm/s, by (c) electron beam deposition and (d) ion beam sputtering. (Fladischer et al., 2012)

In Figure 3.34, TEM BF ZL filtered cross-section images of the Alq_3/Ag stacks on Si/SiO_2 substrates using different Ag deposition techniques are shown. In all images the lowest layer is the SiO_2 substrate followed by Alq_3, Ag and the Pt protection layer. Figure 3.34a represents a specimen where Ag was deposited by VTE with the lowest investigated deposition rate of 0.02 nm/s. There, Ag diffusion into Alq_3 can clearly be observed by means of small Ag particles at the interface penetrating into the organic layer over a range of approximately 6 nm. Additional EDXS measurements proved these particles to be Ag. Similar Ag diffusion to a smaller extent was detected for the samples where Ag was deposited by VTE with the highest investigated deposition rate of 1 nm/s (Figure 3.34b). Interestingly, the diffusion depth is essentially identical, whereas the amount of diffused Ag particles is significantly reduced. This clearly indicates that Ag deposition on Alq_3 using VTE induces Ag diffusion into the organic layer. Moreover, depending on the deposition rate Ag diffusion occurs to a varying extent: the lower the deposition rate the more Ag diffuses into Alq_3. Images c and d in Figure 3.34 display the specimens with Ag top layers deposited by EBD and IBS, respectively. In both cases, no Ag particles penetrating into Alq_3 were observed. Therefore, obviously, Ag diffusion into Alq_3 can be minimized by choosing EBD or IBS as deposition technique.

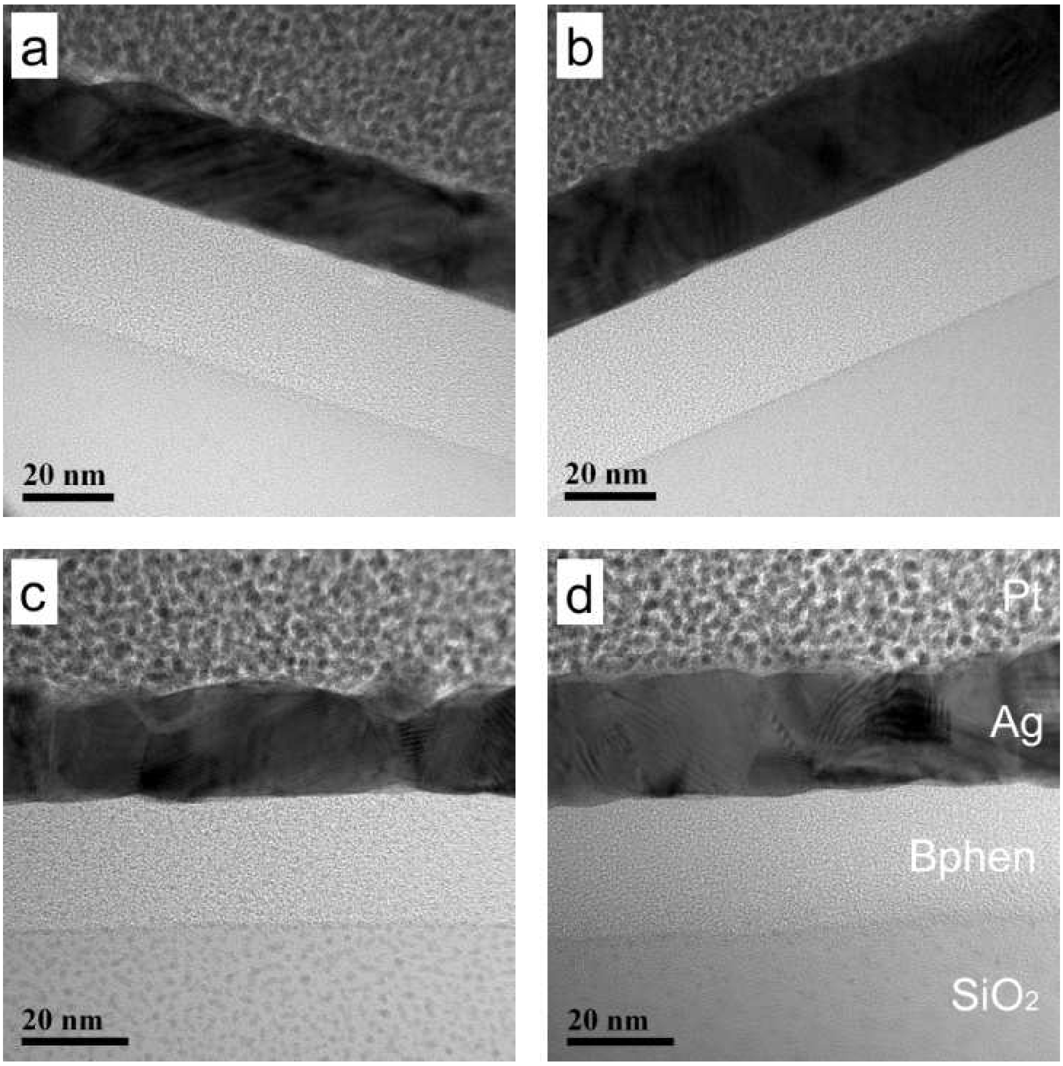

Figure 3.35: TEM cross-section images of the SiO_2/Bphen/Ag stack with an additional Pt protection layer. The Ag layers were deposited on Bphen by (a) vacuum thermal evaporation with a deposition rate of 0.02 nm/s and (b) 1 nm/s, by (c) electron beam deposition and (d) ion beam sputtering. (Fladischer et al., 2012)

Figure 3.35 shows TEM cross-section images of the Bphen/Ag stacks on Si/SiO$_2$ substrates using different Ag deposition techniques. The images show the same assembly as in Figure 3.34 for Alq$_3$ with Bphen instead. Images a and b in Figure 3.35 depict Ag deposited by VTE at deposition rates of 0.02 and 1 nm/s, respectively. Figure 3.35c displays Ag deposited by EBD and d shows IBS deposited Ag. In the case of Bphen, no Ag diffusion was observed, regardless of both deposition technique and rate. Furthermore, comparing the interfaces to Ag of the two organic materials, it is evident that the interface of Bphen to Ag is significantly more defined than that of Alq$_3$. (Fladischer et al., 2012)

XRR measurements were performed to obtain information on layer thickness, interface roughness and electron density of the respective layers. The XRR measurements were performed on a Panalytical Empyrean Reflectometer as outlined in the publication of Fladischer et al. (Fladischer et al., 2012), where the analysis of the XRR data is also explained in detail. Figure 3.36 shows the experimental XRR data (black dots) of the Si/SiO$_2$/Alq$_3$/Ag and Si/SiO$_2$/Bphen/Ag samples for different deposition techniques of the top Ag layer together with the corresponding fits (lines). Note that in the case of Alq$_3$ the experimental data had to be fitted with an additional layer between Alq$_3$ and Ag to improve the quality of the fit. Without this layer, the minima of the Kiessig fringes could not be reasonably reproduced. The introduction of such an additional layer was already reported by Gautier et al. (Gautier et al., 1996). The parameters of this additional layer depend on the deposition technique as well as the deposition conditions. In Figure 3.37, the thickness and electron density of this additional layer are depicted. The rather thin additional layers (0.5 - 2.3 nm) exhibit increased electron densities compared to that of pure Alq$_3$ (0.42 Å^{-3}). Its thickness in combination with its electron density can be interpreted in terms of diffusion depth and amount of diffused metal. The thickness of the diffusion layer is largest when the deposition rate is lowest, and therefore, decreases with increasing deposition rate, which is fully in-line with our TEM results. For EBD and IBS, where no Ag diffusion could be detected by TEM, the thickness of the additional layer, proposed for the XRR fit, is significantly lower (0.5 - 1 nm), which is in the range of the interface roughness (0.5 nm). In contrast to the Alq$_3$ multilayer stack, the simulations for Bphen could be properly performed without any diffusion layers, which points to a well-defined Bphen/Ag interface and no Ag diffusion into the subjacent organic material, which is, again, in good agreement with our TEM results. (Fladischer et al., 2012)

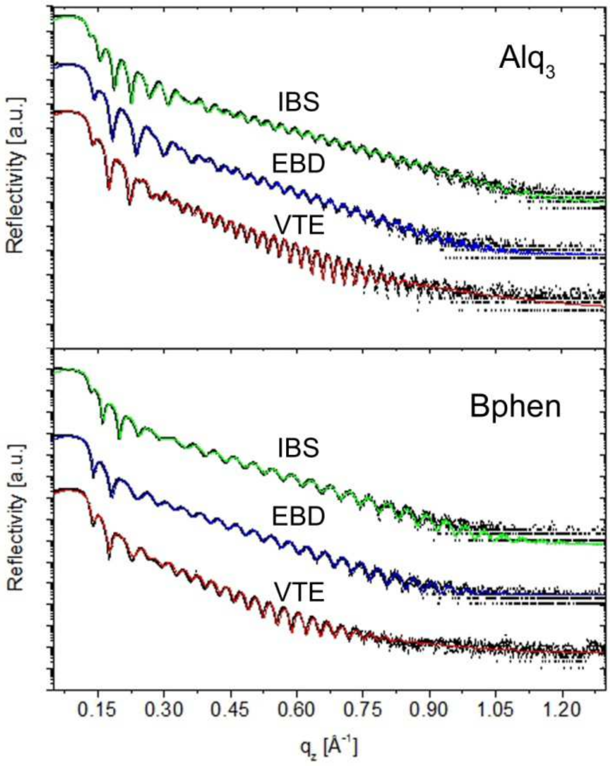

Figure 3.36: XRR measurements (black dots) and fitted data (full lines) of the Si/SiO$_2$/Alq$_3$/Ag and the Si/SiO$_2$/Bphen/Ag stacks. The figures compare samples with Ag layers deposited by ion beam sputtering (IBS, green line), electron beam deposition (EBD, blue line) and vacuum thermal evaporation (VTE, deposition rate 0.02 nm/s). (Fladischer et al., 2012)

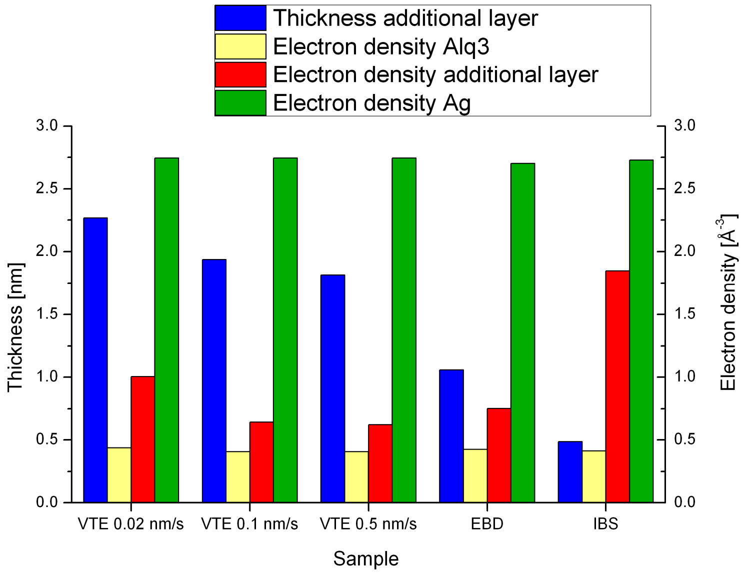

Figure 3.37: XRR fit for the additional layer (diffusion layer) introduced between Alq$_3$ and Ag in the simulation. Its thickness and electron density are depicted together with the electron densities of Alq$_3$ and Ag for the different samples, where Ag is deposited by vacuum thermal evaporation (VTE) at various deposition rates (0.02, 0.1, 0.5 nm/s), electron beam deposition (EBD), and ion beam sputtering (IBS). (Fladischer et al., 2012)

Overall, the results of our TEM and XRR investigations are both qualitatively and quantitatively in good agreement and, hence, corroborate each other. From these results, it becomes clear that Ag diffusion essentially depends on the nature of subjacent organic material. We attribute the different Ag diffusion behavior into the two different organic materials to the degree of order within the organic layers: Severe diffusion into amorphous Alq_3 occurs while a well-defined organic/metal interface in case of crystalline Bphen exists. Furthermore, the deposition technique has a substantial impact on the diffusion behavior and the interface morphology, which all is confirmed by the I-V characteristics.

This work shows that the combination of TEM and XRR represents a powerful nanoanalytical toolset perfectly suited for the characterization of organic electronic devices. The diffusion behavior of Ag could therewith be elucidated: No Ag diffusion was detected in the case of crystalline Bphen, whereas Ag diffusion of varying extent was observed for amorphous Alq_3, which depends on both the deposition technique and the deposition rate. Ag deposited on Alq_3 using VTE induces Ag diffusion: the lower the deposition rate the more Ag diffuses into Alq_3. In contrast, no Ag diffusion was detected for Ag deposited by EBD and IBS. The Ag diffusion behavior therefore clearly depends on the crystallinity of the organic materials (amorphous Alq_3 vs crystalline Bphen). Additionally, I-V characteristics confirm this material and deposition technique dependence. Regarding both the amount of diffused material and its diffusion depth, the process of Ag diffusion entails issues of short-circuits and the transition to ohmic diode characteristics. Clearly, to optimize the device performance, an appropriate deposition parameter set needs to be found for each individual material stack. In the present case for OPDs, the most reliable production strategy consists of using Bphen in combination with Ag deposited by VTE with the lowermost deposition rate.

4 Quantitative EDXS analysis

EDXS is not only a method to qualitatively analyze specimens in TEM but also offers the opportunity to perform quantitative analyses. Historically, in material science the Cliff-Lorimer ratio technique was used most frequently. In addition the ζ-factor method was developed later.

In 1975 Cliff and Lorimer introduced the Cliff-Lorimer ratio technique for quantitative thin-film microanalysis (Cliff & Lorimer, 1975). A condition of using the Cliff-Lorimer ratio technique is the thin-film criterion, which assumes that the specimen is thin enough that any absorption or fluorescence can be neglected. If the thin-film criterion is fulfilled and the characteristic X-ray peaks are measured simultaneously, the compositions of the constituent elements are related to the measured characteristic X-ray intensities above background as:

$$\frac{c_A}{c_B} = k_{AB} \frac{I_A}{I_B} \tag{4.1}$$

c_A, c_B … concentration in weight percents (wt%) of element A and B
I_A, I_B … characteristic X-ray intensities above background of element A and B
k_{AB} … proportionality factor (Cliff-Lorimer factor)

Thus the composition (in wt%) of a specimen can be determined in a straightforward way when the Cliff-Lorimer factors are known. The Cliff-Lorimer factors are sensitivity factors varying according to the TEM-EDXS system, the acceleration voltage and the elements. These factors can be determined either theoretically by calculation from first principles or experimentally. The theoretical determination of the sensitivity factors is a fast and easy method whereas the experimental determination using standards is slow and laborious. Nevertheless, as the theoretical determination produces errors of ± 15 – 20% (Maher et al., 1981, Newbury et al., 1984) sensitivity factors should be determined experimentally when an accuracy of ± 1% is desired (Wood et al., 1984, Sheridan, 1989). At our institute the sensitivity factors were determined experimentally for the Tecnai F20 (Fladischer, 2009).

However, if the thin-film criterion is not fulfilled, the Cliff-Lorimer approach breaks down mainly due to the problem of absorption. Absorption can arise if the specimen is too thick and/or characteristic X-rays have energies below 1-2 keV (i.e. light-element analysis). In the case of absorption less X-ray counts are detected than generated and thus the concentration is no longer simply proportional to the intensity of the element. As a consequence the absorption-correction factor (ACF) was introduced (Goldstein et al., 1977):

$$ACF = \frac{\int_0^t \left(\varphi_B(\rho t) e^{-\left(\frac{\mu}{\rho}\right]_{Spec}^{B} \rho t \ cosec \ \alpha\right)} \right) d(\rho t)}{\int_0^t \left(\varphi_A(\rho t) e^{-\left(\frac{\mu}{\rho}\right]_{Spec}^{A} \rho t \ cosec \ \alpha\right)} \right) d(\rho t)} \tag{4.2}$$

ACF … absorption-correction factor
$\varphi_A(\rho t), \varphi_B(\rho t)$ … depth distribution of X-ray production
$\left.\frac{\mu}{\rho}\right]_{Spec}^{A}, \left.\frac{\mu}{\rho}\right]_{Spec}^{B}$ … mass absorption coefficient of element A and B in the specimen
ρ … density of the specimen
t … thickness of the specimen
α … take-off angle

Furthermore, it is assumed that a uniform distribution of X-rays is generated at all depths throughout a thin film (Philibert, 1963). Thus the depth distribution of X-ray production is assumed to be a constant and equal to unity, which results in the following expression for the absorption-correction factor:

$$ACF = \left(\frac{\left.\frac{\mu}{\rho}\right]_{Spec}^{A}}{\left.\frac{\mu}{\rho}\right]_{Spec}^{B}} \right) \left(\frac{1 - e^{-\left(\frac{\mu}{\rho}\right]_{Spec}^{B} \rho t \ cosec \ \alpha\right)}}{1 - e^{-\left(\frac{\mu}{\rho}\right]_{Spec}^{A} \rho t \ cosec \ \alpha\right)}} \right) \tag{4.3}$$

The mass absorption coefficients can be found in literature for every element (e.g. Heinrich (Heinrich, 1987)) and the take-off angle is adjusted by the TEM operator. The crucial required parameters for absorption correction are the density and the thickness of the specimen (i.e. mass-thickness).

To apply an absorption correction the knowledge of the mass-thickness is required at each analysis position. Inaccuracies in the measurements of the mass-thickness cause errors in the quantitative analysis. There are several ways to determine the thickness of the analyzed region, e.g. the contamination-spot separation method, the convergent-beam diffraction method (Kelly et al., 1975, Allen, 1981) or the EELS method (Egerton, 1996). However, none of these methods are convenient, accurate and universally applicable.

To avoid the necessity to determine the mass-thickness of every analyzed region extrapolation methods were introduced by Van Capellen and Horita (Van Cappellen, 1990, Horita et al., 1987) and further refined by Eibl (Eibl, 1993). For these absorption correction approaches the knowledge of the mass-thickness is obsolete, still the acquisition of various

EDX spectra at different specimen thicknesses is necessary. Thus this method is not easily applicable to homogeneous thin film samples. Another approach called K:L intensity ratio method or differential X-ray absorption method (e.g. Morris et al. and Horita et al. (Morris et al., 1980, Horita et al., 1989)) utilizes the difference in relative X-ray absorption between two emitted X-ray lines from the same element (i.e. K and L or L and M lines). This approach is limited by the requirement of two different X-ray lines from the same element resulting in the restriction to quantify specimens containing elements with Z > 20 (Ca).

To overcome these limitations caused by X-ray absorption the ζ-factor method was proposed in 2006 by Watanabe and Williams (Watanabe & Williams, 2006) based on the previous approach (Watanabe et al., 1996, Watanabe & Williams, 1999, Watanabe & Williams, 2003). The ζ-factor method is a quantitative thin-film X-ray analysis procedure overcoming the two major limitations of the Cliff-Lorimer ratio technique, (i) use of pure-element standards rather than multielement standards and (ii) the possibility of applying an X-ray absorption correction as it yields the mass-thickness. The absorption correction facilitates light-element analysis and enables more accurate quantification results. (Watanabe & Williams, 2006)

Due to the advantages of the ζ-factor method we decided to set it up at both TEM-EDXS systems which is explained in detail in the following chapters together with the theory of the ζ-factor method.

4.1 The ζ-factor method

This chapter outlines the theory of the ζ-factor method following the paper of Watanabe and Williams (Watanabe & Williams, 2006).

If the thin-film criterion is valid meaning that absorption and fluorescence are negligible, the measured characteristic X-ray intensity is proportional to the mass-thickness and the composition. Thus the mass-thickness can be related to the measured X-ray intensity normalized by the composition:

$$\rho t = \zeta_A \frac{I_A}{c_A D_e} \tag{4.4}$$

ρt … mass-thickness (ρ … density, t … thickness)
ζ_A … proportionality factor
I_A … intensity of the characteristic X-ray line of element A
c_A … concentration in weight percents of element A
D_e … total electron dose during acquisition

The ζ-factor is a proportionality factor connecting I_A to ρt and c_A, and the total electron dose during acquisition is defined as follows:

$$D_e = N_e I_p \tau \tag{4.5}$$

D_e … total electron dose during acquisition
N_e … number of electrons (electron counts) in a unit electric charge
I_p … beam current
τ … acquisition time

Due to the insertion of the electron dose term the ζ-factor is not dependent on the acquisition time or the beam current, which was the case in the previous approach (Watanabe et al., 1996, Watanabe & Williams, 1999, Watanabe & Williams, 2003). Thus the ζ-factor does not need to be adjusted for individual experimental conditions with different beam currents or different acquisition times.

In the thin-film approximation the measured X-ray intensity can theoretically be described by the following equation e.g. (Armigliato, 1992):

$$I_A = N \frac{Q_A \omega_A a_A}{A_A} c_A \rho t \, D_e \left(\frac{\Omega}{4\pi}\right) \varepsilon_A \tag{4.6}$$

I_A … intensity of the characteristic X-ray line of element A
N … Avogadro's number
Q_A … ionization cross-section
ω_A … X-ray yield for the characteristic X-rays
a_A … relative transition probability
A_A … atomic weight
c_A … weight fraction of the element
ρt … mass-thickness (ρ … density, t … thickness)
D_e … total electron dose during acquisition
Ω/(4π) … solid angle in the whole 4π space
ε_A … detector efficiency

Comparing this equation with equation (4.4) the ζ-factor results in:

$$\zeta_A = \frac{A_A}{N Q_A \omega_A a_A \left(\frac{\Omega}{4\pi}\right) \varepsilon_A} \tag{4.7}$$

All parameters associated with X-ray generation in a thin specimen and X-ray detection are incorporated in the ζ-factor. The ζ-factor is dependent on the X-ray energy and the accelerating voltage and is independent of the total electron dose, specimen composition, thickness and density. This independence makes any absorption correction trivial. (Watanabe & Williams, 2006)

The explicit parameters on which the ζ-factors depend are explained in this paragraph. Some parameters have already been explained previously such as the X-ray yield for the characteristic X-rays (see chapter 2.1 and equation (2.1)), the solid angle (see chapter 2.4.2) and the detection efficiency (see chapter 2.2.3). Another parameter is the ionization cross-section Q representing the probability of ionization of a particular electron shell by an incident electron. A lot of different models were developed for the determination of the ionization cross-section. Nevertheless there is considerable uncertainty about the absolute value of Q because few reliable experimental measurements have been made at TEM voltages. Most models are variations on the original expression of Bethe (Bethe, 1930):

$$Q = \frac{b_{n1} \pi e^4 Z_{n1}}{(m_0 v^2/2) E_C} ln\left(\frac{c_{n1}(m_0 v^2/2)}{E_C}\right) \tag{4.8}$$

Q … ionization cross-section of the n1 shell
e … electron charge
Z_{n1} … number of electrons in the n1 shell
m_0 … rest mass of the electron
v … velocity of the incident electron
E_C … ionization energy of the shell
b_{n1}, c_{n1} … empirically derived factors (Bethe parameters)

Due to the high accelerating voltages used in TEM, Q has to be corrected for relativistic effects. Therefore Williams (Williams, 1933) modified the original Bethe cross-section (equation (4.8)) by incorporating terms to correct for deviations of the mass and the velocity of the incident beam electron, resulting in:

$$Q = \frac{b_{n1} \pi e^4 Z_{n1}}{(m_0 v^2/2) E_C} \left[ln\left(\frac{c_{n1}(m_0 v^2/2)}{E_C}\right) - ln(1-\beta^2) - \beta^2 \right] \tag{4.9}$$

β … ratio of the electron velocity v to the velocity of light c

Based on this Bethe approach different modifications have been developed yielding different cross section models (e.g. (Mott & Massey, 1949, Green & Cosslett, 1961, Brown, 1974, Powell, 1976, Schreiber & Wims, 1981, Jakoby et al., 1987, Paterson et al., 1989)) and hence different Q values, which introduce a severe uncertainty for the theoretical determination of ζ-factors.

The remaining parameter on which the ζ-factor depends is the relative transition probability, which describes the fact that if a K-shell electron is ionized and returns to ground state through X-ray emission, it can emit either a Kα or Kβ X-ray. The fraction of Kα X-rays in relation to the total intensity of the K spectrum is given by the relative transition probability, which is valid for L and M lines as well:

$$a = \frac{I(K_\alpha)}{I(K_{tot})} \tag{4.10}$$

a ... relative transition probability
$I(K_\alpha)$ … intensity of the Kα X-rays
$I(K_{tot})$ … total intensity of the K X-rays

For the quantification of an EDX spectrum of a specimen a similar relationship to equation (4.4) is established for element B:

$$\rho t = \zeta_B \frac{I_B}{c_B D_e} \tag{4.11}$$

Assuming a binary system ($c_A + c_B = 1$) the mass-thickness and the composition can be expressed as follows:

$$\rho t = \frac{\zeta_A I_A + \zeta_B I_B}{D_e}, \quad c_A = \frac{\zeta_A I_A}{\zeta_A I_A + \zeta_B I_B}, \quad c_B = \frac{\zeta_B I_B}{\zeta_A I_A + \zeta_B I_B} \tag{4.12}$$

This approach can be easily expanded to any multi-component systems using $\sum_j c_j = 1$. Thus the composition and the mass-thickness can be determined simultaneously from measured X-ray intensities. Additionally the specimen thickness can be obtained if the specimen density is known at the analyzed region.

If X-ray absorption within the specimen cannot be neglected a subsequent absorption correction can be performed. Note that X-ray absorption of 10% occurs for element A within the specimen if $\left.\frac{\mu}{\rho}\right]_{Spec}^{A} \rho t = 0.1$ for a take-off angle of 29.6°. Concerning the ζ-factor method an absorption-correction factor is calculated using the resulting mass-thickness of equation (4.12):

$$ACF_A = \frac{\left.\frac{\mu}{\rho}\right]_{Spec}^{A} \rho t \ cosec \ \alpha}{1 - e^{-\left.\frac{\mu}{\rho}\right]_{Spec}^{A} \rho t \ cosec \ \alpha}} \tag{4.13}$$

ACF$_A$ … absorption-correction factor for element A

$\left.\frac{\mu}{\rho}\right]_{Spec}^{A}$ … mass absorption coefficient of element A

ρt … mass-thickness (ρ … density, t … thickness)

α … take-off angle

This absorption-correction factor is then incorporated by multiplying it by the corresponding X-ray intensities in equation (4.12), thus giving:

$$\rho t = \sum_{j}^{N} \frac{\zeta_j I_j \ ACF_j}{D_e}, \quad c_A = \frac{\zeta_A I_A \ ACF_A}{\sum_j^N \zeta_j I_j \ ACF_j} \ , \ldots , \ c_N = \frac{\zeta_N I_N \ ACF_N}{\sum_j^N \zeta_j I_j \ ACF_j} \tag{4.14}$$

An iterative process is required to solve these equations for the composition and mass-thickness since the absorption-correction factors require the mass-thickness. This iteration is straightforward and converges fast, e.g. only 10 – 15 iterations are typically required to converge to less than 0.001 wt% differences in composition.

If the ζ-factors are known, absorption corrected quantitative analysis with simultaneous mass-thickness determination is performed in a straightforward way for the measured characteristic X-ray intensities of an EDX spectrum and according acquisition parameters, which are the acquisition time and the beam current. The beam current measurement is a requirement of the ζ-factor method and at the same time its major disadvantage. Systematic errors in the beam-current measurements will directly influence the mass-thickness determination and hence the subsequent absorption correction. The TEM needs to be equipped with either a Faraday cup or another current measuring device (e.g. calibrated fluorescent screen, camera, or post-column energy filter). If the beam current fluctuates significantly, the ζ-factor method is difficult to apply; if there is no possibility of beam current measurements the ζ-factor method is not applicable. Fortunately, modern TEMs equipped with a Schottky FEG provide a stable beam current, which means that the beam current fluctuation should be less than a few percent for typical time periods of analysis or mapping. For X-FEGs the beam current stability could be improved exhibiting fluctuations below 1% in 1 min (Freitag, 2013). Ideally the beam current is measured before and after EDXS acquisition. In our case the CCD cameras of the GIFs were calibrated and images of the focused electron beams were analyzed for accurate electron beam current measurements.

4.2 Determination of ζ-factors

Quantitative X-ray analysis using the ζ-factor method is straightforward if the ζ-factors are known. The ζ-factors are sensitivity factors varying for every element and TEM-EDXS system. Looking at equation (4.7) it can be seen that the ζ-factor depends on the high voltage of the TEM, as it strongly affects the ionization cross section, on the solid angle and the detector efficiency, which reflect the TEM-EDXS interface and the detector system according to the X-ray energy (see chapters 2.4.2 and 2.2.3) and on the atomic number of the element, which affects the atomic weight, the X-ray yield and the relative transition probability, where latter two again are influenced by the X-ray energy of the element. The main error source for theoretical calculation of the ζ-factor according to equation (4.7) is the ionization cross section, as already outlined in chapter 4.1. In addition the detector related parameters are often not known precisely, which further increases the uncertainty of calculated ζ-factors. As the correct determination of sensitivity factors is crucial for the accuracy of the quantification results, the ζ-factors should be determined experimentally for each TEM-EDXS system using standard specimens. For the experimental determination of a ζ-factor the mass-thickness and composition of the standard, the characteristic X-ray intensity of the relevant element and the acquisition parameters, which are the acquisition time and the beam current, need to be known or measured.

As the ζ-factor consists of information from only one single element pure element thin film standards can be used for the experimental determination of the ζ-factors in addition to thin films of known composition. The option of using pure element standards is an advantage of the ζ-factor method over the Cliff-Lorimer ratio technique as pure element standards are robust, cheap, easy to fabricate and insensitive to un-noticed specimen drift. Additionally they do not change composition during the thinning process or as a result of beam damage.

If quantitative X-ray analysis is performed on unknown multielement specimens, ζ-factors are required for all elements of the specimen. To reduce the tedious work of determining ζ-factors for every element a simplified approach was developed (Watanabe & Williams, 2006). Therefore a set of ζ-factors for K-shell X-ray lines can be estimated from a spectrum generated from the NIST SRM 2063a thin film glass standard (Reed, 1993). SRM 2063a contains the elements Mg, Si, Ca, Fe and O and its composition, thickness and density are known to a high degree of accuracy. By measuring an EDX spectrum from the SRM 2063a standard, the ζ-factors for the K lines of its five elements can be directly determined. Based on these factors a series of ζ-factors covering a significant fraction of the periodic table can be estimated by an inter/extrapolation fitting process enabling the quantification of a multitude of elements.

Due to the advantage of obtaining a series of ζ-factors and being able to quantify a multitude of elements the SRM 2063a standard was used for the experimental determination of the ζ-factors for both TEM-EDXS systems, the Si(Li) detector on the Tecnai F20 and the Super-X detector on the Titan³, being explained in the following two chapters.

4.2.1 ζ-factors of the Si(Li) detector

The ζ-factors for the Si(Li) detector of the Tecnai F20 were determined experimentally following the above mentioned method described in the paper of Watanabe and Williams (Watanabe & Williams, 2006) using a NIST SRM 2063a standard on a Cu grid (Reed, 1993) and the program “zetazDet” of M. Watanabe. This work is published in the paper of Fladischer and Grogger (Fladischer & Grogger, 2013). For the determination of the ζ-factors several spectra of the standard were acquired in STEM mode with a specimen tilt of 15° towards the detector, a beam current of 352 pA and an acquisition time of 100 s. An area of 2 μm^2 was scanned during acquisition to prevent the specimen from damage. In order to yield good statistics and to obtain the ζ-factors for this system 13 spectra of the SRM 2063a standard were analyzed. One of the spectra is displayed in Figure 4.1 showing the characteristic X-ray peaks of O, Mg, Si, Ca, Fe and Ar as well as a C peak caused by contamination.

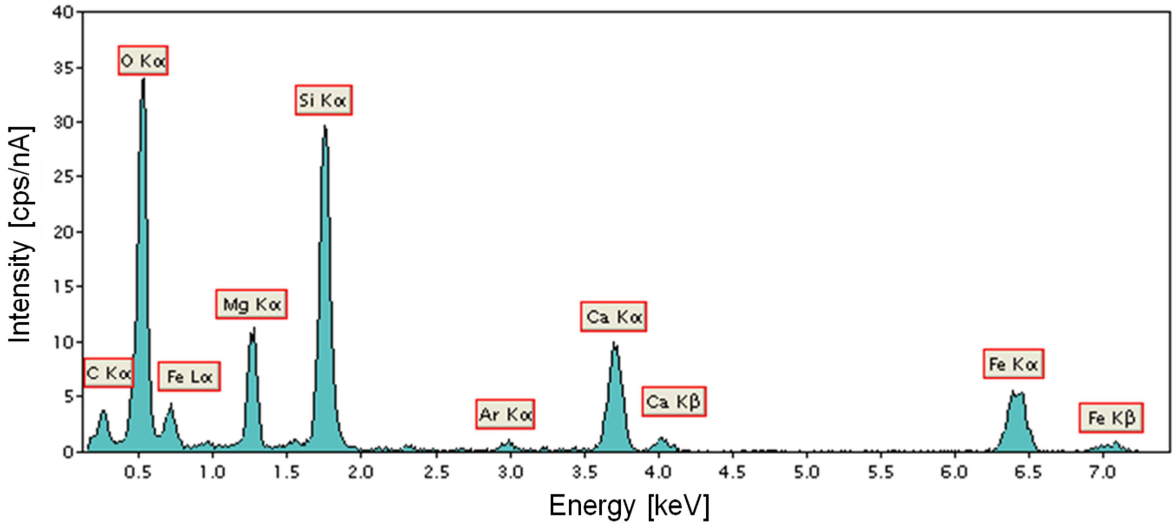

Figure 4.1: EDX spectrum of the SRM 2063a standard acquired with the Si(Li) detector.

The ζ-factors of the K lines of O, Mg, Si, Ca and Fe were determined directly from the EDX spectra of the SRM 2063a standard according to equation (4.4). Ar, which is present in the specimen with only 0.4 wt%, was not used for the experimental determination of the ζ-factor, as the peak is too small for reliable ζ-factor determination. The intensities of the O, Mg, Si, Ca and Fe peaks were determined by fitting Gaussians to the Kα peaks. The resulting ζ-factors of the K lines are ζ_{O} = (1862 ± 41) kg·electron/(m^2·photon), ζ_{Mg} = (1277 ± 17) kg·electron/(m^2·photon), ζ_{Si} = (1354 ± 14) kg·electron/(m^2·photon), ζ_{Ca} = (1552 ± 19) kg·electron/(m^2·photon) and ζ_{Fe} = (1970 ± 25) kg·electron/(m^2·photon). The ζ-factors for K lines of the other elements were then estimated by an inter/extrapolation fitting process of the directly determined ζ-factors as explained in detail in the paper of Watanabe and Williams (Watanabe & Williams, 2006). Therefore a parameter optimization of the fit was performed concerning uncertain parameters like the ionization cross-section and the thicknesses of detector-window materials, contact layer and dead layer of the detector crystal. For this parameter optimization using Watanbe's zetazDet software up to four parameters can be fitted from the five measured ζ-factors, one of them being the ionization cross-section model and three parameters representing thicknesses of the above mentioned layers. The mass absorption coefficients of Heinrich (Heinrich, 1987), the relative intensity ratios of Fiori (Fiori et al., 1992) and the fluorescence yields of Bambynek (Bambynek, 1989) were used for the parameter optimization. The software offers 22 different ionization cross-section models for the optimization. Figure 4.2 displays the estimated ζ-factors of K lines plotted against the atomic number for the different ionization cross-section models and the directly determined ζ-factors. Note, that the estimated ζ-factors have a huge dependence on the different ionization cross-section models in particular for light elements and elements with Z > 30. The huge differences arise due to the uncertainty of the ionization cross-section values for acceleration voltages used in TEM and the different ionization cross-section model approaches as described in chapter 4.1. In this case the ionization cross-section model of Paterson (Paterson et al., 1989) yielded results fitting best to the experimentally determined ζ-values exhibiting a χ^2 value of 40 whereas other models exhibit χ^2 values of up to 200 and even 1230 for the model of Zaluzec.

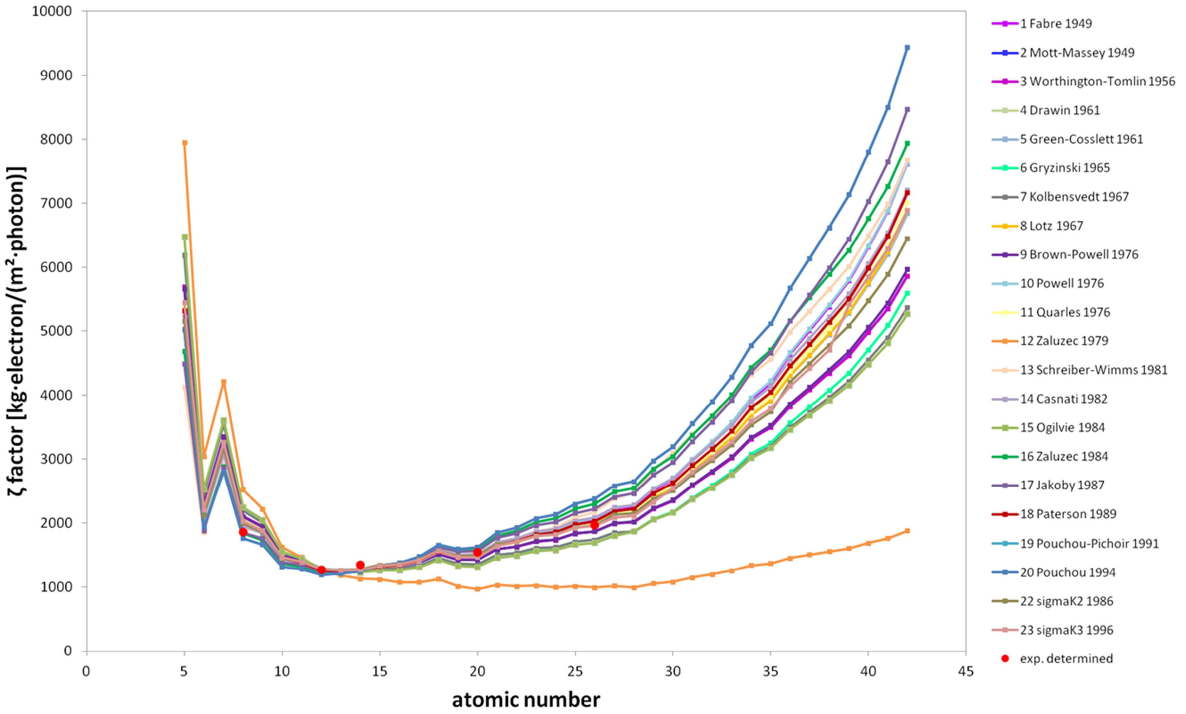

Figure 4.2: Estimated ζ-factors of K lines plotted against the atomic number for different ionization cross-section values and the directly determined ζ-factors (red dots) of the Si(Li) detector.

With the chosen ionization cross-section model of Paterson the influence of the parameter optimization varying the thicknesses of the contact layer, the crystal's dead layer, and the detector window (Al on top of Moxtek polymer) was studied. The nominal thicknesses are: $t_{\text{Au contact layer}}$ = 6 nm, $t_{\text{crystal´s dead layer}}$ = 10 nm, t_{Al} = 30 nm and $t_{\text{Moxtek polymer}}$ = 300 nm (Nicolosi, 2008, West, 2008). As only three of the four thickness parameters can be fitted, all possible combinations were performed. Figure 4.3 displays estimated ζ-factors of K lines plotted against the atomic number for different parameter optimizations concerning the thickness values and the directly determined ζ-factors. The results of the most reasonable 5 parameter optimization combinations (e.g. varying the dead and the Au layer (blue square) or varying the Au, the Moxtek and the Al layer (green square)) are displayed together with the estimated ζ-factors where no thickness parameter was varied. Especially in the low energy region below 1 keV considerable differences of the ζ-factor values arose for the different parameter optimizations. In this case the ζ-factors fitting best to the experimentally determined ζ-values resulted from optimizing the dead layer together with the window's Moxtek polymer layer leading to a χ^2 value of 18. The thickness values were changed according to the parameter optimization: $t_{\text{Au contact layer}}$ = 6 nm, $t_{\text{crystal´s dead layer}}$ = 0 nm, t_{Al} = 30 nm and $t_{\text{Moxtek polymer}}$ = 230 nm. These ζ-factors of K lines were used for further quantification of EDX spectra and are displayed in Figure 4.4 and listed in Table A.1.

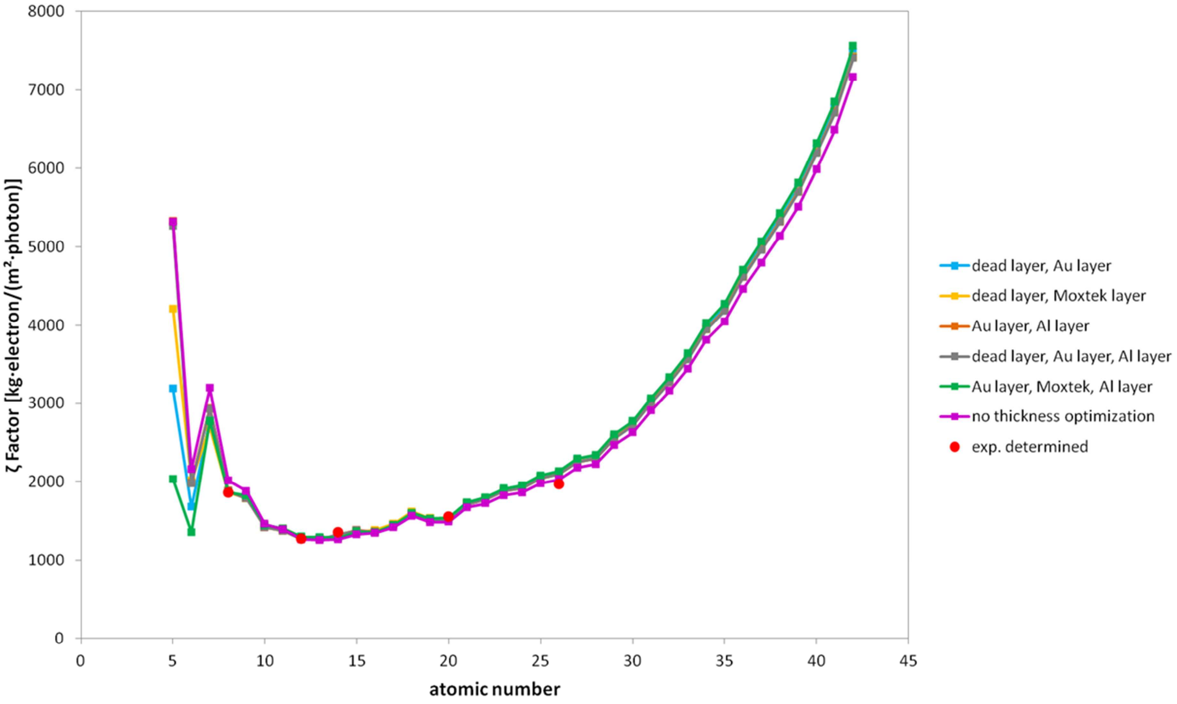

Figure 4.3: Estimated ζ-factors of K lines plotted against the atomic number for different parameter optimizations and the directly determined ζ-factors (red dots) of the Si(Li) detector.

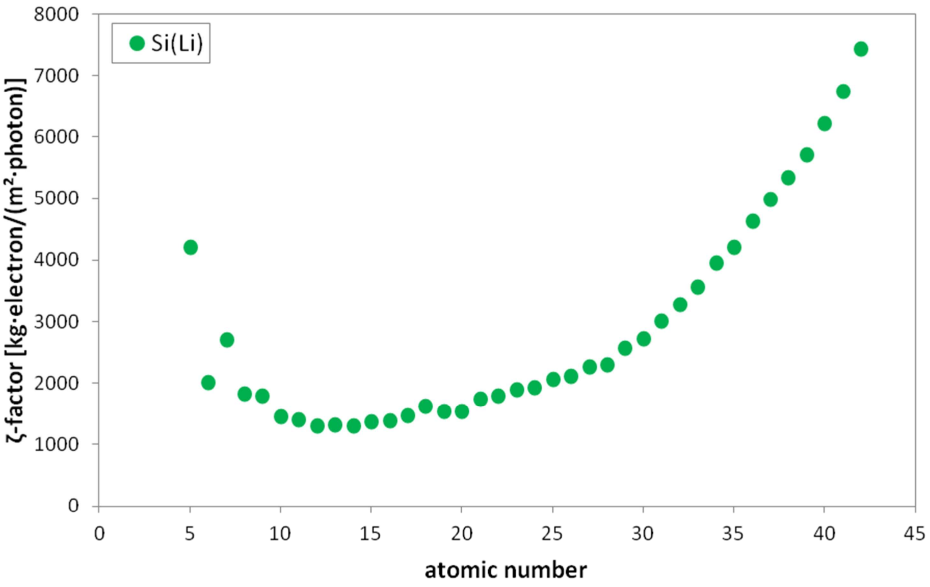

Figure 4.4: Estimated ζ-factors of K lines of the Si(Li) detector of Tecnai F20 using the ionization cross-section of Paterson and optimizing the dead layer together with the window´s polymer layer.

4.2.2 ζ-factors of the Super-X detector

Similar to the ζ-factor determination of the Si(Li) detector (see chapter 4.2.1) the ζ-factors for the Super-X detector of the Titan³ were determined experimentally following the above mentioned method using a NIST SRM 2063a standard on a Cu grid and the program "zetazDet" of M. Watanabe. Therefore several spectra of the standard were acquired in STEM mode for a high tension of 300 kV, without any specimen tilt, a beam current of 389 pA and an acquisition time of 100 s. An area of 1.7 µm² was scanned during acquisition to prevent the specimen from damage. In order to yield good statistics and to obtain the ζ-factors for this system 6 spectra of the SRM 2063a standard were analyzed. Figure 4.5 displays one of the EDX spectra of the SRM 2063a standard exhibiting the characteristic X-ray peaks of O, Mg, Si, Ca, Fe and Ar as well as a C peak caused by contamination. In comparison to the EDX spectrum acquired with the Si(Li) detector (see Figure 4.1) the detection efficiency of the Super-X detector is increased by an order of magnitude yielding better counting statistics for similar acquisition conditions.

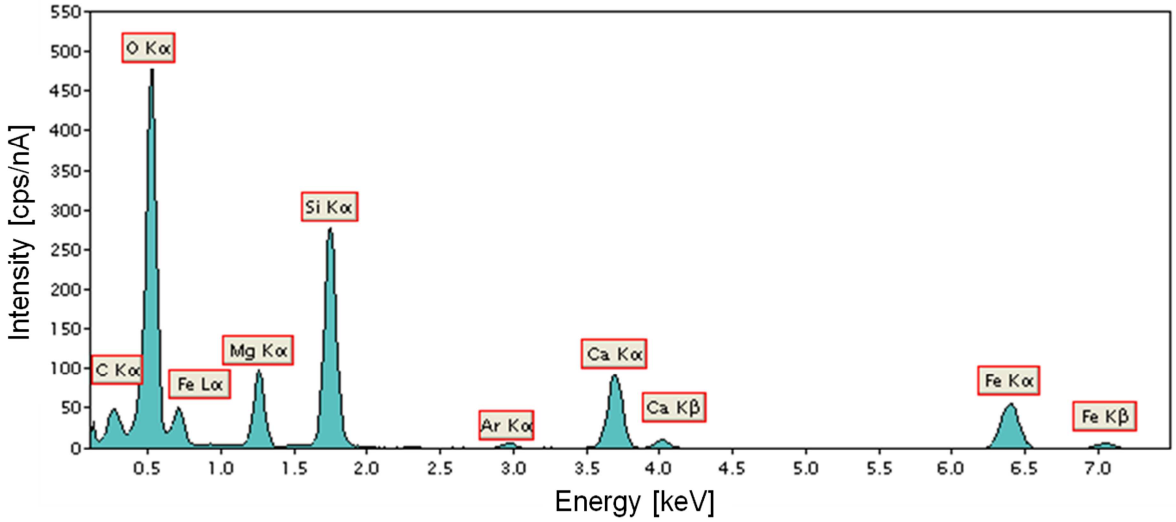

Figure 4.5: EDX spectrum of the SRM 2063a standard acquired with the Super-X detector.

Similar to the determination of the ζ-factors of the Si(Li) detector the ζ-factors of the Super-X detector of the K lines of O, Mg, Si, Ca and Fe were determined directly from the EDX spectra of the SRM 2063a standard according to equation (4.4). The resulting ζ-factors of the K lines are ζ_O = (159 ± 4) kg·electron/(m²·photon), ζ_{Mg} = (151 ± 2) kg·electron/(m²·photon), ζ_{Si} = (150 ± 1) kg·electron/(m²·photon), ζ_{Ca} = (174 ± 1) kg·electron/(m²·photon) and ζ_{Fe} = (213 ± 1) kg·electron/(m²·photon). The ζ-factors for K lines of the other elements were then estimated by an inter/extrapolation fitting process of the directly determined ζ-factors by performing a parameter optimization. The same values as in the case of the Si(Li) detector were used for the mass absorption coefficients, the relative intensity ratios and the fluorescence yields (see chapter 4.2.1). The estimated ζ-factors using the most reasonable 6 ionization cross-section models are displayed in Figure 4.6. Again the estimated ζ-factors have a huge dependence on the different ionization cross-section models in particular for light elements and elements with $Z > 30$. Again the ionization cross-section model of Paterson (Paterson et al., 1989) yielded results fitting best to the experimentally determined ζ-values exhibiting a χ^2 value of 31.

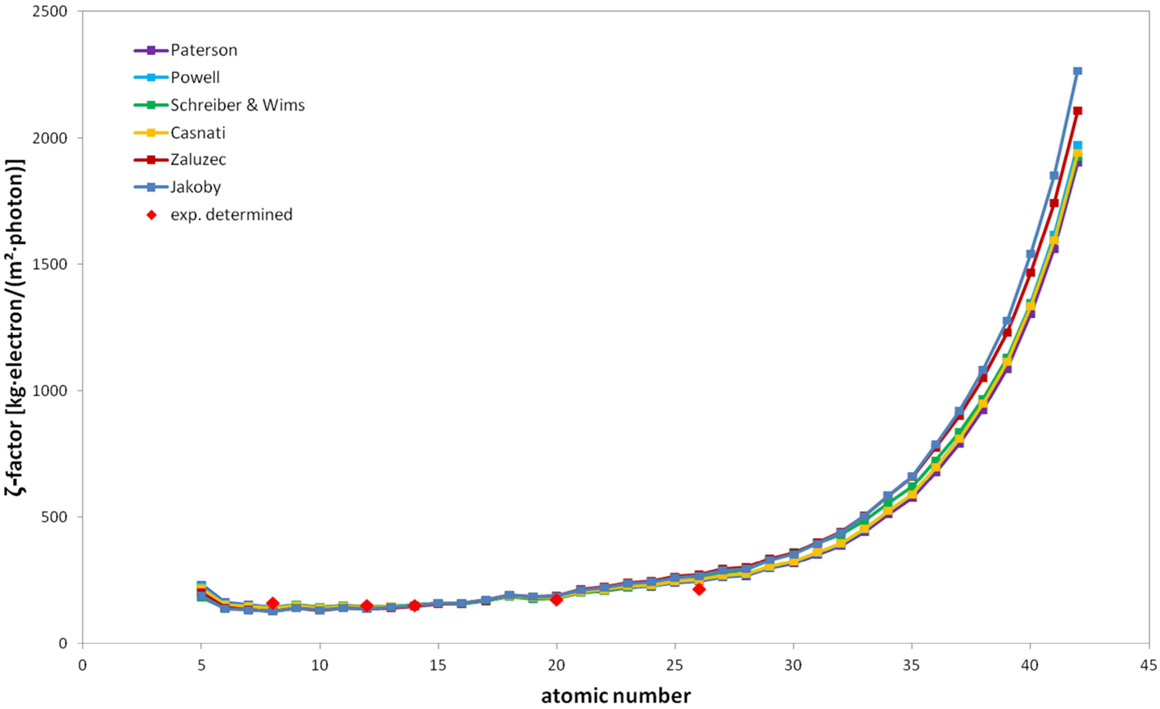

Figure 4.6: Estimated ζ-factors of K lines plotted against the atomic number for different ionization cross-sections and the directly determined ζ-factors (red dots) of the Super-X detector.

With the chosen ionization cross-section model of Paterson the influence of the parameter optimization varying the thicknesses of the contact layer (Al) and the crystal's dead layer was studied. As the Super-X detector does not possess a window only these two layer thicknesses were varied in the parameter optimization. The nominal thickness values are: $t_{\mathrm{Al\ contact\ layer}}$ = 30 nm and $t_{\mathrm{crystal's\ dead\ layer}}$ = 0 nm (Mitterbauer, 2011). Additionally the ζ-factors were estimated by using two different take-off angles, the nominal take-off angle of 18° and a take-off angle of 23° determined by coherent bremsstrahlung measurements (see chapter 2.6). Figure 4.7 displays estimated ζ-factors of K lines plotted against the atomic number for different parameter optimizations concerning the thickness values for different take-off angles and the directly determined ζ-factors. The results are displayed together with the estimated ζ-factors where no thickness parameter was varied. Especially in the low energy region below 1 keV considerable differences of the ζ-factor values arose for the different parameter optimizations. In the case of the Super-X detector the ζ-factors fitting best to the experimentally determined ζ-values resulted from a take-off angle of 23° and not optimizing any thickness value which was confirmed by subsequent quantitative analyses. These ζ-factors of K lines are displayed in Figure 4.8 and listed in Table A.2.

Comparing the ζ-factors of the Super-X detector (see Figure 4.8 and Table A.2) to the ζ-factors of the Si(Li) detector (see Figure 4.4 and Table A.1) a difference in the magnitude of the values can be seen. The ζ-factors of the Super-X are between 140 and 1900 kg·electron/(m²·photon), whereas the ζ-factors of the Si(Li) are between 1300 and 7430 kg·electron/(m²·photon). This difference is attributed to the different high tensions; the ζ-factors of the Si(Li) detector were determined for a high voltage of 200 kV, whereas a high voltage of 300 kV was used in the case of the Super-X detector. Additionally, the different detection efficiencies of both systems (see chapters 2.2.3 and 2.3.1) influence the ζ-factors, which manifests in the magnitude of the ζ-factors. Due to the window of the Si(Li) detector the detection efficiency is significantly decreased in the low energy region thus increasing the ζ-factors for light elements.

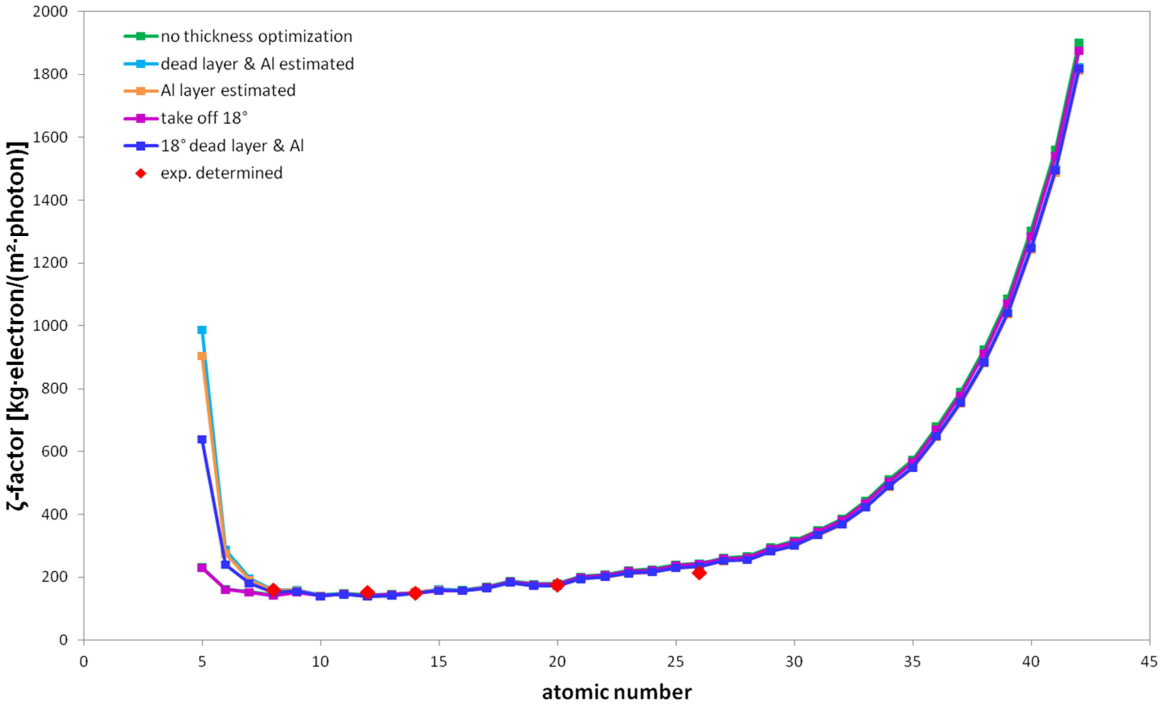

Figure 4.7: Estimated ζ-factors of K lines plotted against the atomic number for different parameter optimizations and the directly determined ζ-factors (red dots) of the Super-X detector.

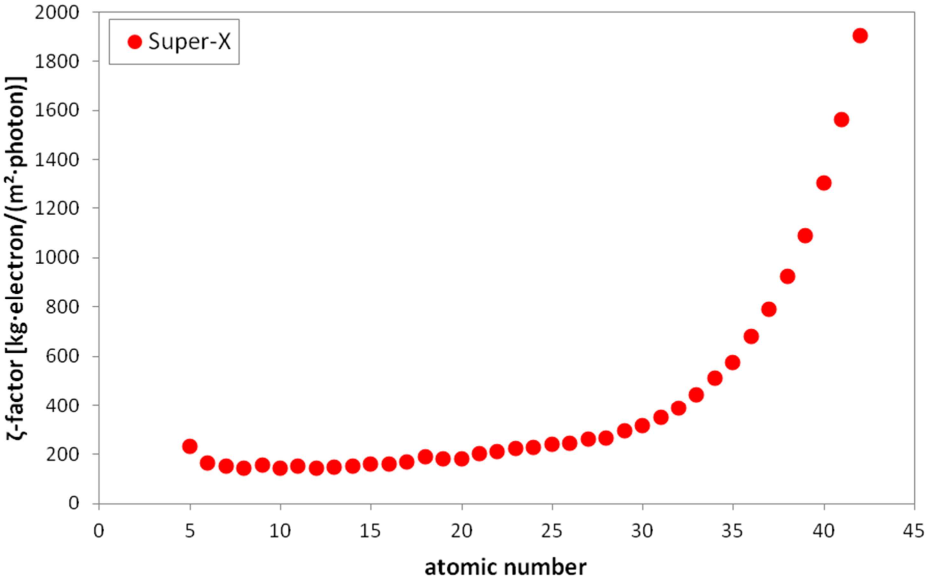

Figure 4.8: Estimated ζ-factors of K lines of the Super-X detector of Titan³ using the ionization cross-section of Paterson and no thickness optimization.

4.3 Application of ζ-factor method

With the knowledge of the ζ-factors for the individual TEM-EDXS systems quantitative EDXS analyses can now be performed using the ζ-factor method benefiting from its absorption correction thus yielding more accurate quantification results in particular regarding the quantification of light elements. Quantitative EDXS analysis of light elements is challenging as they have the disadvantage of fluorescence yield, poor detection efficiency and significant X-ray absorption. However, due to its ability to intrinsically correct for X-ray absorption the ζ-factor method significantly improved the quality of the quantitative analyses. Until now only a few applications of the ζ-factor method performing quantitative analyses were reported (Watanabe & Williams, 2006, Burke et al., 2006, Watanabe et al., 2006, Srot et al., 2010). In these publications materials like alloys, steels, ceramics, and metal oxides were quantified. To the best of our knowledge, no study was published until now on materials containing light elements like organic material, where the power of the ζ-factor method could be fully employed.

In this work the ζ-factor method was applied to EDX spectra of different materials, on the one hand to stable materials like sapphire and on the other hand to sensitive organic materials frequently used in organic semiconducting devices. The quantitative analyses were performed by a program of M. Watanabe called “zetact”, which performs an iterative process incorporating the absorption correction.

4.3.1 Sapphire

To test the validity of the obtained ζ-factors for both TEM-EDXS systems a sapphire (Al_2O_3) specimen (purchased by CrysTec Kristalltechnologie) was used, as sapphire is stable under the electron beam. The results for the Si(Li) detector were published in the paper of Fladischer and Grogger (Fladischer & Grogger, 2013). The sapphire specimen was prepared in the focused ion beam (FIB) instrument using the in situ lift-out technique (Langford & Clinton, 2004).

In the case of the Si(Li) detector EDX spectra of sapphire were acquired with a specimen tilt of 15° towards the detector, a beam current of 500 pA and an acquisition time of 100 s. In the case of the Super-X detector EDX spectra were acquired at a high tension of 300 kV, without any specimen tilt, a beam current of 930 pA and an acquisition time of 100 s. One representative EDX spectrum of each system is displayed in Figure 4.9. Again, the huge difference in detection efficiency is clearly visible when comparing both spectra.

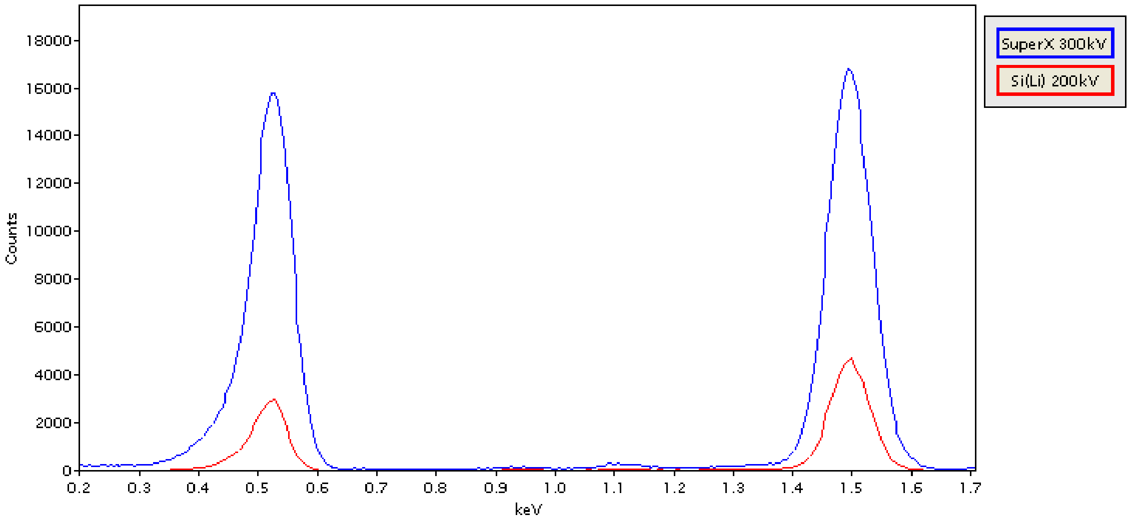

Figure 4.9: EDX spectra of sapphire acquired with the Si(Li) (red curve) and the Super-X detector (blue curve).

The results of the quantification of both TEM-EDXS systems can be seen together with the nominal composition of sapphire in Table 4.1. The error is estimated to be about 3% for the O/Al ratio resulting in the indicated error. The absorption-correction factors for the Si(Li) detector for O and Al were 1.25 and 1.06 for the chosen acquisition conditions. The absorption-correction factor is multiplied by the measured intensity to yield the generated (i.e. unabsorbed) X-ray intensity needed for quantification. Additionally, this factor indicates the error of quantitative analysis without performing absorption correction, which is in this case 25% for O and 6% for Al. In the case of the Super-X detector the absorption-correction factors for O and Al were 1.06 and 1.02 for the chosen acquisition conditions. In comparison to the Si(Li) detector the absorption-correction factors are very small, which is attributed to the windowless design of the Super-X detector. The results of the quantification of both systems are in good agreement with the nominal composition even for low energy X-ray lines.

Table 4.1: Results of quantitative EDXS analyses of the Si(Li) and the Super-X detector using the ζ-factor method for sapphire and its nominal composition (at%).

	Si(Li)		**Super-X**	
	O	**Al**	**O**	**Al**
Nominal	60.0	40.0	60.0	40.0
1	60.5	39.5	59.8	40.2
2	60.8	39.2	59.7	40.3
3	60.6	39.4	59.9	40.1
Mean	60.6 ± 0.5	39.4 ± 0.5	59.8 ± 0.3	40.2 ± 0.3

4.3.2 Organic semiconducting materials

The ζ-factor method was applied to quantitative EDXS analyses of organic semiconducting materials. The goal was the quantification of all organic materials used in the organic photodiode, being CuPc, PTCBi, Bphen and Alq_3 (see chapter 3.1). Therefore plan view specimens were prepared. Thus films of CuPc, PTCBi, Bphen and Alq_3 with a thickness of 40 nm were deposited on NaCl single crystals (Agar Scientific Ltd.) under high vacuum conditions (10^{-6} mbar) at room temperature in an organic material deposition chamber of a high-vacuum clustertool (Oerlikon Leybold Vacuum GmbH). The film thickness was measured with a quartz thickness gauge. To float off the organic layer, the sample was put into a vessel with distilled water, where the NaCl single crystal dissolved, and the organic layer was transferred to a TEM supporting grid. Unfortunately Alq_3 dissolved completely in the distilled water due to hydrolysis (Knox et al., 2006). Thus the plan view specimens of CuPc, PTCBi and Bphen were investigated in the Tecnai F20.

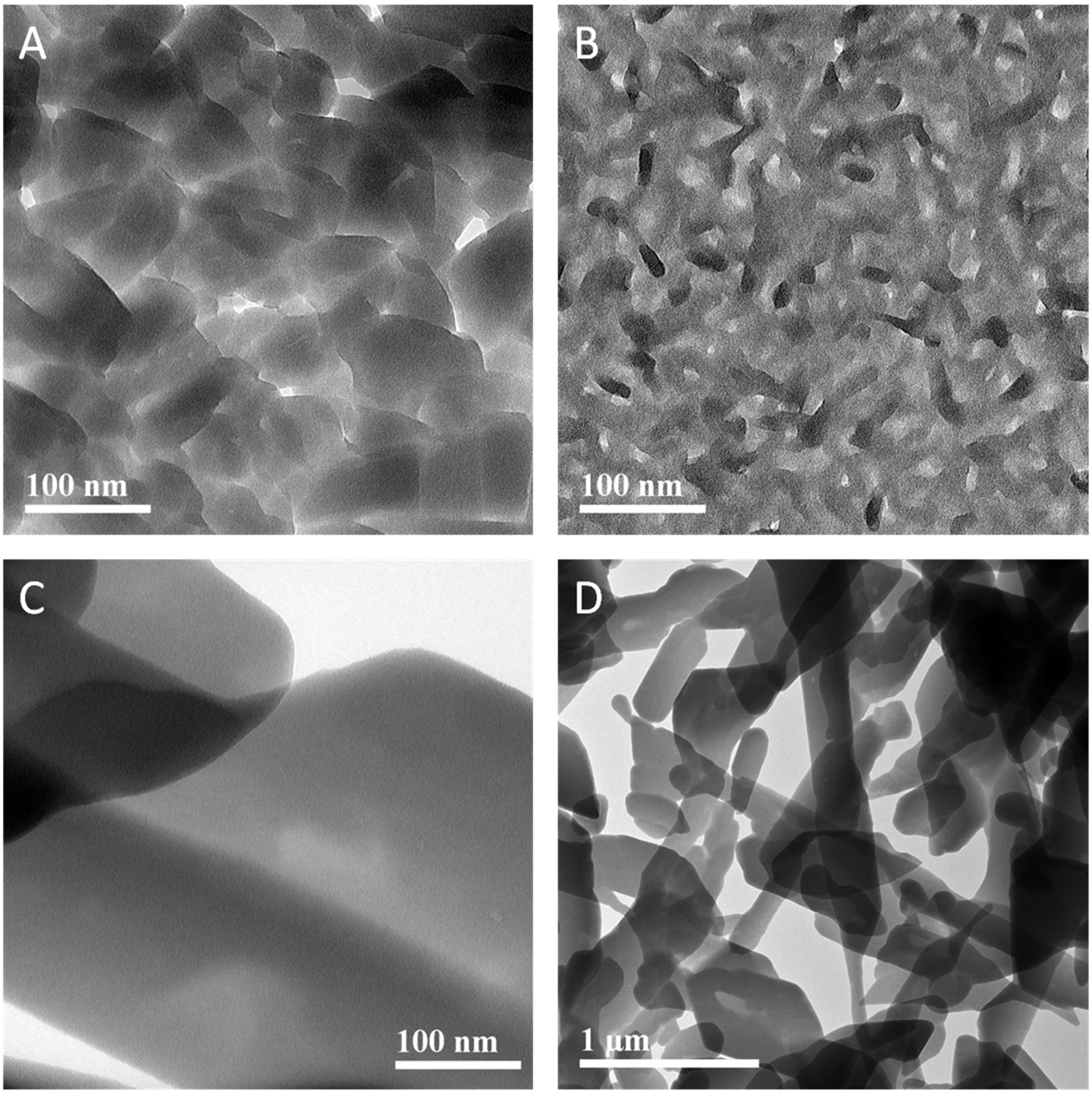

Figure 4.10: TEM BF ZL filtered images of A) CuPc, B) PTCBi and C,D) Bphen.

In Figure 4.10 TEM BF ZL filtered images of plan view specimens of CuPc (A), PTCBi (B) and Bphen (C and D) are shown. The organic materials are dispayed at the same magnification in Figures A – C. Additionally Bphen is shown in a smaller magnification in Figure D due to its shape dimensions. The morphological difference is obvious when comparing the images. While CuPc forms shapes with diameters varying between 40 and 100 nm, PTCBi is growing in rod-like structures with diameters of the rods of 10 nm, whereas Bphen builds rods with diameters varying between 100 and 500 nm.

A crucial point in TEM investigations is the stability of the specimen during exposure to the electron beam. Especially organic materials are very sensitive and degradation will likely take place sooner or later. The stability of CuPc, PTCBi and Bphen was determined by exposing the materials to the same illumination conditions in TEM diffraction mode (image coupling) and acquiring the EELS signal for the C K edge of exactly the same specimen area with advancing time. In all three cases a beam current of 400 pA was used. In Figure 4.11 the EEL spectra of the C and N edge (energy range: 280 – 430 eV) and the intensity of the C edge are displayed for CuPc, PTCBi and Bphen as a function of time. In this illustration the background of the C edge of each EEL spectrum was removed and resulting EEL spectra are displayed together in Figure 4.11. It can be seen that under the given illumination conditions CuPc is stable for up to 500 s while PTCBi starts to degrade after 130 s, whereas Bphen starts to degrade immediately. Due to the immediate degradation of Bphen, this material was excluded for quantitative EDXS investigations. The results of the quantitative EDXS analyses of CuPc and PTCBi are published in the paper of Fladischer and Grogger (Fladischer & Grogger, 2013).

Based on these EELS data the acquisition parameters for consecutive EDXS measurements for CuPc and PTCBi were chosen such that the materials did not degrade. Therefore STEM illumination and continuous scanning of the analyzed region during EDXS acquisition was chosen, as for STEM illumination the characteristic dose is reported to increase by several orders of magnitude thus decreasing beam damage significantly in comparison to TEM illumination (Varlot et al., 1997, Egerton & Rauf, 1999).

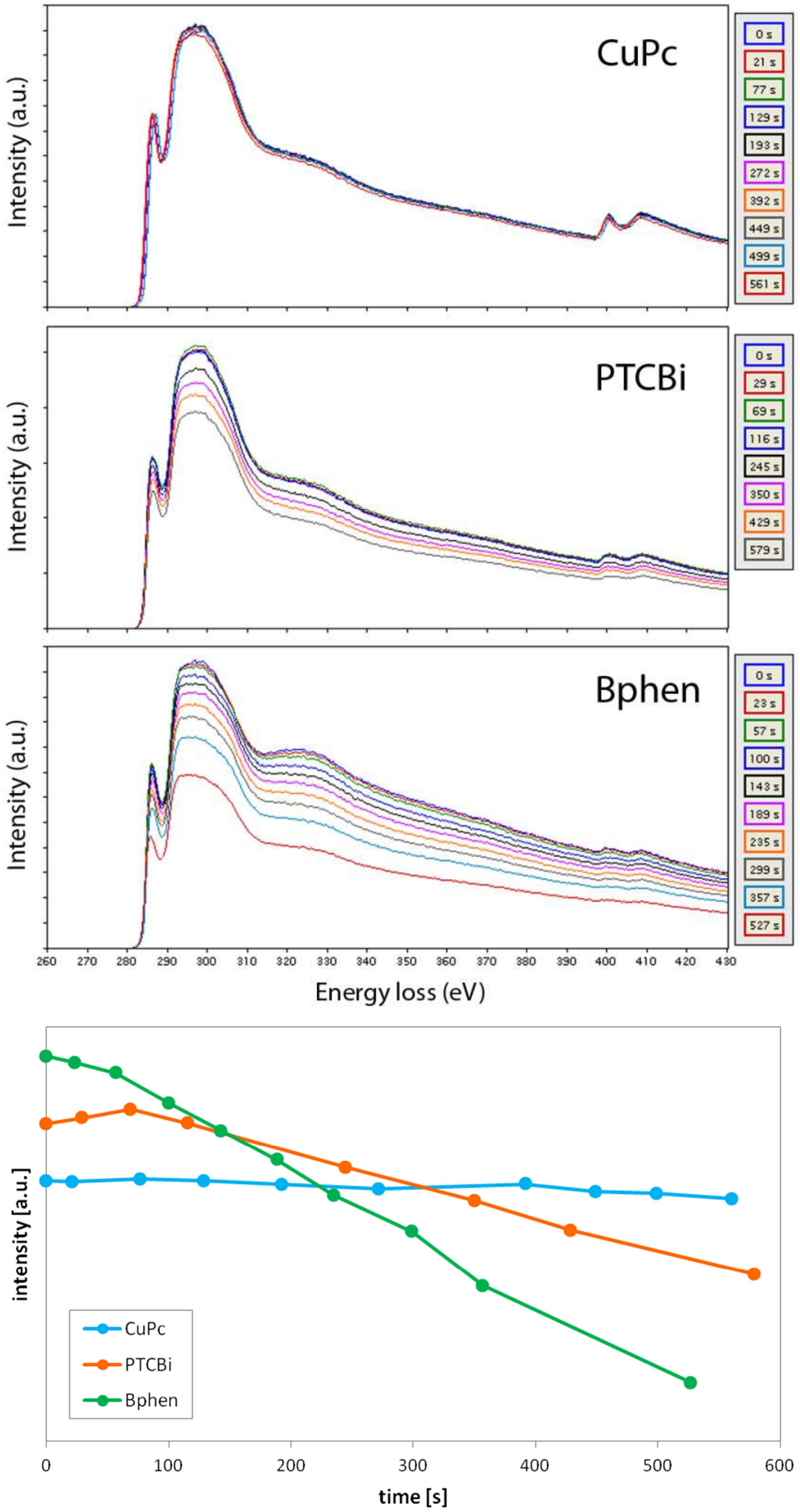

Figure 4.11: EEL spectra and intensity of the C edge of CuPc, PTCBi and Bphen as a function of time.

For the acquisition of the EDX spectra both specimens were again tilted to 15° towards the Si(Li) detector of Tecnai F20. In the case of CuPc a beam current of 410 pA was set and a specimen area of 0.49 µm² was scanned during the acquisition. One of several EDX spectra of CuPc, which were acquired at different specimen areas, is depicted in Figure 4.12. The quantitative analysis was performed by using the K lines of the elements C, N and Cu. Note that the composition of CuPc is $C_{32}H_{16}CuN_8$ and hydrogen can't be detected by EDXS. As a consequence the following quantification results are given in concentration ratios. In Table 4.2 the results of the quantification using the ζ-factor method, the mean value and its standard deviation are listed together with the nominal composition. Spectrum 1 was acquired with an acquisition time of 100 s, whereas spectra 2 and 3 were acquired for 300 s. The absorption-correction factors for C, N and Cu were 1.19, 1.92 and 1.00 for the CuPc specimen and the chosen acquisition conditions. The results for this organic material comprising light elements (C and N) and metal atoms (Cu) are in good agreement with each other and the nominal composition.

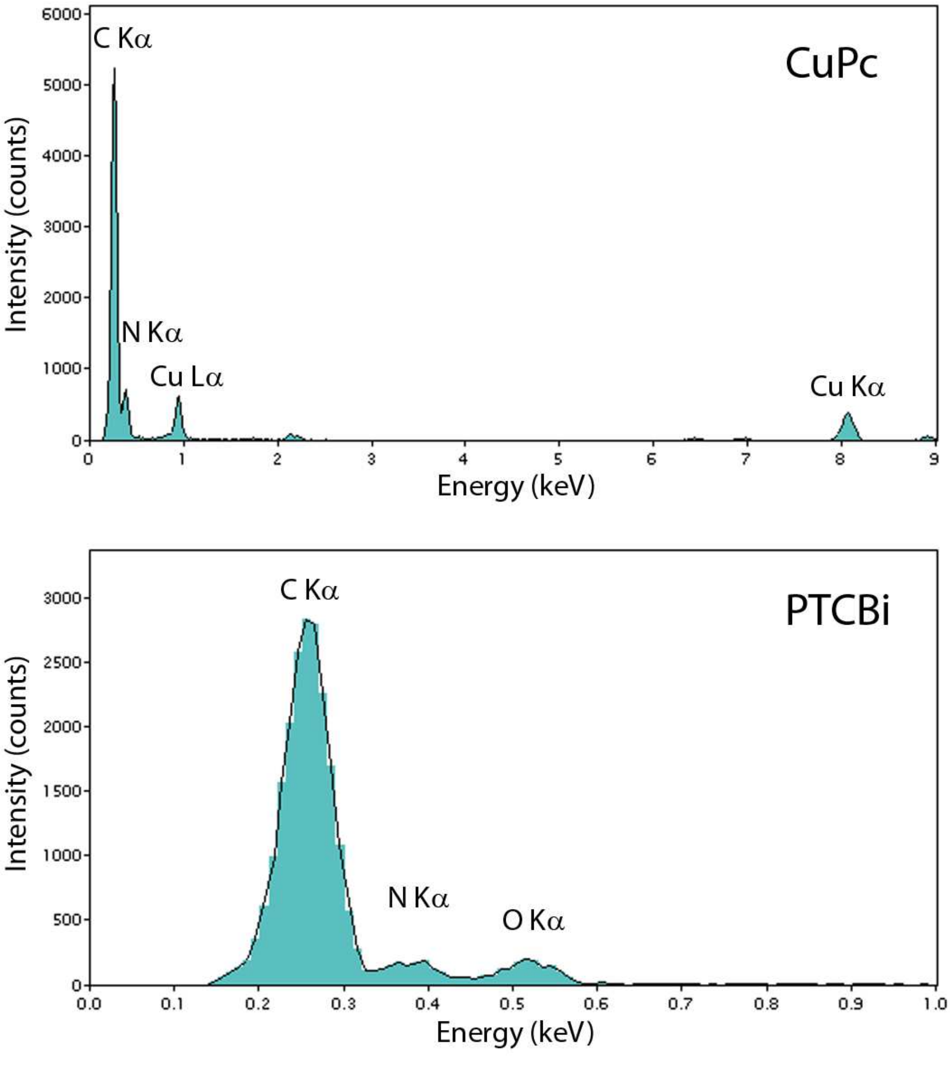

Figure 4.12: EDX spectra of CuPc and PTCBi. (Fladischer & Grogger, 2013)

In the case of PTCBi a beam current of 380 pA was chosen while scanning over a specimen area of 1 µm². Spectra 1 and 2 were acquired for 100 s and spectrum 3 for 200 s. Comparing these acquisition parameters to those of CuPc, a lower beam current, bigger specimen areas and shorter acquisition times were chosen for this more sensitive specimen. An EDX spectrum of PTCBi is displayed in Figure 4.12, where the C K, N K and O K peak is shown. The composition of PTCBi is $C_{36}H_{16}N_4O_2$ and for same reasons as mentioned above, a relative composition omitting hydrogen is used to compare the experimental results. In Table 4.2 the results of the quantitative analysis of PTCBi, consisting of only light elements, are listed together with the mean value, its standard deviation and the nominal values. The absorption-correction factors for C, N and O were 1.05, 1.44 and 1.24 for the PTCBi specimen and the chosen acquisition conditions. Again a very good agreement is obvious when comparing the values with each other and the nominal composition.

Table 4.2: Concentration ratios of quantitative EDXS analyses using the ζ-factor method for CuPc and PTCBi and their nominal concentration ratios (at%). (Fladischer & Grogger, 2013)

	CuPc		**PTCBi**	
	N/C	**Cu/C**	**N/C**	**O/C**
Nominal	0.250	0.031	0.111	0.056
1	0.256	0.034	0.100	0.063
2	0.233	0.033	0.110	0.067
3	0.215	0.031	0.099	0.056
Mean	0.235 ± 0.021	0.032 ± 0.002	0.103 ± 0.006	0.062 ± 0.005

The ζ-factor method with its built-in absorption correction was used for quantitative analyses of different materials comprising light elements. The results are in good agreement with the nominal compositions for these well-defined materials and the deviations of the results are within the error limits. The quantification using EDXS would not have been possible without the proper absorption correction of the ζ-factor method (see calculated absorption factors).

5 Conclusion and Outlook

In this work, TEM and its analytical methods in particular EDXS were used to characterize organic semiconducting devices.

First, the performances of the two TEM-EDXS systems used for this work were determined as this knowledge is indispensable to perform reliable EDXS analysis. Thus the Tecnai F20 with a Si(Li) detector and the Titan³ with a Super-X detector were characterized concerning their detection efficiency, detection sensitivity, energy resolution, stray radiation, geometrical aspects like solid angle and take-off angle as well as absorption effects caused by geometrical conditions. All these issues could be clarified for both TEM-EDXS systems by measuring and analyzing different standard specimens. It could be shown that the detection efficiency of the Super-X detector is significantly higher than that of the Si(Li) detector which is attributed to the substantially bigger solid angle. Additionally, the windowless design of the Super-X detector increases the detection efficiency for low energies in comparison to the Si(Li) detector which is equipped with an ultrathin polymer window. As a consequence of the improved detection efficiency of the Super-X detector its detection sensitivity is significantly higher and trace elements can be detected in much shorter times and with better statistics. Due to its improved electronics and SDD detector design the Super-X detector shows significantly better energy resolution when comparing small time constants. Characteristic X-ray peaks caused by stray radiation were identified for both systems thus preventing their wrong assignment to the specimen. The Super-X detector has the advantage that due to its geometry there is no need of tilting the specimen. However, the fact that the quadrants are placed symmetrically around the specimen has to be considered carefully concerning absorption effects caused by the geometry of the specimen. Thus only appropriate quadrants ensure reliable EDXS analysis. Altogether these characterizations enable correct interpretation and analysis of acquired EDX spectra of unknown specimens.

The two TEM systems were then used to characterize different aspects of an organic photodiode, which is used as a detection unit in an organic opto-chemical sensor. In this work special ring-shaped organic photodiodes were characterized with regard to the appearance of the different interfaces and the thicknesses of the individual layers. Furthermore, material diffusion and the influence of different organic blocking layers introduced into device structures in combination with different deposition techniques of metal electrodes were studied. To elucidate these parameters influencing the device performance different investigation methods such as TEM, SEM, AFM and X-ray scattering techniques were used.

For TEM investigations the first requirement is the preparation of the specimen which needs to be representative of the whole sample and free of artifacts. Therefore several attempts were made using ultramicrotomy and the FIB instrument with the result that reliable cross-section lamellas of the OPDs can be prepared in the FIB using the in-situ lift out technique in combination with upside down milling and low ion beam currents. TEM investigations of organic devices are challenging due to the sensitivity of organic materials to beam damage and contamination. An additional challenge posed the Ag electrode of the OPD as it alters in ambient air. Despite these challenges reliable TEM results could be obtained by (i) performing the TEM investigation immediately after the preparation in the FIB, (ii) working with a clean specimen holder and a good vacuum and (iii) using low dose rates for the TEM investigations. As the organic layers of the OPD exhibit similar mass-thicknesses for the cross-section lamellas they are not distinguishable with imaging techniques in TEM. Thus the different layers of the OPD were identified and distinguished by the combination of analytical methods as EDXS, EELS and EFTEM and their thicknesses were measured. The TEM results in combination with SEM, AFM and XRR measurements could elucidate the topography and roughness of the interfaces as well as the thicknesses of the individual layers. It could be shown that the semitransparent Au layer is very smooth. A significantly increased surface roughness is observed for CuPc, which is attributed to its crystallinity. PTCBi grows with randomly distributed crystallites resulting in similar roughness values. The deposition of amorphous Alq_3 flattens the surface whereas the top Ag cathode again exhibits a rough surface. Thus the roughness increases with each layer except for amorphous Alq_3, which smoothes the surface a little bit. The rough interfaces between the organic materials result in smooth transitions of the analytical data in the TEM cross-section investigations.

In further investigations the diffusion of Ag into different organic materials was investigated with respect to different Ag deposition techniques such as electron beam deposition, ion beam sputtering and vacuum thermal evaporation at various deposition rates. No Ag diffusion was detected in the case of crystalline Bphen, whereas Ag diffusion of varying extent was observed for amorphous Alq_3, which depends on both the deposition technique and the deposition rate. It was demonstrated that the Ag diffusion essentially depends on the structural properties of the subjacent organic material and that diffusion, in turn, can be minimized by choosing appropriate materials, deposition techniques and preparation parameters. Both the deposition technique used for the metallic layer and the nature of the organic blocking layer material itself significantly impact the performance of organic semiconducting devices. Clearly, to optimize the device performance, an appropriate deposition parameter set needs to be found for each individual material stack. In the present case of OPDs, the most reliable production strategy consists of using Bphen in combination with Ag deposited by vacuum thermal evaporation with the lowermost deposition rate.

As the results of our different investigation methods such as TEM, SEM, AFM as well as XRR are both qualitatively and quantitatively in good agreement and, hence, corroborate each other it could be shown that the combination of investigation methods used in this work represents a powerful nanoanalytical toolset perfectly suited for the characterization of organic electronic devices.

The final chapter of this work deals with the ζ-factor method which was used to perform quantitative X-ray analysis. With its ability to intrinsically correct for X-ray absorption, the ζ-factor method significantly improved the quality of the quantification as well as the accuracy of the results in particular regarding the quantification of light elements. The sensitivity factors (ζ-factors) for both TEM-EDXS systems were determined experimentally using a standard specimen. Based on these factors a series of ζ-factors covering a significant fraction of the periodic table was estimated by careful study of all parameters thus enabling the quantification of a multitude of elements. The determined ζ-factors were then used for quantitative analyses of stable materials like sapphire and sensitive organic semiconducting materials used in the above mentioned OPD. The quantitative results of these materials consisting of either light elements exclusively or in combination with metal atoms are in good agreement with their nominal compositions. This good agreement is attributed to the absorption correction of the ζ-factor method determining the mass thickness of each analyzed region. The necessity of performing this absorption correction is demonstrated by the values of the absorption-correction factors for light elements. Thus the accuracy of the quantitative analysis and the good performance of the ζ-factor method could be confirmed.

The ζ-factor method is established at both TEM-EDXS systems for K lines and special focus was put on the quantitative analysis of light elements. Thus the next step should be the determination of ζ-factor for L and M lines, which then will provide a powerful tool for the quantitative analysis of all kinds of specimens containing light as well as heavy elements.

6 Bibliography

Allen, S.M., 1981. Foil thickness measurements from convergent-beam diffraction patterns. Philos. Mag. A 43, 325-335.

Armigliato, A., 1992. X-ray microanalysis in the analytical electron microscopy. Electron Microscopy in Materials Science, 431-456.

Bambynek, W., 1989. A new evaluation of K-shell fluorescence yields. Post deadline paper of X84 Proceedings X-ray and Inner-Shell Processes in Atoms, Molecules and Solids (ed. by A. Meisel) , 20-23.

Barbiellini, G., Bologna, G., Diambrini, G., Murtas, G.P., 1962. Experimental evidence for a quasi-monochromatic bremsstrahlung intensity from the Frascati 1-GeV electronsynchrotron. Phys. Rev. Lett. 8, 454-457.

Bennett, H.E., Peck, R.L., Burge, D.K., Bennett, J.M., 1969. Formation and growth of tarnish on evaporated silver films. J. Appl. Phys. 40, 3351-3360.

Bennett, J.C., Egerton, R.F., 1995. NiO Test Specimens for Analytical Electron Microscopy: Round-Robin Results. Microscopy and Microanalysis 1, 143.

Bethe, H., 1930. Zur Theorie des Durchgangs schneller Korpuskularstrahlen durch Materie. Ann.Phys.(Leipzig) 5, 325-400.

Bonnet, N., Colliex, C., Mory, C., Tence, M., 1988. Developments in processing image sequences for elemental mapping. Scanning microscopy.Supplement 2, 351-364.

Brabec, C.J., Sariciftci, N.S., Hummelen, J.C., 2001. Plastic solar cells. Advanced Funtional Materials 11, 15-26.

Brown, D.B., 1974. Cross sections for ionization of K- and L-shells by electrons. Handbook of Spectroscopy 1, 248.

Burke, M.G., Watanabe, M., Williams, D.B., Hyde, J.M., 2006. Quantitative characterization of nanoprecipitates in irradiated low-alloy steels: Advances in the application of FEG-STEM quantitative microanalysis to real materials. J. Mater. Sci. 41, 4512-4522.

Burroughes, J.H., Bradley, D.D.C., Brown, A.R., Marks, R.N., Mackay, K., Friend, R.H., Burns, P.L., Holmes, A.B., 1990. Light-emitting diodes based on conjugated polymers. Nature 347, 539-541.

Cliff, G., Lorimer, G.W., 1975. The quantitative analysis of thin specimens. J. Microsc. 103, 203-207.

Deslattes, R.D., Kessler Jr., E.G., Indelicato, P., de Billy, L., Lindroth, E., Anton, J., 2003. X-ray transition energies: new approach to a comprehensive evaluation. Rev.Mod.Phys. 75.

Dimitrakopoulos, C.D., Malenfant, P.R.L., 2002. Organic thin film transistors for large area electronics. Adv Mater 14, 99-117.

Dürr, A.C., Schreiber, F., Kelsch, M., Carstanjen, H.D., Dosch, H., Seeck, O.H., 2003. Morphology and interdiffusion behavior of evaporated metal films on crystalline diindenoperylene thin films. J. Appl. Phys. 93, 5201-5209.

Egerton, R.F., 2012. Control of radiation damage in the TEM. Ultramicroscopy.

Egerton, R.F., 1996. Electron energy-loss spectroscopy in the electron microscope, 2nd edition. Plenum Press, New York.

Egerton, R.F., Cheng, S.C., 1994. Characterization of an analytical electron microscope with a NiO test specimen. Ultramicroscopy 55, 43-54.

Egerton, R.F., Li, P., Malac, M., 2004. Radiation damage in the TEM and SEM. Micron 35, 399-409.

Egerton, R.F., Rauf, I., 1999. Dose-rate dependence of electron-induced mass loss from organic specimens. Ultramicroscopy 80, 247-254.

Eibl, O., 1993. New method for absorption correction in high-accuracy, quantitative EDX microanalysis in the TEM including low-energy X-ray lines. Ultramicroscopy 50, 179-188.

Faupel, F., Willecke, R., Thran, A., 1998. Diffusion of metals in polymers. Materials Science and Engineering R: Reports 22, 1-55.

Fiori, C.E., Swyt, C.R., Myklebust, R.L., 1992. NIST/NIH Desk Top Spectrum Analyzer. available from the National Institute of Standards and Technology .

Fladischer, S., 2009. New Methods of Quantitative X-Ray Analysis in a Transmission Electron Miroscope. Diploma Thesis.

Fladischer, S., Grogger, W., 2013. Quantitative EDXS analysis of organic materials using the ζ-factor method. Submitted to Ultramicroscopy.

Fladischer, S., Neuhold, A., Kraker, E., Haber, T., Lamprecht, B., Salzmann, I., Resel, R., Grogger, W., 2012. Diffusion of Ag into organic semiconducting materials: A combined analytical study using transmission electron microscopy and X-ray reflectivity. ACS Applied Materials and Interfaces 4, 5608-5612.

Freitag, B., 2013. private communication.

Friend, R.H., Gymer, R.W., Holmes, A.B., Burroughes, J.H., Marks, R.N., Taliani, C., Bradley, D.D.C., Dos Santos, D.A., Brédas, J.L., Lögdlund, M., Salaneck, W.R., 1999. Electroluminescence in conjugated polymers. Nature 397, 121-128.

Gautier, E., Lorin, A., Nunzi, J.-., Schalchli, A., Benattar, J.-., Vital, D., 1996. Electrode interface effects on indium-tin-oxide polymer/metal light emitting diodes. Appl. Phys. Lett. 69, 1071-1073.

Goldstein, J.I., Costley, J.L., Lorimer, G.W., Reed, S.J.B., 1977. Quantitative X-ray analysis in the electron microscope. Scan. Electron Microsc. 1, 315-324.

Grandin, H.M., Tadayyon, S.M., Lennard, W.N., Griffiths, K., Coatsworth, L.L., Norton, P.R., Popovic, Z.D., Aziz, H., Hu, N.X., 2003. Rutherford backscattering and secondary ion mass spectrometry investigation of Mg:Ag-tris(8-hydroxy quinoline) aluminum interfaces. Organic Electronics: physics, materials, applications 4, 9-14.

Green, M., Cosslett, V.E., 1961. The efficiency of production of characteristic x-radiation in thick targets of a pure element. Proc. Phys. Soc. 78, 1206-1214.

Heinrich, K.F.J., 1987. Mass absorption coefficients for electron probe microanalysis. Proceedings of the 11th International Congress on X-ray Optics and Microanalysis (ed. By J.D. Brown and R.H. Packwood), 67-377.

Hirose, Y., Kahn, A., Aristov, V., Soukiassian, P., Bulovic, V., Forrest, S.R., 1996. Chemistry and electronic properties of metal-organic semiconductor interfaces: Al, Ti, In, Sn, Ag, and Au on PTCDA. Physical Review B - Condensed Matter and Materials Physics 54, 13748-13758.

Horita, Z., Ichitani, K., Sano, T., Nemoto, M., 1989. Applicability of the differential X-ray absorption method to the determinations of foil thickness and local composition in the analytical electron micrscope. Philosophical Magazine A: Physics of Condensed Matter, Structure, Defects and Mechanical Properties 59, 939-952.

Horita, Z., Sano, T., Nemoto, M., 1987. Simplification of X-ray absorption correction in thin-sample quantitative microanalysis. Ultramicroscopy 21, 271-276.

Huang, Q., Walzer, K., Pfeiffer, M., Leo, K., Hofmann, M., Stübinger, T., 2006. Performance improvement of top-emitting organic light-emitting diodes by an organic capping layer: An experimental study. J. Appl. Phys. 100, 064507.

Jakoby, C., Genz, H., Richter, A., 1987. A semi-empirical, formula for the total K-shell ionization cross section by electron impact. J. Phys. Colloques 48 (C9), 487-490.

Kelly, P.M., Jostsons, A., Blake, R.G., Napier, J.G., 1975. Determination of foil thickness by scanning transmission electron microscopy. Phys Status Solidi (A) Appl Res 31, 771-780.

Klauk, H., 2010. Organic thin-film transistors. Chem. Soc. Rev. 39, 2643-2666.

Knox, J.E., Halls, M.D., Hratchian, H.P., Schlegel, H.B., 2006. Chemical failure modes of AlQ3-based OLEDs: AlQ3 hydrolysis. Physical Chemistry Chemical Physics 8, 1371-1377.

Kraker, E., Haase, A., Lamprecht, B., Jakopic, G., Konrad, C., Köstler, S., 2008. Integrated organic electronic based optochemical sensors using polarization filters. Appl. Phys. Lett. 92.

Kramers, H.A., 1923. On the Theory of X-ray Absorption and Continuous X-ray Spectrum. Phil. Mag. 46, 836.

Lamprecht, B., Abel, T., Kraker, E., Haase, A., Konrad, C., Tscherner, M., Köstler, S., Ditlbacher, H., Mayr, T., 2010. Integrated fluorescence sensor based on ring-shaped organic photodiodes. Physica Status Solidi - Rapid Research Letters 4, 157-159.

Lamprecht, B., Kraker, E., Sagmeister, M., Köstler, S., Galler, N., Ditlbacher, H., Ungerböck, B., Abel, T., Mayr, T., 2011. Integrated waveguide sensor utilizing organic photodiodes. Physica Status Solidi - Rapid Research Letters 5, 344-346.

Langford, R.M., Clinton, C., 2004. In situ lift-out using a FIB-SEM system. Micron 35, 607-611.

Lechner, P., Eckbauer, S., Hartmann, R., Krisch, S., Hauff, D., Richter, R., Soltau, H., Strüder, L., Fiorini, C., Gatti, E., Longoni, A., Sampietro, M., 1996. Silicon drift detectors for high resolution room temperature X-ray spectroscopy. Nuclear Instruments and Methods in Physics Research, Section A: Accelerators, Spectrometers, Detectors and Associated Equipment 377, 346-351.

Li, H., Brédas, J.-., Lennartz, C., 2007. First-principles theoretical investigation of the electronic couplings in single crystals of phenanthroline-based organic semiconductors. J. Chem. Phys. 126.

Lifshin, E., Ciccarelli, M.F., Bolon, R.B., 1975. Practical Scanning Electron Microscopy. ed. J.I. Goldstein, H. Yakowitz, Plenum Press, New York , 363-398.

Maher, D.M., Joy, D.C., Ellington, M.B., Zaluzec, N.J., Mochel, P.E., 1981. Relative accuracy of k-factor calculations for thin film X-ray analysis. Analytical Electron Microscopy 1981 , 33-38.

McDonagh, C., Burke, C.S., MacCraith, B.D., 2008. Optical chemical sensors. Chem. Rev. 108, 400-422.

Mitterbauer, C., 2011. private communication.

Morris, P.L., Ball, M.D., Statham, P.J., 1980. The correction of thin foil microanalysis data for X-ray absorption effect. Developments in Electron Microscopy and Analysis (ed. by T. Mulvey) , 413-416.

Mott, N.F., Massey, H.S.W., 1949. The Theory of Atomic Collisions. Second Edition.

Neuhold, A., Fladischer, S., Mitsche, S., Flesch, H.-., Moser, A., Novak, J., Smilgies, D.M., Kraker, E., Lamprecht, B., Haase, A., Grogger, W., Resel, R., 2011. Structure and morphology of an organic/inorganic multilayer stack: An x-ray reflectivity study. J. Appl. Phys. 110.

Newbury, D.E., Williams, D.B., Goldstein, J.I., Fiori, C.E., 1984. Observation on the calculation of kAB factors for analytical electron microscopy. Analytical Electron Microscopy - 1984 , 276-278.

Nicolosi, J., 2008. private communication.

Pais, A., Banerjee, A., Klotzkin, D., Papautsky, I., 2008. High-sensitivity, disposable lab-on-a-chip with thin-film organic electronics for fluorescence detection. Lab on a Chip - Miniaturisation for Chemistry and Biology 8, 794-800.

Pantel, R., 2011. Coherent Bremsstrahlung effect observed during STEM analysis of dopant distribution in silicon devices using large area silicon drift EDX detectors and high brightness electron source. Ultramicroscopy 111, 1607-1618.

Paterson, J.H., Chapman, J.N., Nicholson, W.A.P., Titchmarsh, J.M., 1989. Characteristic X-ray production cross-sections for standardless elemental analysis in EDX. J. Microsc. 154, 1-17.

Peumans, P., Yakimov, A., Forrest, S.R., 2003. Small molecular weight organic thin-film photodetectors and solar cells. J. Appl. Phys. 93, 3693-3723.

Philibert, J., 1963. A method for calculating the absorption correction in electron probe microanalysis. Proc 3rd Int.Symp.X-ray Optics and Microanalysis , 379-392.

Powell, C.J., 1976. Cross sections for ionization of inner-shell electrons by electrons. Reviews of Modern Physics 48, 33-47.

Reed, W.P., 1993. Certificate of Analysis Standard Reference Material 2063a. National Institute of Standards and Technology , 1-2.

Reed, W.P., 1992. Certificate of Analysis Standard Reference Materials 610 and 611. National Institute of Standards and Technology , 1-3.

Reese, G.M., Spence, J.C.H., Yamamoto, N., 1984. Coherent Bremsstrahlung from kilovolt electrons in zone axis orientations. Philosophical Magazine A: Physics of Condensed Matter, Structure, Defects and Mechanical Properties 49, 697-716.

Savvate'ev, V., Chen-Esterlit, Z., Aylott, J.W., Choudhury, B., Kim, C.-., Zou, L., Friedl, J.H., Shinar, R., Shinar, J., Kopelman, R., 2002. Integrated organic light-emitting device/fluorescence-based chemical sensors. Appl. Phys. Lett. 81, 4652-4654.

Scharnberg, M., Hu, J., Kanzow, J., Rätzke, K., Adelung, R., Faupel, F., Pannemann, C., Hilleringmann, U., Meyer, S., Pflaum, J., 2005. Radiotracer measurements as a sensitive tool for the detection of metal penetration in molecular-based organic electronics. Appl. Phys. Lett. 86, 024104-1-024104-3.

Schlossmacher, P., Klenov, D.O., Freitag, B., von Harrach, H.S., 2010a. Enhanced Detection Sensitivity with a New Windowless XEDS System for AEM Based on Silicon Drift Detector Technology. Microscopy Today 18, 14.

Schlossmacher, P., Klenov, D.O., Freitag, B., von Harrach, H.S., Steinbach, A., 2010b. Nanoscale Chemical Compositional Analysis with an Innovative S/TEM-EDX System. Microscopy and Analysis 24, 5-8.

Scholze, F., Procop, M., 2009. Modelling the response function of energy dispersive X-ray spectrometers with silicon detectors. X-Ray Spectrom. 38, 312-321.

Schreiber, T.P., Wims, A.M., 1981. A quantitative X-ray microanalysis thin film method using K-, L-, and M-lines. Ultramicroscopy 6, 323-334.

Sheridan, P.J., 1989. Determination of experimental and theoretical kASi factors for a 200-kV analytical electron microscope. J. Electron Microsc. Tech. ; J. Electron Microsc. Tech. 11, 41-61.

Song, Q.L., Li, F.Y., Yang, H., Wu, H.R., Wang, X.Z., Zhou, W., Zhao, J.M., Ding, X.M., Huang, C.H., Hou, X.Y., 2005. Small-molecule organic solar cells with improved stability. Chemical Physics Letters 416, 42-46.

Song, W., Li, Z., So, S.K., Qiu, Y., Zhu, Y., Cao, L., 2001a. Dynamic SIMS characterization of interface structure of Ag/Alq3/NPB/ITO model devices. Surf. Interface Anal. 32, 102-105.

Song, W., So, S.K., Moulder, J., Qiu, Y., Zhu, Y., Cao, L., 2001b. Study on the interaction between Ag and tris(8-hydroxyquinoline) aluminum using x-ray photoelectron spectroscopy. Surf. Interface Anal. 32, 70-73.

Spence, J.C.H., Reese, G., Yamamoto, N., Kurizki, G., 1983. Coherent Bremsstrahlung Peaks in X-ray Microanalysis Spectra. Philosophical Magazine B: Physics of Condensed Matter; Electronic, Optical and Magnetic Properties 48, l39-l43.

Srot, V., Watanabe, M., Scheu, C., Van Aken, P.A., Salzberger, U., Luerßen, B., Janek, J., Rühle, M., 2010. Characterization of chemical composition and electronic structure of Pt/YSZ interfaces by analytical transmission electron microscopy. Solid State Ionics 181, 1616-1622.

Strunskus, T., Kiene, M., Willecke, R., Thran, A., Bechtolsheim, C.V., Faupel, F., 1998. Chemistry, diffusion and cluster formation at metal-polymer interfaces. Materials and Corrosion - Werkstoffe und Korrosion 49, 180-188.

Tang, C.W., 1986. Two-layer organic photovoltaic cell. Appl. Phys. Lett. 48, 183-185.

Ted Pella, I., 2011. Evaluating an Analytical TEM with the NIOX^{TM}Test Specimen Product No. 650. Technical Notes.

Turak, A., Grozea, D., Feng, X.D., Lu, Z.H., Aziz, H., Hor, A.M., 2002. Metal/AlQ 3 interface structures. Appl. Phys. Lett. 81, 766-768.

Van Cappellen, E., 1990. The parameterless correction method in X-ray microanalysis. Microsc.Microanal.Microstruct. 1, 1-22.

Varlot, K., Martin, J.M., Quet, C., Kihn, Y., 1997. Towards sub-nanometer scale EELS analysis of polymers in the TEM. Ultramicroscopy 68, 123-133.

Wang, X.Z., Xie, Z.T., Wang, X.J., Zhou, Y.C., Zhang, W.H., Ding, X.M., Hou, X.Y., 2007. Blocking of interfacial diffusion at Ag/Alq3 by LiF. Appl. Surf. Sci. 253, 3930-3932.

Watanabe, M., 2009. XUtils Plug-in for Gatan DigitalMicrograph.

Watanabe, M., Ackland, D.W., Burrows, A., Kiely, C.J., Williams, D.B., Krivanek, O.L., Dellby, N., Murfitt, M.F., Szilagyi, Z., 2006. Improvements in the X-ray analytical capabilities of a scanning transmission electron microscope by spherical-aberration correction. Microsc. Microanal. 12, 515-526.

Watanabe, M., Horita, Z., Nemoto, M., 1996. Absorption correction and thickness determination using the ζ factor in quantitative X-ray microanalysis. Ultramicroscopy; Ultramicroscopy 65, 187-198.

Watanabe, M., Williams, D.B., 2006. The quantitative analysis of thin specimens: A review of progress from the Cliff-Lorimer to the new ζ-factor methods. J. Microsc. 221, 89-109.

Watanabe, M., Williams, D.B., 2003. Quantification of elemental segregation to lath and grain boundaries in low-alloy steel by STEM X-ray mapping combined with the ζ-factor method. Z Metallkd 94, 307-316.

Watanabe, M., Williams, D.B., 1999. The new form of the zeta-factor method for quantitative microanalysis in AEM-XEDS and its evaluation. Microsc. Microanal. 5, 88-89.

Wentzel, G., 1927. Über strahlungslose Quantensprünge. Zeitschrift für Physik 43, 524-530.

West, R., 2008. private communication.

Williams, D.B., Carter, C.B., 1996. Transmission Electron Microscopy: A Textbook for Materials Science. In Plenum Press N. Y. (Ed.).

Williams, E.J., 1933. Applications of the method of of impact parameter in collisions. Proc. R. Soc. [A] 139, 163-186.

Wolfbeis, O.S., 2005. Materials for fluorescence-based optical chemical sensors. Journal of Materials Chemistry 15, 2657-2669.

Wood, J.E., Williams, D.B., Goldstein, J.I., 1984. Experimental and theoretical determination of kAFe factors for quantitative X-ray microanalysis in the analytical electron microscope. J. Microsc. 133, 255-274.

Ziebold, T.O., 1967. Precision and Sensitivity in Electron Micro-probe Analysis. Anal.Chem. 39, 858-861.

Zulliger, H.R., Aitken, D.W., 1970. Fano Factor Fact and Fallacy. IEEE Trans. Nucl. Sci. NS-17, 187.

A. Appendix

A.1 Abbreviations

ACF	absorption-correction factor
ADF	annular dark field
AFM	atomic force microscopy
AP	advanced polymer
BF	bright-field
CB	coherent bremsstrahlung
EBD	electron beam deposition
EDXS	energy-dispersive X-ray spectrometer/spectrometry
EELS	electron energy-loss spectrometry
EFTEM	energy filtered transmission electron microscopy
FEG	field-emission gun
FET	field-effect transistor
FIB	focused ion beam
FWHM	full width at half maximum
GIF	Gatan Imaging Filter
GIXD	grazing incidence X-ray diffraction
HAADF	high angle annular dark field
HR	high resolution
IBS	ion beam sputtering
ICC	incomplete charge collection
ISOTEC	Integrated Organic Sensor and Optoelectronic Technologies
MAC	mass attenuation coefficient
MCA	multichannel analyzer
MMF	minimum mass fraction
NIST	National Institute of Standards and Technology
OLED	organic light emitting device
OPD	organic photodiode
RMS	root mean square
SDD	silicon drift detector
SEM	scanning electron microscope
SI	spectrum image
Si(Li)	silicon crystal doped with lithium
SRM	standard reference material
STEM	scanning transmission electron microscopy
TEM	transmission electron microscopy
VTE	vacuum thermal evaporation
XRR	X-ray reflectivity
ZL	zero loss

A.2 ζ-factors

Table A.1: ζ-factors of K lines of the Si(Li) detector of Tecnai F20

Element	**Atomic number**	**Energy [keV]**	**ζ-factor [kg·electron/(m²·photon)]**
B	5	0.185	4210 ± 89
C	6	0.282	2014 ± 50
N	7	0.392	2691 ± 109
O	8	0.523	1820 ± 50
F	9	0.677	1791 ± 36
Ne	10	0.848	1444 ± 21
Na	11	1.041	1403 ± 17
Mg	12	1.254	1293 ± 15
Al	13	1.487	1320 ± 15
Si	14	1.740	1304 ± 15
P	15	2.013	1362 ± 15
S	16	2.307	1387 ± 15
Cl	17	2.622	1465 ± 16
Ar	18	2.957	1616 ± 17
K	19	3.313	1534 ± 16
Ca	20	3.691	1540 ± 16
Sc	21	4.090	1729 ± 18
Ti	22	4.510	1785 ± 19
V	23	4.951	1891 ± 20
Cr	24	5.414	1928 ± 21
Mn	25	5.898	2051 ± 22
Fe	26	6.403	2103 ± 22
Co	27	6.929	2260 ± 24
Ni	28	7.477	2301 ± 25
Cu	29	8.046	2556 ± 27
Zn	30	8.637	2721 ± 29
Ga	31	9.251	3010 ± 32
Ge	32	9.886	3273 ± 35
As	33	10.542	3568 ± 38
Se	34	11.221	3949 ± 42
Br	35	11.923	4196 ± 45
Kr	36	12.649	4623 ± 49
Rb	37	13.394	4972 ± 53
Sr	38	14.163	5328 ± 57
Y	39	14.956	5709 ± 61
Zr	40	15.777	6208 ± 66
Nb	41	16.618	6727 ± 72
Mo	42	17.482	7429 ± 79

Table A.2: ζ-factors of K lines of the Super-X detector of Titan[3]

Element	**Atomic number**	**Energy [keV]**	**ζ-factor [kg·electron/(m²·photon)]**
B	5	0.185	232 ± 3
C	6	0.282	163 ± 2
N	7	0.392	153 ± 2
O	8	0.523	144 ± 2
F	9	0.677	155 ± 2
Ne	10	0.848	143 ± 2
Na	11	1.041	150 ± 2
Mg	12	1.254	144 ± 2
Al	13	1.487	148 ± 2
Si	14	1.740	152 ± 2
P	15	2.013	160 ± 2
S	16	2.307	159 ± 2
Cl	17	2.622	170 ± 2
Ar	18	2.957	188 ± 2
K	19	3.313	179 ± 2
Ca	20	3.691	180 ± 2
Sc	21	4.090	202 ± 3
Ti	22	4.510	209 ± 3
V	23	4.951	221 ± 3
Cr	24	5.414	226 ± 3
Mn	25	5.898	240 ± 3
Fe	26	6.403	245 ± 3
Co	27	6.929	263 ± 3
Ni	28	7.477	267 ± 3
Cu	29	8.046	297 ± 4
Zn	30	8.637	316 ± 4
Ga	31	9.251	351 ± 4
Ge	32	9.886	386 ± 5
As	33	10.542	443 ± 6
Se	34	11.221	512 ± 6
Br	35	11.923	575 ± 7
Kr	36	12.649	679 ± 8
Rb	37	13.394	790 ± 10
Sr	38	14.163	924 ± 12
Y	39	14.956	1088 ± 14
Zr	40	15.777	1305 ± 16
Nb	41	16.618	1562 ± 19
Mo	42	17.482	1902 ± 24